

Copyright Warning & Restrictions

The copyright law of the United States (Title 17, United States Code) governs the making of photocopies or other reproductions of copyrighted material.

Under certain conditions specified in the law, libraries and archives are authorized to furnish a photocopy or other reproduction. One of these specified conditions is that the photocopy or reproduction is not to be “used for any purpose other than private study, scholarship, or research.” If a user makes a request for, or later uses, a photocopy or reproduction for purposes in excess of “fair use” that user may be liable for copyright infringement,

This institution reserves the right to refuse to accept a copying order if, in its judgment, fulfillment of the order would involve violation of copyright law.

Please Note: The author retains the copyright while the New Jersey Institute of Technology reserves the right to distribute this thesis or dissertation

Printing note: If you do not wish to print this page, then select “Pages from: first page # to: last page #” on the print dialog screen



The Van Houten library has removed some of the personal information and all signatures from the approval page and biographical sketches of theses and dissertations in order to protect the identity of NJIT graduates and faculty.

ABSTRACT

SIGNAL TRANSMISSION IN EPITHELIAL LAYERS

by
Filippo Posta

Cell signaling is at the basis of many biological processes such as development, tissue repair, and homeostasis. It can be carried out by different mechanisms. Here, we are focusing on ligand mediated cell-to-cell signaling in which a molecule (ligand) is free to move into the extra-cellular medium. On the cell layer surface, it can bind to its molecule-specific receptors located on the cell plasma membrane. This mechanism is the subject of many experimental and theoretical studies on many model biological systems, such as the follicular epithelium of the *Drosophila* egg, which motivates this work.

Here, we present a general mathematical model that incorporates the processes that characterize ligand mediated intercellular signaling in epithelial layers, and we study this model under various assumptions. This model is characterized by nonlinear reaction-diffusion type dynamics. The nonlinearities mainly arise at cell layer where feedbacks can be generated through e.g. ligand mediated ligand release. A direct consequence of this nonlinear behavior is a possibility of existence of multiple steady states and traveling wave solutions. In this thesis, we investigate these types of solutions numerically and analytically.

Looking for steady solutions of parabolic reaction-diffusion equations leads to nonlinear elliptic boundary-value problems. We take advantage of this property and develop an extension of the method of Optimal Grids for elliptic problems. We call this method Compensated Optimal Grids. We present its application and study its convergence properties. Ultimately, we show that this method can be spectrally accurate when applied to two dimensional problems, and fourth order accurate in the three dimensional case, despite the use of simple nearest-neighbor stencils.

We conclude our study by investigating signal transmission in the presence of bulk degradation. In particular, we study the multiplicity of steady states and construct traveling waves solutions for a mathematical model that accounts for degradation in the bulk, also obtaining biophysical conditions in which signal transmission is possible.

SIGNAL TRANSMISSION IN EPITHELIAL LAYERS

by
Filippo Posta

**A Dissertation
Submitted to the Faculty of
New Jersey Institute of Technology and
Rutgers, The State University of New Jersey – Newark
in Partial Fulfillment of the Requirements for the Degree of
Doctor of Philosophy in Mathematical Sciences**

**Department of Mathematical Sciences, NJIT
Department of Mathematics and Computer Science, Rutgers-Newark**

May 2008

Copyright © 2008 by Filippo Posta
ALL RIGHTS RESERVED

APPROVAL PAGE

SIGNAL TRANSMISSION IN EPITHELIAL LAYERS

Filippo Posta

~~Dr. Michael R. Booty~~
Dr. Cyril B. Muratov, Dissertation Advisor
Associate Professor of Mathematical Sciences, NJIT

04/22/08

Date

Dr. Michael R. Booty, Committee Member
Associate Professor of Mathematical Sciences, NJIT

04/22/08

Date

Dr. Lou Kondic, Committee Member
Associate Professor of Mathematical Sciences, NJIT

4/22/2008

Date

Dr. Victor V. Matveev, Committee Member
Assistant Professor of Mathematical Sciences, NJIT

4/22/08

Date

Dr. Stanislav Shvartsman, Committee Member
Associate Professor of Chemical Engineering and the Lewis Sigler Institute for
Integrative Genomics, Princeton

April 22, 2008

Date

BIOGRAPHICAL SKETCH

Author: Filippo Posta
Degree: Doctor of Philosophy
Date: May 2008

Undergraduate and Graduate Education:

- Doctor of Philosophy in Mathematical Sciences,
New Jersey Institute of Technology, Newark, NJ, 2008
- Master of Science in Computational Biology,
New Jersey Institute of Technology, Newark, NJ, 2002
- Bachelor of Science in Mathematics and Computer Science,
Universita' degli Studi di Siena, Siena, Italy, 2000

Major: Mathematical Sciences

Awards:

- *College of Science and Liberal Arts Outstanding Graduate Student*,
New Jersey Institute of Technology, Newark, NJ, 2008
- *Teaching Excellence Award as TA*,
New Jersey Institute of Technology, Newark, NJ, 2006

Presentations and Publications:

- F. Posta, S. Y. Shvartsman, and C. B. Muratov, "Compensated optimal grids for elliptic boundary value problems", *Journal of Computational Physics*, Submitted for review 2008.
- F. Posta, C. B. Muratov, and S. Y. Shvartsman, "Autocrine signal transmission in the presence of volume degradation", *Biophysical Journal*, In preparation 2008
- F. Posta, "Signal Transmission in Epithelial Layers", *Frontiers in Applied and Computational Mathematics*, Poster presentation, May, 2007

*to my beloved mamma and babbo,
"grazie della vita che mi avete regalato"*

ACKNOWLEDGMENT

At last I am here, writing the final chapter of my life as a graduate student. I can only start by thanking my parents. Although my family has been living in Tuscany for generations, I always feel as though they are standing here beside me with love and support.

I would not be here, writing this thesis, if two people at NJIT did not go out of their way to help me in my graduate studies. My advisor, Dr. Cyril Muratov, has been unbelievably patient with me while I was struggling to manage my research and teaching responsibilities. He has always pointed me toward the right direction, providing clarity, encouragement, and a sense of professionalism.

In addition, Dr. Lou Kondic, a committee-member, has been a great source of support. Without him, I would have never been able to pass the qualifying exams. He has been a wonderful teacher and mentor.

I would also like to thank the other members of my committee: Dr. Michael Booty, who gives the best notes among NJIT Professors, and whom I enjoyed working with while organizing various student activities. Dr. Victor Matveev, who not only is the best runner among the NJIT faculty, but has also been consistently generous in answering my questions. Last, but definitely not least, Dr. Stanislav Shvartsman. His work has been fundamental in stimulating my passion for Developmental Biology. In addition, his class in pattern formation at Princeton University has been one of the highlights of my academic career.

When I look back at the time spent at NJIT, there are many people that I will always remember: faculty members, administrators, my students, and even the staff at the cafeteria. I cannot name them all, otherwise my “Acknowledgment” section would be longer than the thesis itself - much to the dismay of Dr. Kane. My graduate school experience has also enabled me to form lasting friendships. Specifically, Hakan,

Nebo, Tsezar and Yuri: we have been through a lot together, and I am sure that good things are ahead. I look forward to continuing our friendship for the rest of our lives.

When I have discussed writing this thesis, and have complained about the time and effort it has required, I have often heard the comment: Relax, nobody is going to read it anyway. Despite these sentiments, I know of one person that would beg to differ: LovaLova and Emily.

LovaLova: you have been a great source of fun and support. All of those fantastic times we have spent driving around the U.S.A. have re-charged both my energy and spirit.

Emily: thanks for all your love, support and English expertise. I will do the same for you while you work on your own doctorate dissertation, as a good husband should!

TABLE OF CONTENTS

Chapter	Page
1 INTRODUCTION.....	1
2 MODELING SIGNAL TRANSMISSION IN EPITHELIAL LAYERS.....	9
2.1 Modeling Issues.....	10
2.2 General Model for Signal Transmission in Epithelial Layers	11
2.3 Model Simplification and Analysis	19
2.4 Traveling Wave Solution	24
2.5 A Numerical Study	30
3 COMPENSATED OPTIMA GRIDS	34
3.1 Optimal Grids	35
3.1.1 N operator for the Laplace equation in half-space [50]	36
3.1.2 Connection between N and the numerical solution of elliptic problems ..	37
3.1.3 Convergence of optimal grids	40
3.1.4 Optimal geometric grids	41
3.2 Compensation	41
3.3 Convergence of Compensated Optimal Grids	46
3.3.1 Comparison with Zolotarev and optimal grids	46
3.3.2 An exactly solvable nonlinear problem	50
3.3.3 Extension to three dimensional problems	54
3.3.4 Compensation on hexagonal grids	55
3.3.5 Compensation on anisotropy-adjusted square grids	60
3.4 Application to Cell Signaling	64

TABLE OF CONTENTS
(Continued)

3.5 Some Theoretical Considerations	68
4 AUTOCRINE SIGNAL TRANSMISSION IN THE PRESENCE OF VOLUME DEGRADATION	70
4.1 Mathematical Model with Degradation	70
4.2 Comparison with the Thin-Gap Limit	72
4.3 Steady State Multiplicity	75
4.4 Stationary Fronts	80
4.5 Traveling Waves	85
4.6 Exact Traveling Wave Solutions	91
5 CONCLUSIONS AND FUTURE RESEARCH	95
APPENDIX STABILITY OF TIME DEPENDENT PROBLEMS	100
REFERENCES	103

LIST OF TABLES

Table		Page
2.1	List of the symbols and their description in equations (2.4)-(2.8).	16
2.2	Typical value of the parameters of the EGFR system for the Drosophila oocyte [61, 74].	20
3.1	The optimal grid steps corresponding to (3.30).	46

LIST OF FIGURES

Figure	Page
2.1 (a) Schematic of the signal transmission framework. (b) Ligand-receptor dynamics at cell surface level.	12
2.2 Behavior of the Hill function for fixed $a = 1/2$. Notice how as n increases toward infinity, the Hill function approaches the Heaviside function centered at a (thick black line).	24
2.3 Graphs of the velocity of the traveling front solutions as a function of a for small values of τ . Notice the convergence of v toward its asymptotic limit at $\tau = 0$ (red line).	26
2.4 Graphs of the velocity of the traveling front solutions as function of a for large values of τ . Notice the asymptotic behavior of v as $\tau \rightarrow \infty$ (red line).	29
2.5 Behavior of numerical solutions of (2.17) at different times. These plots are obtained using the FTCS finite difference scheme described by (2.33) with no flux boundary conditions, initial conditions $s(x, 0) = \theta(x - 3)$, $p(x, 0) = 0$, and parameters $a = 0.3$, $\tau = 3$, $n = 20$, $\Delta x = 0.5$, and $\Delta t = 0.04$	31
2.6 Numerical results for the qualitative behavior of the position of the traveling front for both s (blue line) and p (red line), for the same parameters of the simulation in figure (2.5). The slope of the blue line is 0.1797 and the one for the red line is 0.1799. They both agree up to three significant digits to the velocity obtained through (2.22) in the case of the Heaviside nonlinearity, which is 0.179276.	32
3.1 Relative Error in approximating $R(\lambda)$ with different methods.	41
3.2 Relative error in approximating $F_c(\lambda)$ in Eq. (3.27).	45
3.3 Comparison of the performance of different optimal grids for solving the boundary-value problem (3.31) with m fixed. In both (a) and (b), the relative error of the solution is shown for all admissible values of q ; $n = 8$ in (a), while $n = 14$ in (b). In all cases $m = 1000$	48
3.4 Convergence study for the solution of (3.31) with $q = 4$. Results for the compensated grids with $n = 10$ and $n = 14$, as well as geometric and Zolotarev grids with $n = 14$ are shown.	50
3.5 (a) The form of the solutions of (3.35) for several values of α . (b) Results of the convergence studies of the numerical solution using a compensated grid with $n = 14$ obtained in Sec. 3.2.	52

LIST OF FIGURES
(Continued)

Figure	Page
3.6	Convergence study for the solution of (3.43) with results for the compensated grids with $n = 14$ for various combinations of \mathbf{q} , together with the results for an optimal geometric grid of size $n = 14$ (continuous black line). 56
3.7	(a) The discretization of the rectangular domain using a hexagonal grid. (b) The 9-point anisotropy-adjusted stencil for Δ_{\perp} on a square grid. In (a), the solid circles show the discretization nodes, while the empty circles correspond to the ghost nodes of the reflecting boundary. Similarly, solid lines in (a) show the connections between the discretization nodes, while dashed lines show the connections to the ghost nodes. In (b), the fractions give, apart from the factor of h_{\perp}^{-2} , the weights of different nodes in the stencil. 57
3.8	The L^{∞} norm of the relative error of the numerical solution of (3.43) and (3.44) obtained, using hexagonal grids in the xy -plane and compensated optimal grids with $n = 8$ in (a) and $n = 14$ in (b) (see text for complete details). In (b), the straight line indicates the $O(\mathbf{q} ^4)$ dependence. . . . 60
3.9	The L^{∞} norm of the relative error of the numerical solution of (3.43) and (3.44) obtained, using anisotropy-adjusted square grids in the xy -plane and compensated optimal grids with $n = 8$ in (a) and $n = 14$ in (b) (see text for complete details). In (b), the straight line indicates the $O(\mathbf{q} ^4)$ dependence. 63
3.10	(a) The profile of the solution of (3.71) obtained using the $n = 14$ compensated optimal grid of Sec. 3.3.3 on a hexagonal lattice with $h_{\perp} = 0.25$, $L_x = 60h_{\perp}$, $L_y = 68h_{\perp}\sqrt{3}/2$. (b) The relative error of $\bar{u}(0,0)$ obtained using the $n = 14$ compensated optimal grids of Sec. 3.3.3 for hexagonal and anisotropy-adjusted square lattices. In (b), the straight line indicates the $O(h_{\perp}^4)$ dependence. 68
4.1	Ligand-mediated signal transmission. (A) The geometry of the system modeled by Eq. (4.1). (B) Illustration of elementary processes. 71
4.2	Graphical representation of a bi-stability scenario for Eq. (4.11) 74
4.3	Multiplicity of the steady states for Hill nonlinearity with $n = 2$. (A) Three possible scenarios for the solution of Eq. (4.18). (B) The behavior of the two nontrivial solutions s_2 (unstable) and s_3 (stable) as γ increases. In both plots $c_0 = 0.2$ 77
4.4	Dependence of λ upon q for the steady states s_2 (subplot A) and s_3 (subplot B). For this study we used $\gamma = 0.3$ and $c_0 = 0.1$ 79

LIST OF FIGURES
(Continued)

Figure	Page
4.5	Steady state bifurcation diagram superimposed on the plot of the autocrine loop activation threshold curve for Hill nonlinearity with $n = 2$ 83
4.6	Autocrine loop activation threshold in the case of the Heaviside nonlinearity. 84
4.7	Autocrine loop activation threshold: comparison between the Hill and the Heaviside nonlinearities. 84
4.8	The profiles of a traveling wave solution at $\alpha = 0.2$, $\gamma = 0.1$, $c_0 = 0.188$. In (A) and (B), the distributions of $s(x, 0)$ and $p(x)$ are shown, in (C) a contour plot of $s(x, z)$ is shown. 87
4.9	Relation between the traveling wave velocity v and the activation threshold c_0 for different values of α at $\gamma = 0.1$, obtained from Eq. (4.43). 88
4.10	Dependence of the propagation velocity v on γ for different values of c_0 (A) and α (B), obtained from Eq. (4.43). In A, $\alpha = 0.1$, in B, $c_0 = 0.15$. 89
4.11	Dependence of the propagation velocity on the Hill coefficient at $\gamma = 0.25$, $\alpha = 0.1$, $c_0 = 0.1594756$, obtained from the numerical solution of Eqs. (4.5) – (4.7). 90
4.12	Contour for the integral of Eq.(4.56). 92
5.1	The user input a number of nodes is randomly placed on a prescribed geometrical shape. 96
5.2	A simulated annealing algorithm rearranges the nodes to minimize a given penalty function that is selected with the goal of achieving a regular configuration of nodes. 97
5.3	Voronoi partitioning of the given domain. 98

CHAPTER 1

INTRODUCTION

Advances in the technologies that are used to investigate the physical world are constantly reshaping the modus operandi of scientists. As a result, the classical fields of science do not exist as semi-isolated compartments, and “interdisciplinary” is the rule rather than the exception of most research projects. Biological and Medical studies provide the most obvious example of this change of times. In these fields, there is a necessity of Mathematicians, Physicists and Statisticians to model and interpret the data that new technologies are able to produce. Nowadays, it is not uncommon for outstanding scientists (e.g. the mathematician J.D. Murray) to not only provide a mathematical description of a certain medical condition (e.g. tumor growth), but also to suggest the best way to treat it [55, 76, 77]. In [77], the authors constructed a mathematical model to study the dynamics of serum prostate-specific antigen (PSA), a marker for prostate cancer. The value of PSA is usually used to screen patients for prostate cancer, it is a very common yet painful procedure. And it has been proved clinically (see references in [77]) that from the level of detected PSA it is possible to see if prostate cancer is forming or if the patient could have prostate cancer in the future. There is an anomaly, however; some patients could have low level of PSA and still develop prostate cancer. Through the analysis of their mathematical model, the authors were able to give an explanation of this anomaly. They showed that the patients that develop prostate cancer after showing low level of PSA have fast changing PSA levels, and therefore they need to have their levels checked more often to establish this trend and catch the tumor in time.

This Ph.D. thesis too is the product of an interdisciplinary collaboration in which we investigate (through the analysis of problem-specific mathematical models)

some of the genetic and biochemical events that can lead to spatial patterning in a certain biological model (e.g. epithelial layers of drosophila).

Spatial patterning is a central problem in the field of developmental biology [55], and also applies to many other physiological contexts [28]. Developmental biology is the branch of biology that focuses on the evolution of an organism from its early embryonic stages to its adult form. Researchers in the field are investigating such problems as dynamics of cell growth, cell differentiation, and morphogenesis. Understanding these mechanisms will shed light on many open-ended questions, some of which, we might have asked ourselves, such as what determines the spots on a leopard, or the stripes on a zebra, or the proportions of a human body.

The human body, or any other mammal, develops from one single cell, the zygote. This cell begins its development by dividing itself, creating an agglomerate of cells (all of the same type) that constitute the early embryo. This early embryo will ultimately evolve into an adult, consisting of 100 trillion cells of different types [45]. Biologists have been able to determine when cell differentiation and patterning takes place, and also where the instructions for it are contained (the genome). However, the mechanisms that govern these processes have yet to be explained in details.

Studies to understand developmental processes spiked in the late 1960s and early 1970s. The work of many developmental biologists highlighted the importance of positional information in development, introducing the notion of pattern formation as spatial organization of cell differentiation [89]. A well documented *in vivo* model of patterning arising from positional information was given by hydra experiments [91, 87]. These studies showed that when the head of a hydra is cut off, and the parts below the severed head are grafted to the body, depending on the position of the newly grafted material, the hydra was able to regenerate either one or two heads [71].

Around the same period of time, theoretical work on pattern formation sprouted from the last paper by Alan Turing [83]. His work showed how differences in the diffusion constants of interacting chemicals could lead to pattern generating instabilities. While most of the early contribution to this theory came from the work of Gierer and Meinhardt [30] (who are still working on the subject [31]), the subject has generated a huge amount of research and not only in Biology, but in related fields (see, e.g. [49, 46, 56]).

From the diffusion-driven instabilities of the Turing theory, many other mathematical models (mainly borrowed from chemistry) had been proven to have the capability to generate complex patterns from simple settings [53, 84, 93]. However, none of these models had been able to capture the dynamics of a developing embryo in such a comprehensive way as the Hodgkin-Huxley model did for the electrical activity in physiology (to cite probably the most important model in physiological literature [41]). The reasons for the (relative) shortcomings of these models is directly correlated with the many unanswered questions that experimentalists are still trying to address, such as the identification of key molecules, genes, etc.

Development is a highly complex process that involves many structurally diverse elements which operate on totally different time and length scales. For instance, the instructions for cell development are contained in the genetic code of the cell itself, and the result of these instructions will correspond to an adult, fully functional organism [90]. It is not an easy task to determine the genetic network that determines the foundation of a certain developmental mechanism or to closely monitor molecular interactions that activate certain genetic patterns.

Continuing technological and methodological advances are allowing scientists to improve the identification and monitoring of developmental processes at genetic and molecular levels. The observations obtained from these studies have led to many important discoveries, such as the confirmation of the existence of morphogen gradi-

ents, and have changed the way developmental processes are modeled. In fact, this better (albeit not yet complete) picture of the players and processes that compose the dynamic of embryonic development in many model organisms (e.g. *Drosophila*, *Xenopus*), has led to mathematical representations of this dynamic through mechanistic models that can emulate each process more effectively [64, 55]. At the same time, comprehensive developmental pattern formation models are characterized by many different variables and parameters that characterize each process they represent.

Moreover, different processes have different time scales, length scales, and governing dynamics (e.g. activation of a genetic pathway, as opposed to the diffusion of a ligand in the extracellular medium). When this intrinsic complexity of developmental models is coupled with the lack of experimental measurements of parameters, or the uncertainty with the precise determination of the players involved in a specific framework, we might ask ourselves if these models are realistic at all.

The truth is that while we are still far away from being able to construct comprehensive mathematical models of basic developmental processes, we can successfully synthesize the available experimental results into “working” mathematical models, and then analyze these models to obtain a better understanding of the underlying biological mechanisms they try to represent [64]¹.

The most successful modeling results have been obtained for *Drosophila*. This is due to the fact that its genome has been completely mapped [1], and many of the developmental processes of its embryonic stages have been characterized both *in vivo*, and *in vitro* [28, 90].

In [32], the authors used dimensional analysis to identify the key parameters that determine the shape of the gradient of Gurken, a morphogen acting in the development of *Drosophila* egg. In particular, the authors found that to quantify the shape of the morphogen gradient, there was no need to evaluate every single parameter in

¹We strongly recommend this article for a more complete review of the current status of quantitative modeling in development

the model, but just the ratio between the ability of Gurken to diffuse and the spatial decay of the same morphogen. This parameter is known in the engineering literature as the Thiele modulus [86]. Essentially, it represents the ratio between the size of a system and the spatial decay of a signal diffusing through it. Furthermore, to have an efficient patterning this parameter should be of order one [64]. This dimensional analysis inspired the authors of [32] to formulate a method to estimate the parameter, obtaining a value of approximately 3, from the experiments.

We should also note that while the Thiele modulus can be directly correlated with the shape of the gradient of Gurken, there are other morphogenic scenarios where other dimensionless parameters seem to be more relevant. For instance, in the case of bicoid (the first morphogen gradient to be observed experimentally) it was assumed that the shape of the morphogen's gradient is determined (similarly to Gurken) by the competition between the diffusivity and the degradation of the signal, thus leading to Thiele modulus dependence [36, 34]. However, in a recent paper [14], the authors showed that it was the competition between diffusion and nuclear trapping that may be responsible for the shape of the bicoid gradient. This is quite a common occurrence in a field such as rapidly evolving as Developmental biology, hence mathematical models can change quickly as well.

Dimensional analysis, together with other common mathematical model techniques, such as asymptotical studies [52] can be important tools for model analysis and model simplification. However, the most direct method in our hands is computational analysis.

The computational studies of mathematical models are of great impact and of great necessity, since the more complex the model, the less likely we will be able to obtain quantitative analytical results from it. There are plenty of successful applications of numerical studies in the field of developmental biology. Some of the most recent ones are presented in [93, 20, 63, 62]. In general, the computational analysis of

a mathematical model is very effective in determining the feasibility and sufficiency of patterning mechanisms, such as in [62] where it is shown that a positive feedback loop is sufficient to generate long-range signal transmission in an idealized epithelium.

The above paragraphs represent only a brief overview of some of the general concepts concerning modeling in developmental biology. As we proceed with the description of the work we have done, we will also give more details about why certain mathematical and numerical techniques are used over others. In addition, we will discuss what we want to accomplish with every specific analysis. Before, we do that, we want to briefly describe our approach within the aforementioned developmental framework.

As the title suggests, this thesis aims to model intercellular signaling, since signaling processes are of fundamental importance in development. Our work is motivated by the ligand mediated signaling mechanisms that take place in the development of *Drosophila*.

We will use the general mechanistic model presented in [62, 53], and elaborate upon it with the aim of analyzing certain regimes and processes related to ligand mediated cell communication. In particular, we are interested in the existence and properties of traveling front of cell signaling. In fact, from some experiments we infer that diffusion alone of cell signaling is not sufficient to explain the observed gradients. Furthermore, the nonlinear coupling between diffusing ligand molecules and intracellular chemicals can lead to the existence of multiple steady states in the mathematical model. A known feature of bistable reaction diffusion equations is to have traveling front solutions connecting different steady states [41, 55]. We will use some mathematical and computational techniques to carry out these studies. Numerical analysis is a centerpiece of this work. We will use it to validate our analytical results, as well as to compare our findings with the ones in the relevant literature.

One of our main results is the development of a numerical method tailored to simulate our model. We called this method Compensated Optimal Grids (COG), since it is an extension of the optimal grids method presented in [38].

There are plenty of numerical methods that can be used to solve simple problems involving partial differential equations. However, for more complicated settings such as systems of nonlinear partial differential equations in three dimensions, these methods either fail to work or are too computationally expensive. For instance, finite differences methods on a uniform grids represent a very straightforward and efficient way to discretize a partial differential equation in one dimension. However, for higher dimensions, these methods become very computationally expensive and other methods are chosen instead. In our case, the implementation of COG allowed us to obtain accurate solutions while minimizing the computational power needed to carry the simulations. This is a very important aspect of modeling. Often we begin working on a very simplified model (e.g. a one dimensional reduction of a three dimensional system), and use standard numerical techniques such as finite differences because they are easy and fast to implement. However, when we want to extend the model to a more complex setup, the computational costs drastically increase, and these standard techniques are unable to produce results in an acceptable amount of time, hence the necessity of implementing numerical techniques that are adequate for our task.

We will use these numerical techniques together with analytical ones, to study cell signaling in a model epithelium in presence of degradation in the bulk. In particular, we will study the multiplicity of steady states for this model and the traveling front solutions that are expected in case of the bi-stability.

The thesis is organized as follows:

Chapter 2 We present the biological and modeling concepts regarding ligand mediated signal transmission. We describe the fully dimensional model that is the starting point of our studies, and we study it under a certain set of as-

sumptions. This first analysis is used to present some of the questions that researchers are trying to answer using mathematical models of biological phenomena.

Chapter 3 We introduce a computational approach to solve elliptic boundary value problems in unbounded domains, and explain how this method can be effective to simulate our model. The method that we called Compensated Optimal Grids is an extension of the Optimal Grids method that was introduced by Druskin et al. [38]. We describe the application of the method for Elliptic p.d.e.'s, discuss its convergence, and present its application to a model cell signaling problem.

Chapter 4 We analyze a cell signaling framework in which one degradation in the bulk term is added to the basic events that characterize our model from Chapter 2. In addition, we study the existence and properties of propagating fronts under this regime. We also describe the effect of using the Heaviside function as an approximation of the Hill function that is usually used to lump certain intracellular processes that characterize ligand activation [23].

Chapter 5 We discuss our findings in a developmental context, and present potential future extensions of our work.

Appendix We derive the stability properties of the compensated optimal grid method for the solution of parabolic problems.

CHAPTER 2

MODELING CELL SIGNALING IN EPITHELIAL LAYERS

Intercellular communication is fundamental for every organism to be able to carry out those biological processes that constitute the organism's life-cycle. Every step is started, regulated, and ended through precise mechanisms that involve the interaction of cells among themselves and their environment. Intercellular communication is characterized by different types of signals which can be extremely different in nature, such as electric signals (caused by the movement of ions), direct cell-to-cell communication of adjacent cells (through gap junctions on the neighboring cell's membranes), and extracellular signaling molecules [45]. The latter is the form of cell-to-cell communication we are interested in.

In this communication process, extracellular signaling molecules are synthesized and released by signaling cells. The signal diffuses within the extracellular space so that it can reach target cells, e.g. cells that have the ability to capture the signal itself. This ability consists of the presence of specific molecules called receptors (see Fig. 2.1 part b).

There is a huge variety (both in size and nature) among signaling molecules. Some of the signals (like steroids) are so small that they can diffuse through the plasma membrane and bind to the intracellular receptors, others are too big to pass through the membrane and therefore they bind to receptors which are located on the membrane's surface. The binding leads to changes in the cytosol through the activation/deactivation of signaling pathways that can generate extreme changes in the cell state [45].

The mechanism of cell communication in which an extracellular molecule (ligand) acts as a signal and binds to a receptor located on the membrane of a cell to

generate a cell response is of primary importance in development [29], tumor growth [2], and wound healing [57].

Studies in developmental biology have shown how genetic patterns generated by the distribution of the ligands among different cells lead to specific fates of the affected cells. For example, the distribution of ligands in epithelial layer of the egg of the fruit fly determines the axial orientation of the embryo [11, 65].

Pattern formation in development due to secreted ligands is common in epithelial layers [35] making them a more general target for our study. In this context, the cells in the layer secrete ligands in the extracellular space, the free extracellular ligands can then bind to the receptors that are present on the surfaces of the cells thus creating ligand-receptor complexes. The concentration of these complexes within a single cell induces a response by the cell itself. This response can be both of activation or inhibition of secretion of the ligand itself, thus creating positive and negative feedback loops [28].

2.1 Modeling Issues

After this crude introduction to signal transmission in epithelial layers, it is important to stress some of the features that are of special interest when trying to build a mathematical model of the system:

Spatial Scales : an epithelium is characterized by three extremely different spatial domains, the extracellular space (three dimensional) where the ligands diffuse, the cell surface layer (two dimensional) where the forward and backward binding occur, and the intracellular space that interprets the signal and reacts accordingly.

Time Scales : each spatial step described above is characterized by one or more time scales. As an example, let us consider the cell layer where we can identify three different timescales: for forward binding, backward binding and internalization

of a complex. This issue becomes even more complicated if we consider the intracellular mechanisms that lead to ligand release by the cell [28].

Nonlinearities : nonlinear behavior is common among the elements of the system.

For example, different ligands can bind to the same receptor, or two ligands can bind among themselves and by binding among themselves they can inhibit receptor binding [88]. Another example of nonlinear behavior is given by the sensitivity of the intracellular species that determines the set of reactions that lead to ligand release [37]. It is quite problematic to exactly model these behaviors or even to choose which one of these behaviors has to be modeled or can be neglected.

As a result, there are a lot of open questions about signal transmission in epithelial layers, such as the determination of the rate-limiting steps, the range of the signal or its duration. The goal of a mathematical model of the system is to furnish further insights to these questions. For example, by confirming some experimentally observed behaviors or by leading to a better experiment design.

2.2 General Model for Signal Transmission in Epithelial Layers

The general modeling framework of our analysis is depicted in Fig. 2.1. In it, we can identify (from bottom to top) three compartments, the layer of epithelial cells where the signal is processed, the cell surface layer, where the signals are captured by the receptors and transduced inside the cells, and the extracellular compartment where the signal diffuses. This division into three main parts is of main importance, and therefore we are going to describe in more details the processes that take place in each compartment, together with their representation [53].

Extracellular Medium Cells secrete ligands into the extracellular medium. While in the medium, the ligand molecules diffuse and interact among each other and the

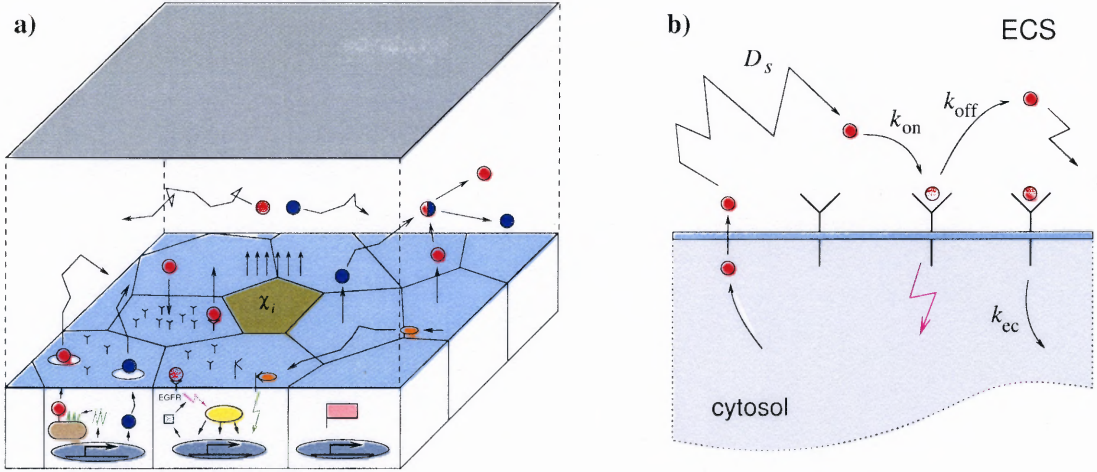
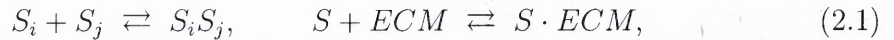


Figure 2.1 (a) Schematic of the signal transmission framework. (b) Ligand-receptor dynamics at cell surface level.

medium itself. The extracellular space is considered unbounded in the x and y directions, while in the vertical direction there are two precise boundaries, the cell layer on the bottom and an "impermeable wall" on top that is characterized by the fact that ligands cannot move through it. While diffusing, ligands can reversibly bind to each other or with the medium itself (ligands are represented by the green and blue dots and the orange ovals in Fig. 2.1) a. These interactions can have an essential impact on the signal. For example, association with extracellular material can regulate the range of the signal or even inhibit the signal itself [28, 44].

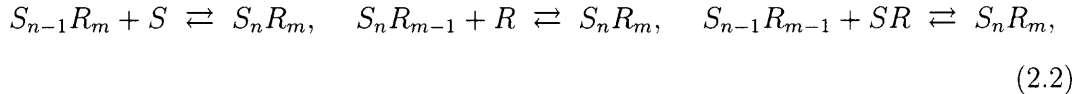
We can model these interactions using the law of mass action [41]:



where S_i and S_j are two ligand molecules and ECM indicates the extracellular medium. These reactions are characterized by certain rates which are determined experimentally (when possible). When reaction coefficients cannot be obtained experimentally, a mathematical/computational analysis of the model is essential to obtain qualitative information about the rates that lead (or not) to the observed evolution

of the system. For instance, in Chapter 4, where we look at the model in presence of degradation in the bulk, we determine the relative rates of ligand activation and ligand degradation so that traveling wave solutions for the system are possible.

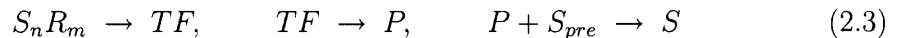
Cell Surface The cell surface layer is the centerpiece of the whole communication process. We consider a flat layer (Fig. 2.1 a) so that the geometry of the compartment is two-dimensional, and we make no assumptions on the shape of the cells. Two actions characterize this compartment (Fig. 2.1 b). The main one is the ligand-receptor complex formation/dissociation, in which ligands reversibly bind to cell surface receptors, thus transmitting the signal to the inside of the cell. The receptor is the physical link between the cytosol and the extracellular space, and when a ligand binds to it, the cell is able to sense this through the phosphorylation of the intracellular domain of the receptor [45]. Also, the complexes are not always constituted by one ligand and one receptor; actually it is quite the opposite, to have signal transmission more than one ligand and receptor need to be part of the complex. These mechanisms are represented through the following reactions schemes:



where S_nR_m represents a complex consisting of n ligand molecules together with m receptor molecules. In general $n \leq m$ and the configuration $n = 0$ and $m = 1$ represents an unoccupied receptor molecule. Although we are not going to explore this property in this thesis, we should stress the fact that there are many different configurations of ligand-receptor complexes. In particular there is signal activation only under specific ligand-receptor configurations such as the dimer (a complex formed by two ligand and two receptor molecules (S_2R_2)) that can be observed in EGFR systems [85]. For more general systems we know that m and n are small [28]. The other process that characterizes this subsystem is endocytosis of complexes, in which

ligand-receptor complexes are internalized at some prescribed rate. Endocytosis and binding are not the only interactions occurring at surface level. In fact, receptors are also able to move within the cell surface, and there is also the question of replacing internalized receptors. We will use biologically based assumptions to deal with these “minor” processes, and we will only concentrate on binding and endocytosis.

Intracellular Space Inside the cell the signal is interpreted, and a series of intracellular reactions leads to a determined physiological response by the signaled cell. The signal’s transduction cascades are started inside the cell when phosphorylation of the receptor tail occurs. These cascades lead to the activation of different targets. Among them, there are transcription factors (TF in the equations below) which determine the transcription and translation of proteins that can activate the production of ligand precursors. A precursor’s activation will lead to the secretion of ligand molecules in the extracellular space that can generate both positive and negative feedback loops [62, 53, 45, 37]. These processes can be represented through a series of irreversible enzymatic reactions:



The above discussion is extremely abstract, since for the purpose of this work we are not interested in a specific analysis of each reaction that takes place internally, but rather we are interested in qualitative responses such as the timescale of intracellular ligand production once the signal is sensed.

Now that we have a broad idea about the mechanisms that govern the system, we can present a mathematical model that describes the evolution of these same

processes¹[53]:

$$\frac{\partial S}{\partial T} = D_S \nabla^2 S + f(S) \text{ in } \Omega \times (0, H), \quad \frac{\partial S}{\partial Z} \Big|_{Z=H} = 0, \quad (2.4)$$

$$\frac{\partial C}{\partial T} = D_C \nabla_{\perp}^2 C + k_{on} R \bar{S} - (k_{off} + k_{ec}) C + \gamma(C, P) \text{ in } \Omega, \quad \frac{\partial C}{\partial n} \Big|_{\partial \Omega_i} = 0, \quad (2.5)$$

$$\frac{dP_i}{dT} = -k_P P_i + \sigma(C_i, P_i), \quad C_i = \int_{\Omega_i} C dx dy, \quad (2.6)$$

$$\bar{S} = S \Big|_{Z=0}, \quad R = R(C), \quad P = \sum_i P_i \chi_i, \quad (2.7)$$

$$\left(D_S \frac{\partial S}{\partial Z} - k_{on} R S \right) \Big|_{Z=0} = -k_{off} C - \sum_i g_i(C_i, P_i) \chi_i. \quad (2.8)$$

This is a full dimensional model in time and space. The surface of the cell layer is represented by the two dimensional domain $\Omega \subseteq \mathbb{R}^2$ and the surface of the i -th cell is indicated by Ω_i , where $\Omega_i \subset \Omega$ and $\Omega_i \cap \Omega_j = \emptyset$ for $i \neq j$. $\chi_i(X, Y) = 1$ if $(X, Y) \in \Omega_i$ and zero otherwise is the characteristic function of the i -th cell. The extracellular medium is represented by the three dimensional domain $\Omega \times (0, H)$, where H is the height of the medium (which we assume constant).

The main quantities of the model are the vectors S, C , and P that denote the concentrations of the ligands, ligand-receptor complexes, and intracellular species respectively. Their dynamics is described by equations (2.4), (2.5), and (2.6). The first equation, the one for the evolution of ligand concentrations, is a typical reaction-diffusion partial differential equation with a forcing term f and diffusion matrix D_S , it describes the mechanisms of (2.1) and is characterized by no-flux boundary conditions at the top and the sides of the extracellular medium. In Chapter 4 we will use a particular expression of f to represent degradation in the bulk.

¹A summary of the meaning and the description of the various symbols in the above equations is given in Table 2.1.

Equation (2.5) describes the diffusion of the ligand-receptor complexes at cell surface level ($Z = 0$) in connection with the various processes that characterize the cell surface layer of the system. In particular, the second and third term of the right-hand side of the partial differential equation describe the dynamics shown in part b of Fig. (2.1), where $k_{on}R\bar{S}$ and $k_{off}C$ represent the process of association and dissociation of complexes as represented by reactions in (2.2), and $k_{ec}C$ is the term associated with the receptor-mediated endocytosis in which a complex is internalized. The meaning of the γ term is to be related to the local behavior of the complexes and the intracellular species, in this work we assume it to be negligible.

Table 2.1 List of the symbols and their description in equations (2.4)-(2.8).

Symbol	Description
T	time variable
$\Omega \subseteq \mathbb{R}^2$	Two dimensional domain of the epithelium
Ω_i	Domain of the i-th cell
$(X, Y) \in \Omega$	Surface variables
$Z \in (0, H)$	Medium's height variable
$S(X, Y, Z, T)$	Concentration vector of different species of ligands
D_S	Ligand diffusion matrix
∇	Three dimensional gradient
∇_{\perp}	Two dimensional gradient in the plane of the epithelium
$C(X, Y, T)$	Concentration vector of ligand-receptor complexes
D_C	Matrix of ligand-receptor complexes diffusion coefficients
k_{on}	Rate constant of ligand receptor association
k_{off}	Rate constant of ligand receptor dissociation
k_{ec}	Rate constant of endocytosis

$R(X, Y, T)$	Concentration vector of ligand-receptor complex precursors
χ_i	Characteristic function of the i -th cell
$P_i(T)$	Vector of concentrations of the different intracellular species
k_P	Rate constants of degradation of P
g_i	Production rates of P for the i -th cell

The last element that needs to be described in the reaction diffusion equation (2.5) is $R(C)$. This vector represents the concentration of the ligand-receptor complex precursors, e.g., the concentration of those ligand-receptor complexes that need the addition of another molecule to form a certain complex. For example R_2S and RS are precursors of the dimer R_2S_2 .

The equation for the local dynamics of the intracellular species P due to receptor signaling is given by (2.6). This is a first order nonlinear ordinary differential equation in time characterized by two terms, the first one $k_P P_i$ describes the process of degradation of the intracellular material, and the second is a nonlinear term which represents the processes of (2.3). In particular σ is a sigmoidal function whose argument is the total amount of ligand-receptor complexes on the cell surface and the concentration of intracellular materials that are directly related to the ligands or receptors (e.g. ligand-processing protease). This type of function has been observed to effectively model the cascade that starts with the activation of a pathway and ends with the release of the final product. In particular, and we will discuss it in more detail later, this sigmoidal function can be represented by a Hill function with some pre-determined coefficient [37, 23].

Equation (2.8) describes the boundary condition at cell surface level. The left-hand side represents the diffusion and binding of ligands, while the right-hand side is composed of two terms, one describes the dissociation of complexes and is the same as the analogous term in (2.5), and the other models new ligands that are released in the extracellular medium due to intracellular processes.

This is an extremely general model that captures the essential features of the dynamics of ligand/receptor mediated signal transmission. It is flexible enough to be adapted to more specific systems and studies, and it has been the foundation of various works [62, 61, 53] in which this general model was reduced to model a special biological system under various assumptions. For instance, all three of these works are based on frameworks consisting of one ligand, one receptor, and one ligand-processing protease. Also, these nonlinearities f , and γ , and the diffusion of C are absent.

In [62], the authors consider a model whose limiting step is the amount of available ligand (in other words, there is never a shortage of free receptors), it has fast binding (the number of complexes is considered to instantaneously adjust to ligand binding and complex internalization), the variables in the system are independent of Y , and σ is characterized by a sharp threshold. The reduced model they obtain is characterized by two steady states, one with no signal transmission and one in which there is production of intracellular protease. They found (numerically and analytically) traveling wave solutions with constant speed for the model and studied the ability of these solutions to propagate through heterogeneities.

In [61] the authors consider a fully discrete system and construct a cell-to-cell coupling matrix whose coefficients depend on the biophysical parameters of the system. To do so, they assume a ligand-limited regime with a "thin-gap" approximation (e.g. a value for H much smaller than the length scale of the system), they also assume a separation among the timescales of the elements of the system such that S and C are the fast variables, therefore neglecting their time derivatives. They were able to construct a coupling matrix for the system that would allow for cell-to-cell signal transmission, this matrix is explicitly constructed for two specific geometries (square and hexagonal), but it has more general validity. For this model, they can find stable solutions (as clusters of neighbor cells) of the discrete system, and also made some

qualitative observations about the coupling coefficients, in particular they show the coefficients have rapid decay which suggests an almost nearest neighbor coupling.

Finally, in [53], the authors use an approach similar to [61] to analyze signal propagation. They use a quasi steady-state approximation for the ligand and ligand-receptor complex variables to construct an integral equation for the coupling coefficients for the solution, using Fourier Transform techniques. To solve this integral equation they assume a "thin-gap" configuration and that σ can be approximated by the Heaviside function. Then they are able to find discrete traveling waves solutions of the system, and study their propagation or failure in terms of the parameters of the problem. In particular, their reduced, nondimensional problem is characterized by two parameters, one of which represents the threshold of the Heaviside function. As a result, they found that there is no signal propagation if this threshold is outside of a certain range (independently of the other parameters of the analyzed problem). This result is due to the pinning caused by the discreteness of the model [53, 42].

2.3 Model Simplification and Analysis

We will now start our analysis by using an approach similar to [62, 61, 53] to study signal transmission in a reduced version of the model given in equations (2.4)-(2.8).

The multidimensional nature of the vectors S , P , C , and R in the general model (2.4-2.8) makes it extremely difficult to study. However, it is still possible to obtain meaningful qualitative results from the analysis of a simpler configuration in which there is only one type of ligand, empty receptor, ligand-receptor complex, and one intracellular species (protease) [62, 61, 53]. This is the configuration that we are going to study.

Here, we consider a purely diffusive system (in Chapter 4 we will add a degradation term) for the ligand (e.g. $f(S) = 0$), and neglect the diffusive component of the ligand-receptor complexes (e.g. $D_C = 0$ and $\gamma(C, P) = 0$). Also, we uncouple

the terms relative to protease production and ligand release. For the first term, we assume that the production of intracellular protease is characterized by a sigmoidal function which only depends on the number of complexes (as opposed to both P_i and C in (2.6)) multiplied by a constant which represents the maximum rate of protease production. The term for ligand release in (2.8) is simplified by using a mass-action type dynamics with a constant rate (g_S), representing the rate of ligand release.

Under these assumptions (and in the continuum approximation), the general model in equations (2.4)-(2.8) reduces to:

$$\begin{aligned} \frac{\partial S}{\partial T} &= D\nabla^2 S, & \frac{\partial S}{\partial Z}\Big|_{Z=H} &= 0, \\ (D\frac{\partial S}{\partial Z} - k_{on}RS)\Big|_{Z=0} &= -k_{off}C - g_S P, \end{aligned} \tag{2.9}$$

$$\frac{\partial C}{\partial T} = -(k_{off} + k_{ec})C + k_{on}R\bar{S}, \quad \bar{S} = S(X, Y, 0, T),$$

$$\frac{\partial P}{\partial T} = -k_P P + g_P \sigma(C).$$

We can further reduce the model by considering a ligand-limited regime, where the number of available receptors is always in excess of the free ligands (in this case R is constant as opposed to the study [62]) and that ligand diffusion, and ligand-receptor complexes distribution are independent of Y , thus eliminating one independent variable. Also, we can use a well-known result for EGFR epithelium stating that the time scale of formation, dissociation, and internalization of ligand-receptor complexes (represented by k_{on} , k_{off} , and k_{ec} respectively) is fast compared to the time scale of protease production (k_p) [88]. Then, we can use a quasi steady-state approximation for C and drop the derivative term. This approximation is quantitatively confirmed in Table 2.2, which shows some of the parameter values obtained in [61, 74] for the epithelium of the egg of *Drosophila Melanogaster*.

Table 2.2 Typical value of the parameters of the EGFR system for the *Drosophila* oocyte [61, 74].

Parameter	Typical Value	Description
A	$2.5 \times 10^{-7} \text{ cm}^2$	Cell Area
D	$1 \times 10^{-7} \text{ cm}^2 \text{ s}^{-1}$	Ligand Diffusivity
H	$5 \times 10^{-5} \text{ cm}$	Height of extracellular medium
k_{on}	$0.1 \text{ nM}^{-1} \text{ min}^{-1}$	Rate of Forward Binding
R	10^4	Number of Receptors per Cell Surface
k_{off}	0.1 min^{-1}	Rate of Backward Binding
k_{ec}	0.1 min^{-1}	Rate of Complex Internalization
k_P	0.03 min^{-1}	Protease First Order Degradation Rate

Applying these assumptions to (2.9) gives a new simplified model:

$$\frac{\partial S}{\partial T} = D \left(\frac{\partial^2 S}{\partial X^2} + \frac{\partial^2 S}{\partial Z^2} \right), \quad \frac{\partial S}{\partial Z} \Big|_{Z=H} = 0,$$

$$\left(D \frac{\partial S}{\partial Z} - k_{on} R S \right) \Big|_{Z=0} = -k_{off} C - g_S P,$$

(2.10)

$$0 = -(k_{off} + k_{ec}) C + k_{on} R \bar{S}, \quad \bar{S} = S \Big|_{Z=0},$$

$$\frac{\partial P}{\partial T} = -k_P P + g_P \sigma(C).$$

This model is still fully dimensional and is characterized by ten parameters. We can reduce the number of parameters by standard dimensional analysis. This analysis leads to the introduction of the following non-dimensional variables:

$$x = X/L, \quad z = Z/L, \quad h = H/L, \quad t = T \cdot k_P, \quad L = D/Rk_{on},$$

$$P = \frac{g_P}{k_P} p, \quad S = \frac{g_P g_S (k_{off} + k_{ec})}{k_{on} R k_P k_{ec}} s, \quad C = \frac{g_P g_S}{k_P k_{ec}} c,$$

where L is the unit length of the system, and can be directly derived from the non-dimensionalization process. We should also mention that this length scale can also be measured experimentally through a stochastic approach as described in [10].

We can now re-write the system in a more compact form by introducing the two non-dimensional parameters:

$$\alpha = \frac{L^2 k_P}{D}, \quad \beta = \frac{k_{ec} L k_{on} R}{D(k_{off} + k_{ec})}, \quad (2.11)$$

and then obtain:

$$\alpha \frac{\partial s}{\partial t} = \frac{\partial^2 s}{\partial x^2} + \frac{\partial^2 s}{\partial z^2}, \quad \frac{\partial p}{\partial t} = -p + \sigma(c), \quad (2.12)$$

$$\left(\frac{\partial s}{\partial z} - \beta s\right)\Big|_{z=0} = -\beta p, \quad \frac{\partial s}{\partial z}\Big|_{z=h} = 0.$$

This system can be further reduced by assuming $H \ll L$ (e.g. $h \ll 1$), i.e. that the height of the extracellular space is small compared to the dynamical length scale of the system. This assumption implies that diffusing ligand molecules stay close to the cell layer. Therefore, they are mostly present in ligand-receptor complexes, and the long-range signaling is mainly due to the positive feedback generated by the complex formation.

Under this assumption, we can average s between 0 and h through integration with respect to z :

$$\bar{s}(x, t) = \frac{1}{h} \int_0^h s dz. \quad (2.13)$$

Furthermore, we have that $s \approx \bar{s}$, and we can rewrite the equation for the extracellular ligand as

$$\alpha \frac{\partial \bar{s}}{\partial t} = \frac{\partial^2 \bar{s}}{\partial x^2} + \frac{1}{h} \frac{\partial s}{\partial z}\Big|_0^h. \quad (2.14)$$

From the no-flux boundary condition at $z = h$, and the interface boundary condition we can rewrite the last term in (2.14) as:

$$\frac{1}{h} \frac{\partial s}{\partial z} \Big|_0^h = \frac{1}{h} \left(\frac{\partial s}{\partial z} \Big|_{z=h} - \frac{\partial s}{\partial z} \Big|_{z=0} \right) = \frac{1}{h} (-\beta \bar{s} + \beta p). \quad (2.15)$$

And we obtain a one dimensional system of two equations, with two unknowns \bar{s} and p and three parameters α, β , and h . It is also possible to further reduce the number of parameters by re-scaling the space variable: $x \rightarrow x\sqrt{h/\beta}$:

$$\begin{cases} \alpha \frac{\partial \bar{s}}{\partial t} = \frac{\beta}{h} \frac{\partial^2 \bar{s}}{\partial x^2} - \frac{\beta}{h} (\bar{s} - p) \\ \frac{\partial p}{\partial t} = -p + \sigma(\bar{s}) \end{cases} \Rightarrow \begin{cases} \tau \frac{\partial \bar{s}}{\partial t} = \frac{\partial^2 \bar{s}}{\partial x^2} - \bar{s} + p \\ \frac{\partial p}{\partial t} = -p + \sigma(\bar{s}) \end{cases}, \quad (2.16)$$

where $\tau = \alpha h/\beta$.

As a final step, we drop the bar from s (for ease of notation), and we are left with the system below:

$$\begin{cases} \tau \frac{\partial s}{\partial t} = \frac{\partial^2 s}{\partial x^2} - s + p \\ \frac{\partial p}{\partial t} = -p + \sigma(s) \end{cases} \quad (2.17)$$

To study this reduced system we need to have an analytical expression for σ . This is a sigmoidal function that describes the protease production due to signaling by ligand-receptor complexes, and can be represented through the Hill function with a prescribed coefficient (n) and threshold (a) [41, 23, 37]:

$$\sigma(s) = \frac{s^n}{a^n + s^n}. \quad (2.18)$$

The Hill function for $a = 1/2$ and different values of the Hill coefficient n is given in Fig. 4.11. From this figure we notice how, even for small values of n , we have a nice sharp threshold. This sharpness increases as the Hill coefficient increases, and in the limit $n \rightarrow \infty$ it is the same as the Heaviside function centered at a .

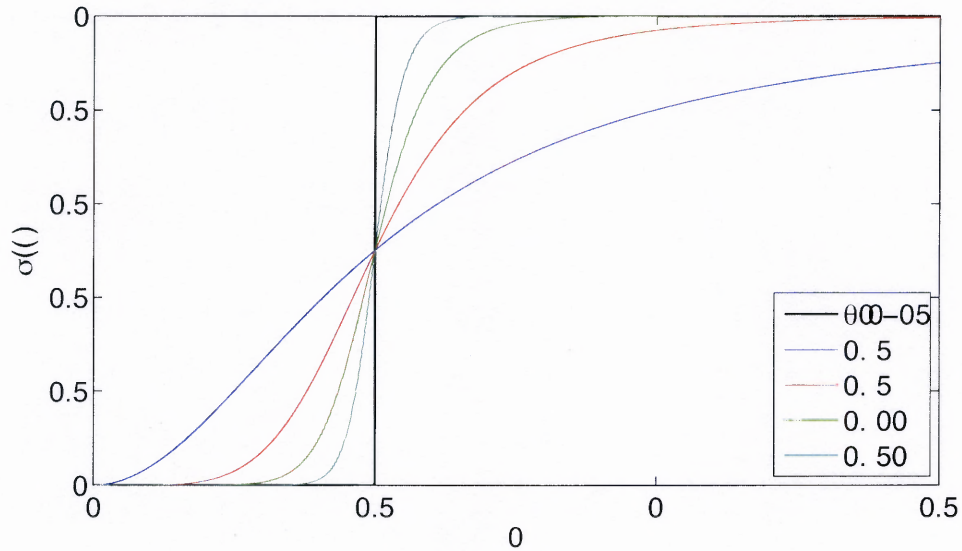


Figure 2.2 Behavior of the Hill function for fixed $a = 1/2$. Notice how as n increases toward infinity, the Hill function approaches the Heaviside function centered at a (thick black line).

This fact is of central importance for an analytical study of (2.17), since by approximating σ with the Heaviside function, we can analytically find important special solutions of (2.17), and then validate these analytical results through numerical simulations run with the Hill function for σ , as it was done for the analogous (to (2.12)) discrete system with $\alpha = 0$ in [61].

2.4 Traveling Wave Solutions

When looking for analytical solutions to (2.17) we are motivated by the studies by Fife and McLeod [25, 26, 27] who showed that under certain conditions, the asymptotic behavior of the solutions to the equation $u_t - u_{xx} - f(u) = 0$ is given by travelling wave fronts with constant speed. This type of behavior of solutions of nonlinear evolution equations is also found in many other biological systems [41, 40] and in particular for the epithelium problem analyzed in [61].

To study system (2.17) analytically in terms of traveling fronts we use the approximation $\sigma(s) = \theta(s - a)$, where a represents the minimal concentration of ligands such that intracellular protease is produced. Through this approximation, we obtain that this dynamical system has two stable steady states at $s = p = 0$ and $s = p = 1$, we can therefore look for traveling waves that connect these two states monotonically. In particular, we will assume that the traveling fronts for both s and p are decreasing, and therefore connecting $s = p = 1$ at $t = -\infty$ to $s = p = 0$ at $t = \infty$. This assumption is equivalent to having a high concentration of ligand at one extreme of the system that spreads to the rest of the cell layer through the combination of diffusion and system-specific biophysical mechanisms.

Seeking traveling wave solutions requires that we look for solutions of the form $s(x - vt)$, $p(x - vt)$. This is achieved by applying the change of variables $\xi = x - vt$ to (2.17). As a result we obtain a system of two ordinary differential equations as opposed to the original system of PDE's:

$$\begin{cases} -v\tau s' = s'' - s + p \\ -vp' = -p + \theta(s - a) \end{cases} \quad (2.19)$$

where the derivatives are with respect to ξ .

To solve this problem we will use the assumption that s is monotonically decreasing, which implies that $s(\xi) = a$ only at one point, and therefore, we can center the Heaviside function at $\xi = 0$ without any loss of generality (a result of translational invariance). The results for s and p are shown below:

$$p(\xi) = \theta(\xi) \left(1 - e^{\frac{\xi}{v}}\right), \quad \lambda_{1,2} = \frac{-v\tau \pm \sqrt{v^2\tau^2 + 4}}{2} \quad \lambda_2 < 0 < \lambda_1, \quad (2.20)$$

$$s(\xi) = \begin{cases} \left(\frac{v^2 a + (1-a)(v^2 \tau + 1)}{v^2 - v^2 \tau - 1} \right) e^{\lambda_1 \xi} + 1 - \frac{v^2}{v^2 - v^2 \tau - 1} e^{\frac{\xi}{v}} & \xi < 0 \\ a e^{\lambda_2 \xi} & \xi \geq 0 \end{cases} \quad (2.21)$$

We can now find an expression relating the velocity of the traveling fronts to the fixed parameters a and τ , by using that $s(0) = a$:

$$a = \frac{2v - (-v\tau + \sqrt{v^2 \tau^2 + 4})(v^2 \tau + 1)}{2\sqrt{v^2 \tau^2 + 4}(v^2 - v^2 \tau - 1)}. \quad (2.22)$$

The qualitative behavior of v is given in Figs. 2.3 and 2.4, where v is plotted as a function of a for selected values of τ . From these figures we notice that there is no wave propagation for $a = 0.5$. This result is the same as the one obtained for the discrete problem in [53].

We are now going to check the result of Eq. (2.22) by studying the velocity of the traveling front solutions of (2.17) for the limiting behaviors $\tau \rightarrow 0$ and $\tau \rightarrow \infty$.

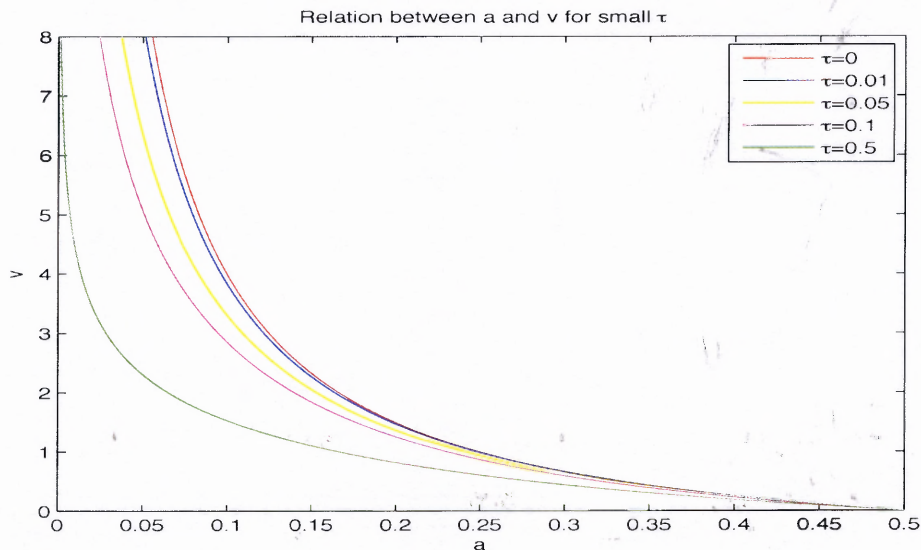


Figure 2.3 Graphs of the velocity of the traveling front solutions as a function of a for small values of τ . Notice the convergence of v toward its asymptotic limit at $\tau = 0$ (red line).

Limit case: $\tau \rightarrow 0$ Let us start by taking the limit $\tau \rightarrow 0$, and solve the system. Under this condition the left-hand side of the first equation of (2.17) becomes negligible:

$$\begin{cases} s_{xx} - s + p = 0 \\ p_t = -p + \sigma(s) \end{cases} \quad (2.23)$$

Looking for traveling wave solutions of the system, we use the transformation $\xi = x - v_0 t$ and the Heaviside function to rewrite the problem as:

$$\begin{cases} s'' - s + p = 0 \\ -v_0 p' = -p + \theta(s - a) \end{cases} \quad (2.24)$$

We first solve for p , using boundness at infinity as boundary conditions. After some algebra we find the following:

$$\begin{cases} p' = \frac{p}{v_0} - \frac{1}{v_0} & \xi < 0 \\ p' = \frac{p}{v_0} & \xi \geq 0 \end{cases} \Rightarrow p(\xi) = \theta(\xi) \left(1 - e^{\frac{\xi}{v_0}}\right). \quad (2.25)$$

We can now use the Green's function approach to find an integral expression for s :

$$s = \frac{1}{2} \int_{-\infty}^{\infty} e^{-|\xi - \xi_0|} p(\xi_0) d\xi_0. \quad (2.26)$$

Solving this integral we get:

$$s(\xi) = \begin{cases} \frac{1}{2} \left[2 - \frac{e^\xi}{1-v_0} + \frac{2v_0^2}{1-v_0^2} e^{\frac{\xi}{v_0}} \right] & \xi \leq 0 \\ \frac{1}{2} \left(\frac{e^{-\xi}}{v_0+1} \right) & \xi > 0 \end{cases}, \quad (2.27)$$

from which we can infer the value of v_0 by using the fact that $s(0) = a$:

$$v_0 = \frac{1 - 2a}{2a}. \quad (2.28)$$

This function is plotted in Fig. (2.3) in red. Note that this problem was solved in [21] in the context of modeling neural networks.

Limit case: $\tau \rightarrow \infty$ This is the case in which s varies extremely slowly as a function of time compared to p , which becomes the fastest changing variable of the system. Biologically, this occurs when protease activation is much faster than ligand diffusion and ligand-receptor binding and unbinding.

In this regime, we need to re-scale the problem by introducing a new time variable $t \rightarrow t/\tau$, which leads to the following system:

$$\begin{cases} \frac{\partial s}{\partial t} = \frac{\partial^2 s}{\partial x^2} - s + p \\ \frac{1}{\tau} \frac{\partial p}{\partial t} = -p + \sigma(s) \end{cases} \quad (2.29)$$

As $\tau \rightarrow \infty$, the left-hand side of the second equation of (2.29) becomes negligible. Then the differential equation for p becomes a simple algebraic equation, and it is straightforward to determine that $p = \sigma(s)$. Using this result, we obtain that s needs to satisfy the following PDE:

$$s_t = s_{xx} - s + \sigma(s). \quad (2.30)$$

This equation was studied by Fife and McLeod in [25, 26, 27], where they proved the existence and uniqueness of traveling wave solutions for (2.30).

Looking for a travelling wave solutions of the form $\xi = x - v_\infty t$, and assuming that $s(0) = a$ with s a monotone decreasing function of ξ , we obtain the following solution for the Heviside nonlinearity centered at a :

$$s(\xi) = \begin{cases} (a-1)e^{\lambda_1 \xi} + 1 & \xi < 0 \\ ae^{\lambda_2 \xi} & \xi \geq 0 \end{cases}, \quad \lambda_{1,2} = \frac{-v_\infty \pm \sqrt{v_\infty^2 + 4}}{2}, \quad (2.31)$$

from which we obtain:

$$v_\infty = \frac{1 - 2a}{\sqrt{a(1 - a)}}. \quad (2.32)$$

This expression of traveling wave velocity for large values of τ is graphically described in Fig. 2.4, and it is a well-known result from [66].

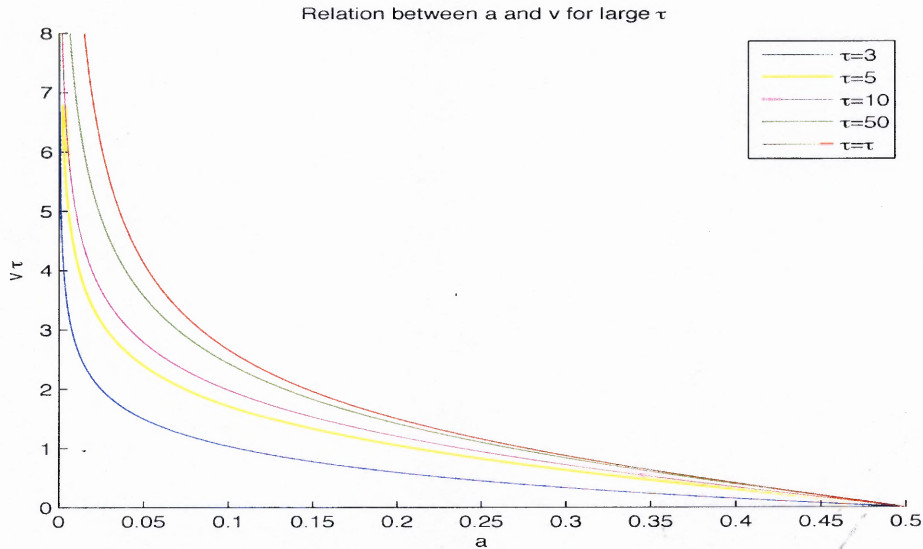


Figure 2.4 Graphs of the velocity of the traveling front solutions as function of a for large values of τ . Notice the asymptotic behavior of v as $\tau \rightarrow \infty$ (red line).

Eqs. (2.28) and (2.32) are exactly the results we would have obtained by taking the respective limits in Eq. (2.22), as we can see graphically in Figs. 2.3 and 2.4.

In general, analytical results like the ones we have obtained above are extremely rare. In this case, by assuming the nonlinearity to be a more realistic Hill function [23], we are unable to solve the simplified model analytically. Under these (common) circumstances, we resort to the use of numerical analysis to shed some light on the solution of the problem. In particular, we can use the analytical results obtained in this section to confirm the validity of the numerical approach.

2.5 A Numerical Study

The goal of this numerical study is to extend what was done analytically in the previous section. In particular, we want to verify the existence of traveling wave solutions and the expression for the velocity given by (2.22) for a more realistic choice of the nonlinearity σ .

We are going to use the Hill function as representation of σ . The use of this function is more appropriate biologically [23], and is also better suited for numerical simulations since it avoids the stiffness problem introduced by the implementation of the Heaviside function. Moreover, the Hill function is a continuous approximation of the piecewise continuous Heaviside function.

We carried out the numerical analysis using two finite difference methods: FTCS (Forward in Time, Central in Space) and Crank-Nicholson. These are two standard numerical schemes. One is explicit, extremely simple to implement but is only conditionally stable (FTCS). The other is implicit and therefore requires a lengthier implementation, but is unconditionally stable (Crank-Nicholson). In the following, we just present in detail the FTCS approach which is suitable for the simple analysis that we are going to perform.

The implementation of this method leads to the following discretization for the equations of s and p :

$$s_i^{m+1} = s_i^m + \frac{\Delta t}{\tau \Delta x^2} (s_{i+1}^m - 2s_i^m + s_{i-1}^m) + \frac{\Delta t}{\tau} (p_i^m - s_i^m),$$

$$p_i^{m+1} = p_i^m + \Delta t \left(-p_i^m + \frac{(s_i^m)^n}{a^n + (s_i^m)^n} \right),$$
(2.33)

where we have used standard finite difference notation in which the subscript represents the discretization in space, while the superscript represents the discretization in time, and Δx , Δt are the space and time steps respectively.

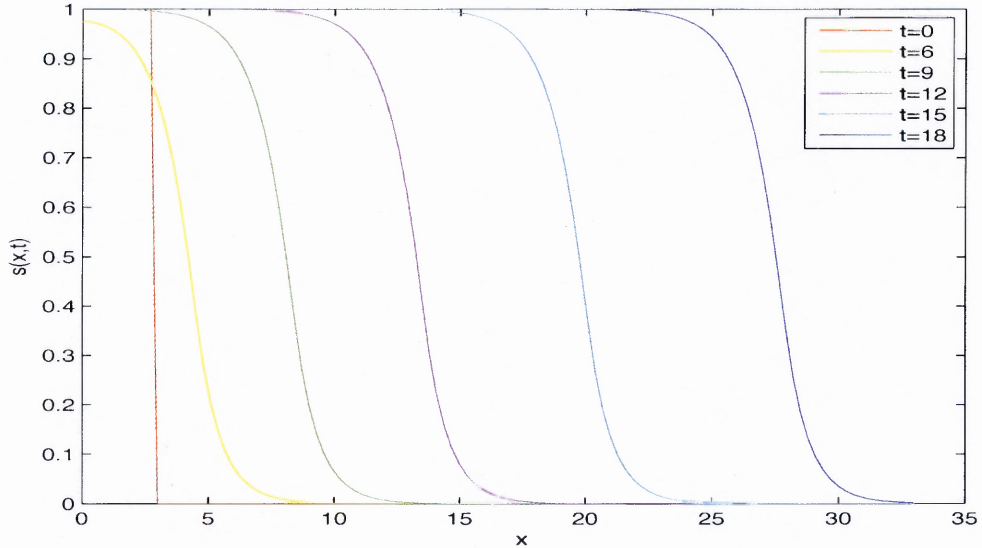


Figure 2.5 Behavior of numerical solutions of (2.17) at different times. These plots are obtained using the FTCS finite difference scheme described by (2.33) with no flux boundary conditions, initial conditions $s(x, 0) = \theta(x - 3)$, $p(x, 0) = 0$, and parameters $a = 0.3$, $\tau = 3$, $n = 20$, $\Delta x = 0.5$, and $\Delta t = 0.04$.

Fig. 2.5 shows the evolution of the numerical solution for s when using the FTCS scheme. This result shows the evolution of the initial data into a traveling front with constant speed, as we discuss next.

To qualitatively analyze the behavior of the traveling fronts shown in Fig. 2.5, we are going to check the change in position of the front itself as a function of time. The results of this analysis are shown in Fig. 2.6 for both s and p . The value $x(t)$ is used to evaluate the evolution of the front and is given by the area under the curve of s and p at a specific time:

$$x_s(t) = \int_0^L s(x, t) dx, \quad x_p(t) = \int_0^L p(x, t) dx. \quad (2.34)$$

From this figure, we can see how, after a short transient, the front starts moving at the same constant speed in accordance with what we have found analytically in (2.20) and (2.21). Moreover, the slopes of the two lines agree up to three signifi-

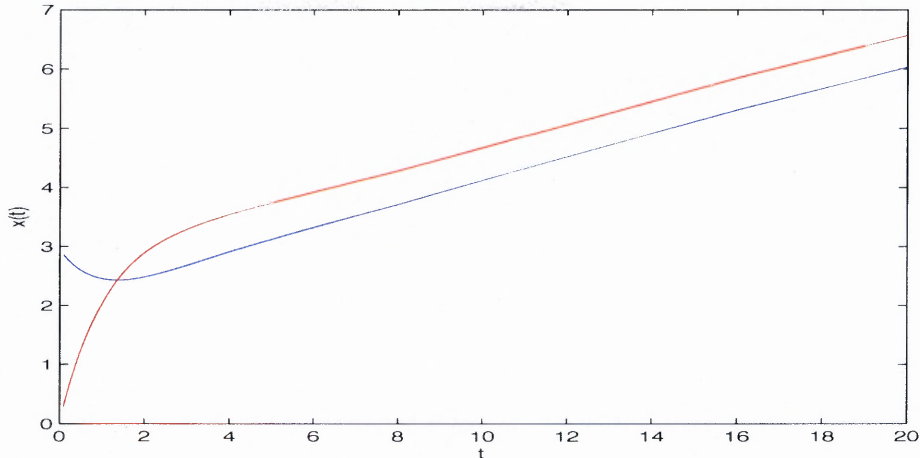


Figure 2.6 Numerical results for the qualitative behavior of the position of the traveling front for both s (blue line) and p (red line), for the same parameters of the simulation in figure (2.5). The slope of the blue line is 0.1797 and the one for the red line is 0.1799. They both agree up to three significant digits to the velocity obtained through (2.22) in the case of the Heaviside nonlinearity, which is 0.179276.

cant digits with the value of the velocity obtained through (2.22) in the case of the Heaviside nonlinearity.

Using numerics we were also able to compare the velocity of the front obtained with the use of the Heaviside function with the numerical velocity obtained from (2.33). In particular we wanted to check how small the Hill coefficient in (2.18) can be taken. After various simulations for different a and τ we found that for n as small as 5, the difference between the analytical and the numerical velocity is no more than $\sim 10\%$. This result is similar to what the authors obtained in [62].

To summarize, we simplified the general model in Eqs (2.4)-(2.8) and analyzed this simplified model both analytically and numerically. We were particularly interested in traveling wave solutions of the simplified model. These solutions are expected for certain parameters of the system because of the particular form of the feedback due to the nonlinearity σ .

In Chapter 4 we will look in more detail at this aspect of the problem, i.e. under what conditions we should expect multiple steady-states and traveling fronts connecting them. We will do this analysis for a model epithelial system similar to the one discussed in this chapter, but with the added mechanism of degradation in the bulk.

In this Chapter we also mentioned the importance of numerics for the analysis of a mathematical model. We used standard finite difference techniques to compare the analytical results obtained for the Heaviside nonlinearity, with the case of a Hill nonlinearity for which we do not have exact solutions. This is a very standard approach that is suitable for a one dimensional study. However, for higher dimensions the use of finite difference methods leads to an increase of many order of magnitudes in computational cost. In these cases, to conduct efficient numerical studies, we need to find alternative ways to cope with the increase in dimensionality of the problem.

In the next Chapter, we will introduce a novel method for the solution of elliptic problems in unbounded domains. And we will extend it to make it spectrally accurate in two dimensions and fourth order in four dimensions, without increasing the method's computational costs.

CHAPTER 3

COMPENSATED OPTIMAL GRIDS

In Section 2.3, we used many assumptions to simplify the model equations. Under these assumptions we were able to make various analytical conclusions about traveling waves solutions of the simplified model. Moreover, we used a straightforward finite difference approach to observe traveling fronts and quantitatively study their properties.

As we move backward along the model simplification, and add complexity to the model by omitting assumptions, we obtain nonlinear dynamical systems that in general cannot be solved analytically and require extensive use of numerical methods. Ultimately, we would have to study spatially three-dimensional models aimed at the reproduction of the signals experimentally observed in the epithelium.

The numerical study of a system of three-dimensional PDEs is a computationally intensive task. In high dimensional contexts, it is pivotal to be able to minimize the storage space and the number of operations with respect to the accuracy that we want to achieve. Failing to do so can lead to a considerable waste of time and computational resources.

For the particular case of the epithelium, we notice that the intracellular dynamics that generates epithelial patterns is regulated by the dynamical behavior of the system at cell surface level, i.e. the ligand mediated ligand release kinetics that characterize these systems. In mathematical terms, the problem of relating the flux of ligands in and out of the cell membrane (i.e. Neumann data) with the concentration of the ligands themselves on the epithelial layer (i.e. Dirichlet data) is the same as the problem of finding the Neumann-to-Dirichlet (\mathcal{N}) operator of the system at the cell surface level. This operator can then be used to replace the dynamics in the ex-

tracellular medium since all its dynamics is contained in the Neumann-to-Dirichlet map.

In essence, the spatially three dimensional problem of intracellular signaling is reduced to a two dimensional one in which the objective is to compute the Neumann-to-Dirichlet map.

Moreover, as we have seen in the previous Chapter, for a wide range of parameters, the mathematical model admits the existence of multiple, often inhomogeneous steady states. For this scenario, we can eliminate the time dependence, thus going from a reaction-diffusion type problem to an elliptic one similar to

$$\Delta u = 0, \quad z > 0, \quad u_z + f(x, y) = 0 \text{ at } z = 0. \quad (3.1)$$

It has been shown [79], that Eq. (3.1) is characterized by the Neumann to Dirichlet map which is given by the negative inverse square root of the negative Laplacian, and this fact is fundamental for the development of optimal grids as we will show below.

In [18], the author observed a relationship between a three point staggered approximation of the Laplacian and the optimal rational approximation of the Neumann-to-Dirichlet map in Fourier space. This observation has led to a novel method for the solution of elliptic boundary problems [38, 19, 50]. This method is called the method of optimal grids and its derivation and properties will start our discussion. After introducing the optimal grid method, we will present the extension we developed in [60]. We called this extension “compensated optimal grids” and we are going to explore its properties and its applications to cell signaling problems.

3.1 Optimal Grids

As mentioned above, the fact that the impedance of the Laplacian on half-space is the negative inverse of the square root of the negative Laplacian is fundamental for

the success of optimal grid application to elliptic problems. Therefore, we will begin by briefly showing the validity of this result.

3.1.1 \mathcal{N} operator for the Laplace equation in half-space [50]

Let us consider the Laplace equation in half-space

$$\frac{\partial^2 u(x, y, z)}{\partial x^2} + \frac{\partial^2 u(x, y, z)}{\partial y^2} + \frac{\partial^2 u(x, y, z)}{\partial z^2} = \Delta_{\perp} u + \frac{\partial^2 u}{\partial z^2} = 0, \quad z > 0, \quad (3.2)$$

with either Dirichlet or Neumann boundary conditions at $z = 0$

$$u(x, y, 0) = \varphi(x, y), \quad \lim_{z \rightarrow 0^+} \frac{\partial u(x, y, z)}{\partial z} = -v(x, y). \quad (3.3)$$

Under certain choices of boundary conditions at $z = 0$ and infinity, this problem has a unique solution. Moreover, there is a one-to-one correspondence between v and φ through the Neumann-to-Dirichlet map [79].

For problem (3.2)-(3.3) we can find a closed form expression of \mathcal{N} by Fourier transforming it with respect to x and y

$$\frac{\partial^2 u_q}{\partial z^2} = |q^2| u_q, \quad u_q(0) = \varphi_q, \quad \varphi_q = \int \int e^{iq_1 x + iq_2 y} \varphi(x, y) dx dy. \quad (3.4)$$

If we assume boundness at infinity, the above problem has the solution $u_q = \varphi_q e^{-|q|z}$. Then, we can use the definition of Neumann data v in Eq. (3.3) and find that the Fourier transform of the impedance is $\mathcal{N}_q = 1/|q|$

$$v = - \lim_{z \rightarrow 0^+} \frac{\partial u(x, y, z)}{\partial z} = \lim_{z \rightarrow 0^+} \varphi_q |q| e^{-|q|z} = |q| \varphi_q. \quad (3.5)$$

We can now find the Neumann-to-Dirichlet map by inverting \mathcal{N}_q , obtaining

$$\mathcal{N}v(x, y) = \frac{1}{2\pi} \int_{\mathcal{R}^2} \frac{v(\vec{x}')}{|\vec{x} - \vec{x}'|} d^2 \vec{x}', \quad \vec{x} = (x, y). \quad (3.6)$$

However, $\mathcal{N}_q = 1/|q| = 1/\sqrt{\lambda_q}$, where $\lambda_q = q_1^2 + q_2^2$ are the eigenvalues of $-\Delta_{\perp}$, and \mathcal{N} is the inverse square root of the negative transversal Laplacian in operator

sense:

$$\mathcal{N} = (-\Delta_{\perp})^{-1/2}. \quad (3.7)$$

Now that we know the form of the Neumann-to-Dirichlet map, we need to show how it comes in to play when trying to optimize the solution of an elliptic problem such as (3.1).

3.1.2 Connection between \mathcal{N} and the numerical solution of elliptic problems

Let us look at problem (3.1) in two dimensions (e.g. we could assume planar fronts independent of y), and solve the problem numerically by first transforming it to Fourier space with respect to x , and then discretizing it using a three points staggered grid in the vertical direction. Thus obtaining the semidiscrete scheme:

$$\frac{1}{h_k} \left(\frac{u_q^{k+1} - u_q^k}{h_{k+1/2}} - \frac{u_q^k - u_q^{k-1}}{h_{k-1/2}} \right) - \lambda u_q^k = 0, \quad k = 1, \dots, n-1, \quad (3.8)$$

$$\left(\frac{u_q^0 - u_q^{-1}}{h_{-1/2}} \right) - h_0 \lambda u_q^k = -f_q, \quad u_q^n = 0. \quad (3.9)$$

We now want to optimize the above scheme to achieve the best approximation of $u_q(0)$, since we are only interested in the Dirichlet data. Therefore, we want to minimize the error at $k = 0$ with respect to the L_2 norm. This error can be estimated as in [38] if we assume that the data has compact support in Fourier space:

$$\|u_q(0) - u_q^0\|_2 \leq \|f_q\| \max_{\lambda \in (\lambda_{min}, \lambda_{max})} |\mathcal{N}_q^n - \lambda^{-1/2}|, \quad (3.10)$$

where \mathcal{N}_q^n is the discrete Fourier transform of the impedance operator, and λ_{min} , λ_{max} represent the extreme of the spectral interval that we want to resolve using this approach.

In essence, the estimate in Eq. (3.10) tells us that to minimize the error of approximating $u_q(0)$ with u_q^0 within a certain spectral interval, we need to select the h_k 's in such a way that they minimize the error in the approximation of the inverse square root on that same spectral interval. This can be achieved by choosing the h_k 's to form the optimal rational approximation of the square root [18].

In particular, we say that $R(x)$ is an optimal rational approximation of $f(x)$ in some interval $[a, b]$, if:

$$\max_{x \in [a, b]} \left| \frac{R(x) - f(x)}{f(x)} \right| = \min_{R_{n-1, n}} \max_{x \in [a, b]} \left| \frac{R_{n-1, n}(x) - f(x)}{f(x)} \right|, \quad (3.11)$$

where, $R_{n-1, n}(x)$ are rational functions of degree $n - 1$ by n . This definition of optimality leads to the so-called Zolotarev grids [59].

For our specific case we have $f(\lambda) = \mathcal{N}(\lambda) = 1/\sqrt{\lambda}$, and we can rewrite (3.11) as:

$$\max_{\lambda \in [a, b]} \left| \sqrt{\lambda}R(\lambda) - 1 \right| = \min_{R_{n-1, n}} \max_{x \in [a, b]} \left| \sqrt{\lambda}R_{n-1, n}(x) - 1 \right|. \quad (3.12)$$

It can be proved that an optimal rational approximation for $1/\sqrt{\lambda}$ exists and is unique. Also its convergence to the approximated function is exponentially fast (see [38] and references therein). We can evaluate $R(\lambda)$ in more than one way. For example we could use the explicit Zolotarev solution, or implement a code that evaluates the optimal rational approximant numerically using Remez algorithm [13]. We used the latter approach, especially since we already have a Mathematica implementation for this task [50]. For example, the (nearly) optimal approximant of the inverse square root in $[1, 10^4]$ with $n = 4$ is [50]:

$$R(\lambda) = \frac{32}{7 \left(\lambda + \frac{197}{9} \right)} + \frac{146}{7 \left(\lambda + \frac{3655}{8} \right)} + \frac{2929}{16 \left(\lambda + \frac{118697}{8} \right)} + \frac{16}{13 \left(\lambda + \frac{2}{3} \right)}. \quad (3.13)$$

At first, the above expression does not seem to help in identifying the steps h_k 's. However, $R(\lambda)$ is a Stieltjes function and can be represented as an S fraction

[38], i.e.:

$$R(\lambda) = \frac{1}{\lambda h_0 + \frac{1}{h_{1/2} + \frac{1}{\lambda h_1 + \dots + \frac{1}{h_{n-1/2}}}}}, \quad (3.14)$$

where the coefficients h_k 's have been obtained from $R(\lambda)$ through a polynomial division [38].

This representation allows us to link the optimal rational interpolant of the Neumann-to-Dirichlet operator of (3.1) to the finite difference scheme (3.8)-(3.9). In fact, Druskin in [18] noticed that Eq. (3.14) is the impedance function for the staggered three point discretization of problem (3.1) given by Eqs. (3.8)-(3.9). To see that, we can change Eq. (3.9) to be $(u_q^0 - u_q^{-1})/h_{-1/2} = -1$, then for the case $n = 1$ substituting this expression in Eq. (3.8) we obtain:

$$u_q^0 = \frac{1}{\lambda_q h_0 + \frac{1}{h_{1/2}}}, \quad (3.15)$$

in the same way, for the case $n = 2$ we get:

$$u_q^0 = \frac{1}{\lambda_q h_0 + \frac{1}{h_{1/2} + \frac{1}{\lambda_q h_1 + \frac{1}{h_{1/2}}}}}, \quad (3.16)$$

and so on, obtaining Eq. (3.14) for a general value of n .

The scheme in Eqs. (3.8)-(3.9) is in Fourier space. So, to actually find the Dirichlet data in problem space, we also need to discretize the transversal Laplacian using any appropriate numerical scheme. For instance, we could use the classical three point centered difference scheme on an uniform grid of stepsize h_\perp and length m , thus obtaining

$$\frac{1}{h_k} \left(\frac{u_i^{k+1} - u_i^k}{h_{k+1/2}} - \frac{u_i^k - u_i^{k-1}}{h_{k-1/2}} \right) + \frac{u_{i+1}^k - 2u_i^k + u_{i-1}^k}{h_\perp} = 0, \quad k = 0, \dots, n-1, \quad (3.17)$$

$$\left(\frac{u_i^0 - u_i^{-1}}{h_{-1/2}} \right) = -f_i, \quad u_i^n = 0, \quad i = 0, \dots, m. \quad (3.18)$$

3.1.3 Convergence of optimal grids

In [38], the authors obtained an asymptotic estimate of the relative error in Eq. (3.10) for large n

$$\max_{\lambda \in (\lambda_{min}, \lambda_{max})} |\mathcal{N}_q^k(\lambda) - \lambda^{-1/2}| = O\left(e^{\left(\frac{\pi^2 n}{\ln(\lambda_{min}/\lambda_{max})}\right)}\right), \quad (3.19)$$

which implies superconvergence within the spectral interval where the rational approximation is computed. Moreover, they showed that even for a small number of gridpoints it is possible to obtain a very accurate approximation of the inverse square root for a broad range of eigenvalues.

We checked this observation by evaluating u_0 in (3.8)-(3.9) for $n = 4$ using three different methods: a tridiagonal solver, the Conjugate Gradient method and a diagonally preconditioned Conjugate Gradient method. We used these three methods because in practical applications we will often embed the optimal grid approach into an implicit scheme (to take advantage of the stability of such schemes), and we wanted to compare their efficiency (we found that the diagonally preconditioned conjugate gradient method is the best choice). Note that the use of optimal grids maintains the sparseness of the differentiation matrix, and that the optimal grid differentiation matrix is symmetric in weighted space, i.e. under multiplication of the k -th row by h_k .

Figure 3.1 shows the relative error of these three methods as a function of λ . From it, we can see that the error never exceeds 5.5×10^{-3} on the interval $[1, 10^4]$, although we only used four points to approximate the function.

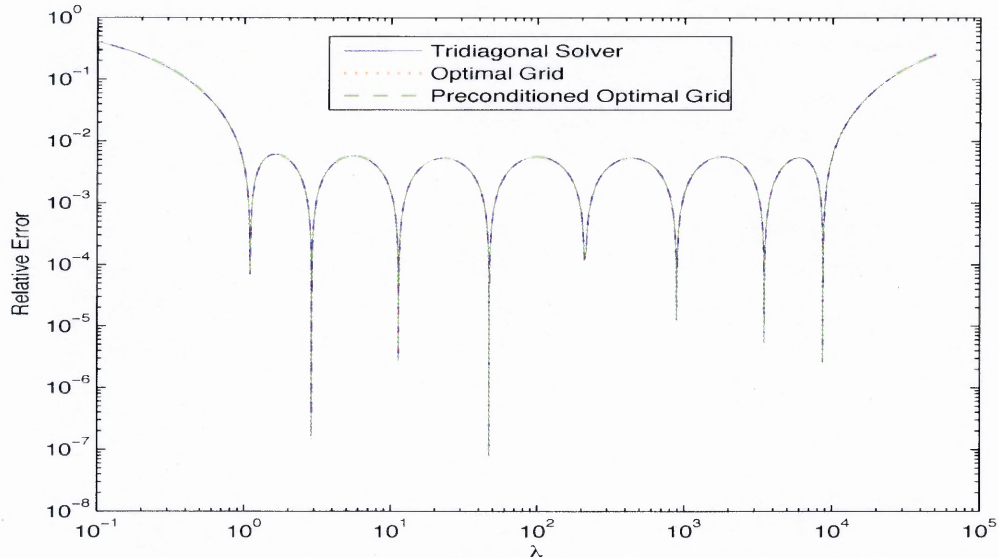


Figure 3.1 Relative Error in approximating $R(\lambda)$ with different methods.

3.1.4 Optimal geometric grids

We end this introduction to Optimal Grids with one more result derived in [38], which consists of a closed form formula for the steps of the rational approximation:

$$h_0 = \frac{h_\perp}{1 + e^{\pi/2\sqrt{n}}}, \quad h_{1/2} = O(h_\perp), \quad h_{i+1/2} = h_{i-1/2} e^{\pi/\sqrt{n}}, \quad h_i = \sqrt{h_{i+1/2} h_{i-1/2}}. \quad (3.20)$$

Grids obtained through these formulas are called Optimal Geometric Grids, and are asymptotically equivalent to the one obtained through Optimal Rational approximation for $n \gg 1$. Since the construction of these grids is straightforward they are often the first choice for the discretization in the z -direction.

3.2 Compensation

We have shown how optimal grids can achieve exponential convergence in approximating the Neumann-to-Dirichlet map. However, when we apply the method to practical problems, we embed it into a broader numerical algorithm, e.g. a three-dimensional solver, in which one dimension is discretized using optimal grids and the

other two by using some other method. It is this addition that introduces an extra source of error that can disrupt the superconvergence of the optimal grid approach.

For example, let us suppose that we need to solve the problem

$$\Delta u = 0 \text{ for } z > 0, \quad u_z + f(x, y, z) = 0 \text{ at } z = 0. \quad (3.21)$$

This type of problem could arise when looking for stationary solutions of the ligand dynamics described in the model in Chapter 2 under certain assumptions, such as a cubic-like function for the secretion of the signal, and fast ligand receptor binding. To make the example simpler, we will only consider plane wave solutions that are independent of y , which are:

$$u(x, z) = \frac{1}{q} e^{iqx - qz}, \quad f(x) = e^{iqx}, \quad q > 0. \quad (3.22)$$

To solve Eq. (3.21) numerically, we take a uniform grid with stepsize h_\perp in the x direction, and a Zolotarev¹ grid in the z direction to discretize our two-dimensional domain. We use a three point centered finite difference to approximate the Laplacian in x (we will indicate it with Δ_\perp), and use a staggered three point approximation for the Laplacian in the z direction:

$$\frac{1}{h_k} \left(\frac{u_i^{k+1} - u_i^k}{h_{k+1/2}} - \frac{u_i^k - u_i^{k-1}}{h_{k-1/2}} \right) + \frac{u_{i+1}^k - 2u_i^k + u_{i-1}^k}{h_\perp^2} = 0, \quad \left(\frac{u_i^0 - u_i^{-1}}{h_{-1/2}} \right) = -f_i, \quad (3.23)$$

Proceeding as in Section 3.1, we find that the solution at $z = 0$ is:

$$u(x, 0) = F(\lambda)f \approx F_n(\lambda_q)e^{iqx}, \quad (3.24)$$

where $F(\lambda)$ is the exact impedance function for problem (3.21) and $F_n(\lambda_q)$ is the approximation of the impedance function using a Zolotarev grid of size n . As for λ_q , we know that its exact value is q^2 . However, because of the discretization of the

¹We will identify Optimal grids as Zolotarev grids to avoid confusion with Optimal Geometric grids

Laplacian in the x direction we have an eigenvalue:

$$\lambda_q = \frac{2 - 2 \cos qh_\perp}{h_\perp^2}. \quad (3.25)$$

From this result, we can choose λ_{max} , λ_{min} , and n to resolve a specific range of wave vectors. Moreover, we can use the asymptotic error estimate given in [38] to quantify the error introduced by the optimal grid approximation. This asymptotic result, together with the error due to the centered finite difference approximation of the second derivative in x , give us the relative error for scheme (3.23):

$$\frac{\|u(x, 0) - u_i^0\|}{\|u_i^0\|} \approx O(h_\perp^2) + O\left(e^{\frac{-\pi^2 n}{\ln(1/h_\perp)}}\right), \quad (3.26)$$

where the first term on the right hand side is due to the finite difference approximation and the second is due to the use of Zolotarev grids.

From this error estimate we can see that for large enough n , the dominant part of the error comes from the discretization of Δ_\perp . This error is passed to the scheme through the argument of F_n , which is the approximation of the impedance function of the problem F . This is the impedance function that we chose the optimal rational approximation upon.

Is it possible to choose a different impedance function such that the dispersion introduced by the approximation of Δ_\perp vanishes? The answer is yes. We can compensate for the approximation of the Laplacian in the direction orthogonal to the optimal grid by choosing an appropriate impedance function that we will indicate with F_c .

For problem (3.23), we have the following compensated impedance function $F_c(\lambda) \approx F_n(\lambda)$:

$$F_c(\lambda) = \frac{h_\perp}{\arccos\left(1 - \frac{1}{2}\lambda h_\perp^2\right)}, \quad (3.27)$$

which results in:

$$F_n \left(\frac{2 - 2 \cos qh_{\perp}}{h_{\perp}^2} \right) \approx F_c \left(\frac{2 - 2 \cos qh_{\perp}}{h_{\perp}^2} \right) \equiv F(q^2), \quad (3.28)$$

the rightmost term being the exact impedance function. In essence, we are able to completely eliminate the error term due to the approximation of the transversal Laplacian, and because of the convergence properties of the optimal grids, we are able to obtain a spectrally accurate approximation of $u(x, 0)$ (as long as n is big enough).

What we have found is a way to increase the convergence of a method without increasing the mesh or the computational complexity. However, there are a few questions that still need to be addressed regarding this idea. When looking for a rational approximation of the impedance function, we need to select an interval of eigenvalues where we want to solve our problem. How do we determine this interval? Given a certain impedance function, are we guaranteed to be able to find the grid steps for the interval we have chosen?

The choice of an appropriate interval is straightforward in the case of a uniform grid of size m with stepsize h_{\perp} . In this case we can choose:

$$\lambda_{min} = \frac{\pi^2}{m^2 h_{\perp}^2}, \quad \lambda_{max} = \frac{4a^2}{h_{\perp}^2}. \quad (3.29)$$

If we choose $a = 1$ in the above expression of λ_{max} , we resolve all the Fourier modes. This is a very conservative choice and in practice we will choose a value of a smaller than one. In this way we will only approximate the relevant (for the problem we intend to solve) spectral interval.

Once the interval is selected, we need to address the other question, namely, can we find the stepizes h_i 's? The answer is no, at least in general. In fact, for a function to be able to be represented as an S-fraction with positive coefficients (h_i 's), it needs to be a Markov function [38], and the impedance function (3.27) in the interval given above is not a Markov function in general unless $a < a_c < 1$ where

a_c is some critical value that depends on the nature of the problem [60]. However, if we can find a spectral interval in which $F_c \approx F$ (which is the case if we take a small enough in Eq. (3.29)), then by continuity of the Zolotarev optimal rational approximant, we should be able to construct an optimal grid for F_c (which we will call compensated optimal grid to distinguish it from the Zolotarev one).

This issue represents a small price to pay to achieve spectral convergence through compensated optimal grids, since in all encountered problems we can always selected values of a and n to resolve the spectral interval of choice.

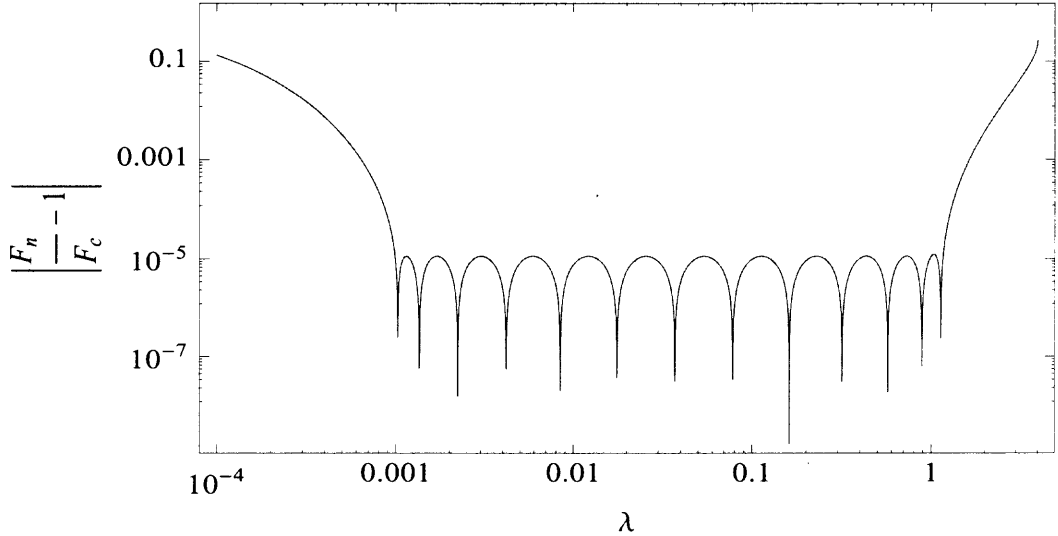


Figure 3.2 Relative error in approximating $F_c(\lambda)$ in Eq. (3.27).

We have implemented this approximation procedure for the impedance function F_c in (3.27), using the Remez algorithm [13], and were able to generate optimal rational approximants for a broad range of values of m and n . For, example the (nearly) optimal rational approximant for F_c with $h_{\perp} = 1$, $n = 6$, $m = 100$, and

$a = 0.5$ on the interval from (3.29) is given by

$$F_n(\lambda) = \frac{0.0270636}{\lambda + 0.00203588} + \frac{0.0548426}{\lambda + 0.0113022} + \frac{0.120905}{\lambda + 0.0559717} + \frac{0.308876}{\lambda + 0.294184} + \frac{1.86027}{\lambda + 2.69169} + \frac{0.0166147}{\lambda + 0.00015466}, \quad (3.30)$$

where we found this value of a to be roughly the maximum value at which the algorithm converged to a solution with negative poles and positive residues. The relative error in approximating F_c in (3.27) on the spectral interval in (3.29) did not exceed 1.2×10^{-5} (see Fig. 3.2), showing the usual high performance of optimal grids [38]. Also, following the procedure of [50], we have extracted the grid steps from (3.30), which are given in Table 3.1.

Note that for a fixed ratio of λ_{\max} to λ_{\min} , the grid steps corresponding to different values of h_{\perp} can be obtained from those with $h_{\perp} = 1$ by a simple rescaling. This is the approach that we have used for all the numerical studies carried out in this work, and because of its versatility it is also the approach that should be used in conjunction with compensated optimal grids .

Table 3.1 The optimal grid steps corresponding to (3.30).

h_0	$h_{1/2}$	h_1	$h_{3/2}$	h_2	$h_{5/2}$
0.41866	1.11746	1.76275	2.61108	3.77355	5.44027
h_3	$h_{7/2}$	h_4	$h_{9/2}$	h_5	$h_{11/2}$
7.89149	11.5611	17.1795	26.1855	42.328	82.559

3.3 Convergence of Compensated Optimal Grids

3.3.1 Comparison with Zolotarev and optimal grids

We now want to verify the advantage that the introduction of the compensated impedance function F_c gives by comparing the performance of the compensated optimal grids constructed with that of the “uncompensated” Zolotarev and geometric

optimal grids [38, 50] of the same size applied to the plane wave solutions of the Laplace's equation on a half-plane.

As a model problem for this comparison we use the boundary-value problem

$$\frac{\partial^2 u}{\partial x^2} + \frac{\partial^2 u}{\partial z^2} = 0 \text{ in } [0, \pi] \times [0, \infty), \quad \frac{\partial u}{\partial z} \Big|_{z=0} = -\cos qx, \quad \frac{\partial u}{\partial x} \Big|_{x=0, L} = 0, \quad (3.31)$$

where $q = 1, 2, \dots$.

We discretize the problem by using the centered finite difference approximation of the second derivative in x with a uniform grid of size m , and stepsize h_\perp . For the Laplacian in the vertical direction, we use the three point staggered stencil with n optimal steps h_k 's (which can be either compensated, Zolotarev, or geometric). That is,

$$\frac{u_{j+1}^k - 2u_j^k + u_{j-1}^k}{h_\perp^2} + \frac{1}{h_k} \left(\frac{u_j^{k+1} - u_j^k}{h_{k+1/2}} - \frac{u_j^k - u_j^{k-1}}{h_{k-1/2}} \right) = 0, \quad k \geq 1, \quad (3.32)$$

$$\frac{u_{j+1}^0 - 2u_j^0 + u_{j-1}^0}{h_\perp^2} + \frac{1}{h_0} \left(\frac{u_j^1 - u_j^0}{h_{1/2}} + \cos qx_j \right) = 0, \quad x_j = jh_\perp, \quad (3.33)$$

with $j = 0, 1, \dots, m$ and $k = 0, 1, \dots, n-1$, the value of $h_\perp = \pi/m$, and the boundary conditions

$$u_{-1}^k = u_1^k, \quad u_{m+1}^k = u_{m-1}^k, \quad u_j^n = 0. \quad (3.34)$$

We solved (3.32) – (3.34) using the diagonally preconditioned conjugate gradient method [33] with a number of different kinds of choices of h_k : compensated grids with $n = 8$ and $n = 10$ optimized on the spectral interval $[\frac{m^2}{10000\pi^2}, \frac{m^2}{10\pi^2}]$; a compensated grid with $n = 14$ optimized on the spectral interval $[\frac{m^2}{20000\pi^2}, \frac{m^2}{20\pi^2}]$; and optimal geometric and Zolotarev grids with different values of n , with Zolotarev grids optimized for the condition number $\lambda_{\max}/\lambda_{\min} = 10^3$, where both the geometric and the Zolotarev grids were scaled so that $h_{1/2} = h_\perp$. Note that the accuracy of the rational approximation for the compensated grids was 6×10^{-9} for $n = 10$ and 1.6×10^{-12} for $n = 14$, while

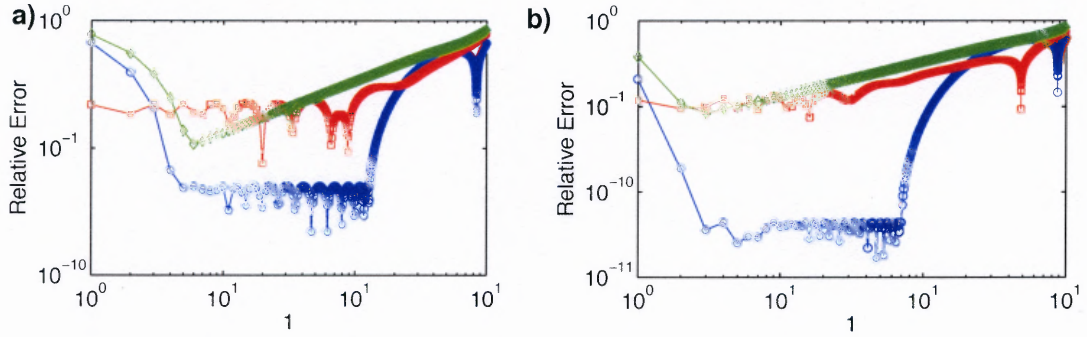


Figure 3.3 Comparison of the performance of different optimal grids for solving the boundary-value problem (3.31) with m fixed. In both (a) and (b), the relative error of the solution is shown for all admissible values of q ; $n = 8$ in (a), while $n = 14$ in (b). In all cases $m = 1000$.

the accuracy of the Zolotarev's grid's approximation of the square root for $n = 14$ was also found to be 1.6×10^{-12} .

We first a series of simulations for different values of q at fixed $m = 1000$ and plotted the relative error of the solution. The results are presented in Fig. 3.3, where the left panel shows the comparison of the data obtained using compensated, geometric, and optimal grids with $n = 8$, while the right panel shows the same results with $n = 14$. The blue circles represent compensated optimal grid results, the red squares are geometric optimal grid data, and the green diamonds show the performance of Zolotarev optimal grids.

From this analysis, we observe the higher performance of compensated grids as compared to the other two choices of grid. For $n = 8$, the relative error does not exceed 10^{-6} in the case of compensation for the whole acceptable spectral interval, while, for $n = 14$ the error is reduced to roughly 10^{-12} for all wave vectors within the spectral interval for which the grid has been constructed.

The results of the analysis in Fig. 3.3 also confirms the result from Eq. (3.26), where it is shown that the main source of error is due to the transverse Laplacian and not the rational approximation of the impedance function. In fact, when increasing

the number of points in the rational approximation, the accuracy of the geometric and Zolotarev grid results does not improve, as opposed to the compensated grid results.

Another effect that we notice in Fig. 3.3 is the deterioration of the performance of the compensated grid at the two extremes of the spectral interval, e.g. for large and for small wave vectors q . The discrepancy for large wave vectors is due to the fact that the spectral interval of optimization was chosen so that $a \simeq 0.1$ in Eq. (3.29), so that the highest frequencies of the discrete problem were not completely resolved. On the other hand, the discrepancy at small wave vectors is a result of the resolution limit of the optimal grid set by the condition number of the optimization interval. For all the grids used in Fig. 3.3 this condition number was set to 10^3 . Note that similar deterioration in performance also occurs in the case of the Zolotarev grids because of the same nature of the approximation procedure. On the other hand, the geometric grids do slightly better at small wavevectors, since optimal geometric grids have a tendency to over-resolve low frequencies.

To further illustrate an essentially pseudo-spectral character of the accuracy of the compensated optimal grids, we performed a convergence study of the solution at fixed q as the value of m is increased. The results for $q = 4$ and several choices of optimal grids are shown in Fig. 3.4. From these results, we observe how the error of the geometric and Zolotarev grids depends on the choice of discretization of the transverse Laplacian, and in this case, it is of second order with respect to the size m of the discretization. Meanwhile, the error of the compensated optimal grid quickly reduces to the value determined by the maximum resolution of the rational approximant, and it starts deteriorating only when m is big enough so that $q = 4$ does not belong to the spectral interval resolution. Also note how the geometric grid has a wider interval of resolution; this is again an effect of the limiting choices of a in Eq. (3.29) that compensation introduces.

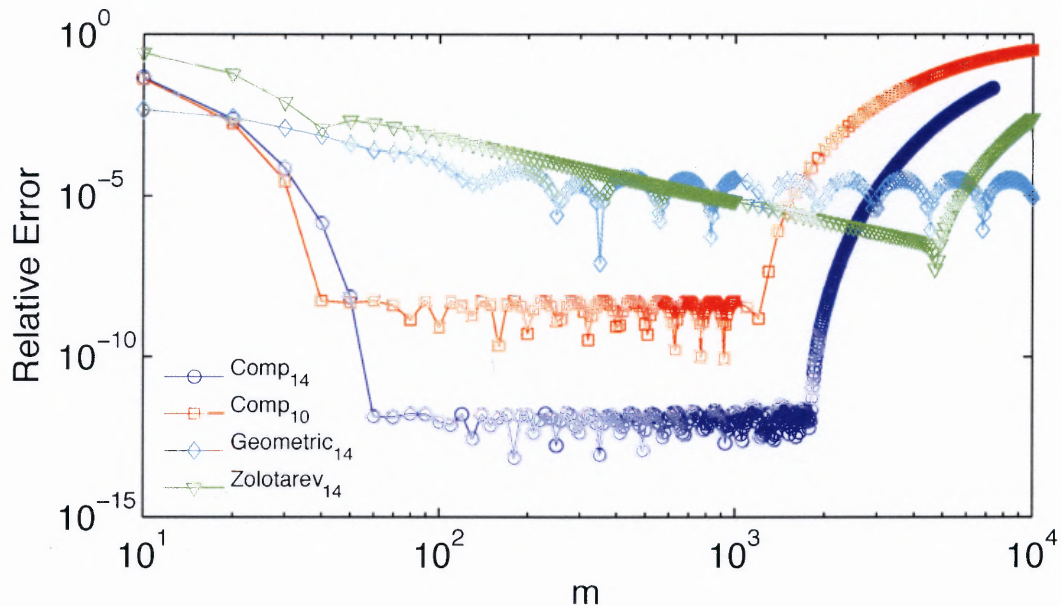


Figure 3.4 Convergence study for the solution of (3.31) with $q = 4$. Results for the compensated grids with $n = 10$ and $n = 14$, as well as geometric and Zolotarev grids with $n = 14$ are shown.

We have shown that through compensated optimal grids we are able to obtain spectral accuracy for the Dirichlet data without having to increase the size of the discretization. Also, we can achieve very high accuracy with very small grid size, e.g. the grid with just $n = 10$ nodes already achieves single-precision accuracy for the range of $m \sim 10 \div 10^3$ in the simulation of Fig. 3.4.

These results were obtained for a very straightforward linear problem. However, many practical applications of mathematical modeling involve the analysis of nonlinear problems, such as cell signaling. Can we successfully apply this compensation approach to more complex nonlinear systems?

3.3.2 An exactly solvable nonlinear problem

To answer this question, we looked in the literature for a nonlinear problem with a known exact solution, and also for a problem whose solution has the properties of a sharp stationary front (at least in some limits of the parameters of the problem).

Toland [81] found that for the nonlinear Neumann boundary-value problem

$$\frac{\partial^2 u}{\partial x^2} + \frac{\partial^2 u}{\partial z^2} = 0 \text{ in } \mathbb{R} \times [0, \infty), \quad \frac{\partial u}{\partial z} + \sin u = 0 \text{ on } z = 0, \quad (3.35)$$

all bounded solutions can be expressed in closed form. In particular, the author showed that all non-constant solutions of Eq. (3.35) are either non-periodic in x , in which case we obtain the Peierls solutions [58]

$$u(x, z) = \pm 2 \tan^{-1} \left(\frac{x+a}{1+z} \right) + 2\pi n, \quad x \in \mathbb{R}, z > 0, \quad (3.36)$$

or, if we pick $\alpha \in (1, 2)$, all the solutions are periodic in x with period (π/δ) , and are of the form

$$u(x, z) = \pm u_\alpha(x+a, z) + 2\pi n, \quad a \in \mathbb{R}, n \in \mathbb{N}, \quad (3.37)$$

where

$$u_\alpha(x, z) = 2 \left[\tan^{-1} \left(\frac{\tan \delta x}{\Gamma_\alpha(z)} \right) - \tan^{-1} (\Gamma_\alpha(z) \tan \delta x) \right], \quad (3.38)$$

and

$$\Gamma_\alpha = \left(\frac{\gamma + \tanh \delta y}{1 + \gamma \tanh \delta y} \right), \quad \beta = \alpha^2 - 2\alpha, \quad \delta = \frac{1}{2} \sqrt{-\beta}, \quad \gamma = \alpha / \sqrt{-\beta}. \quad (3.39)$$

For our purposes, we are only interested in the solutions at $z = 0$, which are shown in Fig. 3.5(a) for chosen values of α . We notice that as α tends to 1 the solution approaches zero, while as α approaches two the solution approaches the behavior of a stationary front. The algebraic expression of the family of solutions of Eq. (3.35) at $z = 0$ is

$$u_\alpha(x, 0) = 2 \{ \arctan(\gamma^{-1} \tan \delta x) - \arctan(\gamma \tan \delta x) \}, \quad \alpha \in (1, 2). \quad (3.40)$$

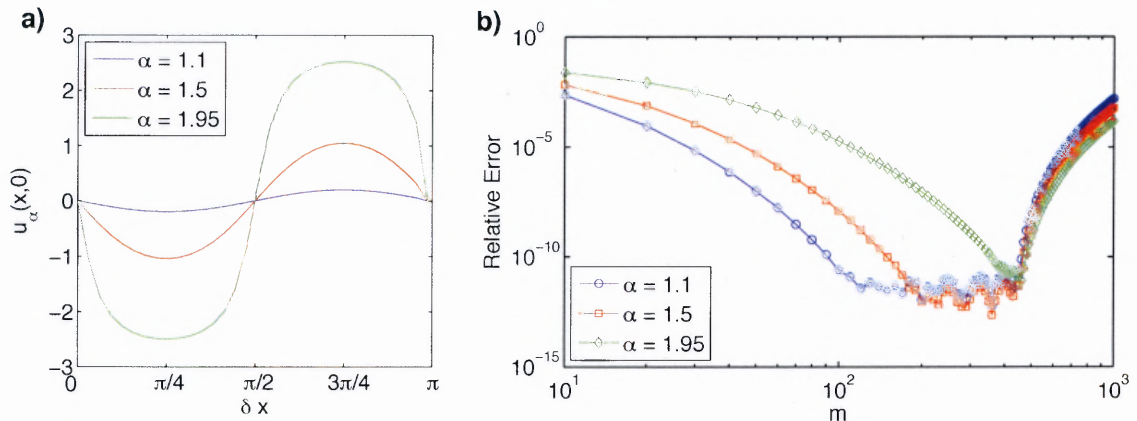


Figure 3.5 (a) The form of the solutions of (3.35) for several values of α . (b) Results of the convergence studies of the numerical solution using a compensated grid with $n = 14$ obtained in Sec. 3.2.

We solve this problem numerically by first discretizing the two dimensional domain $[0, \frac{\pi}{2\delta}] \times [0, +\infty)$ with a uniform grid of size m and stepsize h_\perp in the transversal (i.e. x) direction, and with a compensated optimal grid of size $n = 14$ in the vertical (z) direction. This compensated optimal grid is the same as the one obtained in the previous section and used for the simulations in Fig. 3.4. Therefore, for each simulation, the original compensated grid is rescaled through a multiplication by h_\perp , since the grid was obtained assuming a uniform unitary step along the transversal direction. At the extrema of the horizontal boundary, we used Dirichelet boundary conditions, which for this particular choice of boundaries are homogeneous.

To obtain the solution of the discrete problem, we use a relaxation approach, in which an appropriate initial condition is integrated in pseudo-time until a steady-state is reached. This equilibrium solution is the solution of the original time-independent problem (3.35). To do so, we replace the Laplacian with a diffusion operator, therefore adding a first order time derivative term that we discretize using forward finite differences with timestep Δt , thus obtaining a discrete version of problem (3.35),

namely

$$\frac{u_{j,k}^{t+\Delta t} - u_{j,k}^t}{\Delta t} = \frac{u_{j+1,k}^t - 2u_{j,k}^t + u_{j-1,k}^t}{h_{\perp}^2} + \frac{1}{h_k} \left(\frac{u_{j,k+1}^t - u_{j,k}^t}{h_{k+1/2}} - \frac{u_{j,k}^t - u_{j,k-1}^t}{h_{k-1/2}} \right), \quad (3.41)$$

$$\frac{u_{j,0}^{t+\Delta t} - u_{j,0}^t}{\Delta t} = \frac{u_{j+1,0}^t - 2u_{j,0}^t + u_{j-1,0}^t}{h_{\perp}^2} + \frac{1}{h_0} \left(\frac{u_{j,1}^t - u_{j,0}^t}{h_{1/2}} + \sin u_{j,0}^t \right). \quad (3.42)$$

We then analyzed the convergence properties of compensated optimal grids for the above problem as the size of the mesh in the transverse direction increases. These results are shown in Fig. 3.5 (b), where the L_{∞} norm of the relative error of the numerical solution is plotted as a function of m , for different values of α .

For these simulations, we observe exponential convergence, as was achieved for the linear case of the previous section. However, we also notice that as α approaches its upper bound, the range of values for which we achieve maximum accuracy decreases. For instance, in the case of $\alpha = 1.5$, by doubling the number of grid-points along x the error decreases by approximately one order of magnitude until it reaches its limit. After reaching this limit, further increase of m does not produce any benefit in terms of accuracy of the numerical solution. Moreover, once a certain critical value (independent of α) of m is reached, the accuracy begins to deteriorate since the given compensated optimal grid has not been defined to resolve these long-wave Fourier modes. However, for different values of α , we obtain an apparently different spectral interval of resolution. In particular, as α approaches 2, we observe a decrease in the range of values for which maximum accuracy is achieved. This result is due to the nature of the problem. In fact, as $\alpha \rightarrow 2$, the period of the solution tends to infinity, since in this limit $\delta \rightarrow 0$. As a result, there are more wavenumbers that need to be resolved simultaneously than for smaller values of α , and these extra wavenumbers cause the method to have a smaller range of maximum accuracy. Nonetheless, the method maintains its exponential rate of convergence as we see from the slope in Fig. 3.5.

To summarize these numerical studies, the method of compensated optimal grids applied to the considered nonlinear problem produces solutions that are essentially spectrally accurate. This is quite surprising for a finite-difference method based on a five-point stencil. Moreover, the method provides an easy way to control the error of the approximation, and allows us to obtain solutions with high accuracy using relatively small finite difference grids.

3.3.3 Extension to three-dimensional problems

The results obtained so far have shown the high accuracy and flexibility of compensated optimal grid approaches applied to two dimensional domains. Can we use the same approach to discretize problems in three dimensions? We can try, since all we have to do is discretize one direction using an optimal grid, but as we will show in this Section, we cannot achieve spectral accuracy using just compensation. However, by using a certain approach to discretize the transversal plane, we can achieve at least fourth order accuracy at essentially no extra computational cost. This result is impressive, since when working in three dimensions the required computational effort can be very expensive. To be able to reduce the computational load by reducing the number of gridpoints and also achieve fourth order accuracy is a big step forward with respect to more common methods such as finite differences, which only achieve 2nd order accuracy.

As before, we first consider a simple model problem, which in this case is a straightforward extension of boundary-value problem (3.31)

$$\frac{\partial^2 u}{\partial x^2} + \frac{\partial^2 u}{\partial y^2} + \frac{\partial^2 u}{\partial z^2} = 0 \quad \text{in } [0, L_x] \times [0, L_y] \times [0, \infty), \quad (3.43)$$

$$\frac{\partial u}{\partial z} \Big|_{z=0} = -\cos q_1 x \cos q_2 y, \quad \frac{\partial u}{\partial x} \Big|_{y=0, L_y} = 0, \quad \frac{\partial u}{\partial y} \Big|_{x=0, L_x} = 0, \quad (3.44)$$

where q_1 and q_2 are integer multiples of $\pi/L_{x,y}$, respectively.

Unfortunately, the straightforward extension of the method of Sec. 3.2 to (3.43) and (3.44), in which the three-point stencil in the transversal direction is replaced with a five-point centered difference for the transversal plane on a square grid with step h_{\perp} , would not work because of the numerical anisotropy introduced by such a discretization. In fact, under this approximation we have

$$\lambda_q = -\frac{2}{h_{\perp}^2} [\cos(q_1 h_{\perp}) + \cos(q_2 h_{\perp}) - 2], \quad (3.45)$$

and by Taylor expansion of the right hand side of Eq.(3.45) we find that

$$\lambda_q \approx |\mathbf{q}|^2 - \frac{1}{12} h_{\perp}^2 (q_1^4 + q_2^4) + O(h_{\perp}^4). \quad (3.46)$$

As a result, only the modes with either $q_1 = 0$ or $q_2 = 0$ (which essentially correspond to a one dimensional problem) would be spectrally resolved. In any other case, we cannot compensate as we did for the one dimensional case and the $O(h_{\perp}^2)$ error due to lack of anisotropy of this finite difference approximation will always be present.

We confirmed this observation by running the solver using various combinations of q_1 and q_2 . The results obtained are depicted in Fig. 3.6 and show that the one-dimensional compensated grid still performs no better than the geometric optimal grid of the same size except for the case $\mathbf{q} = (q_1, 0)$ or $\mathbf{q} = (0, q_2)$, which is essentially one dimensional. In particular, the methods all have second order convergence, as we would expect from the result in Eq. (3.46). To avoid this behavior, we need to discretize the transversal Laplacian using a more isotropic scheme. We will do so in the next two sections.

3.3.4 Compensation on hexagonal grids

Since the problem encountered in the previous simulations is due to the anisotropy of the five-point stencil, we can try to construct a more isotropic mesh. A natural way

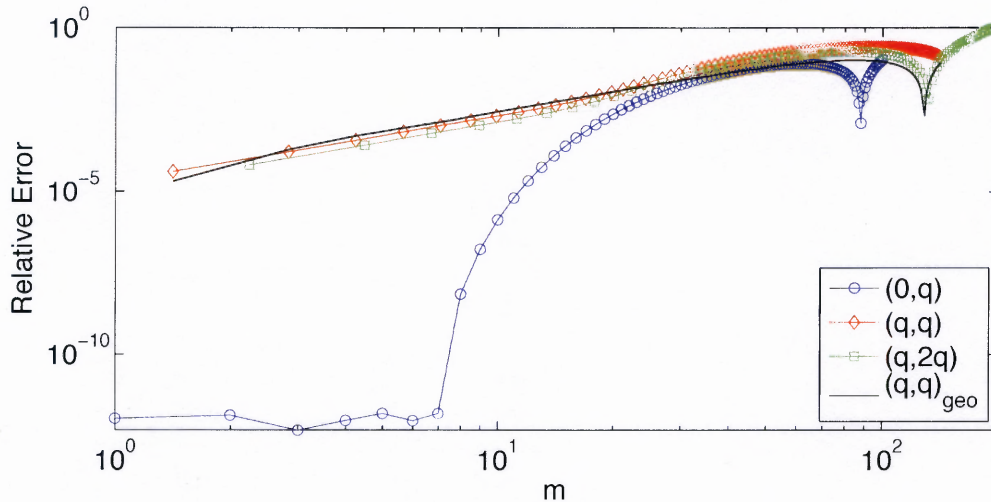


Figure 3.6 Convergence study for the solution of (3.43) with results for the compensated grids with $n = 14$ for various combinations of \mathbf{q} , together with the results for an optimal geometric grid of size $n = 14$ (continuous black line).

to do so would be to go from a square based grid to a hexagonal one, like the grid shown in Fig. 3.7 a.

We coupled this type of discretization of the plane with a seven-point discretization, thus obtaining the following numerical scheme:

$$\frac{2}{3h_{\perp}^2} \sum_{j' \in \mathcal{N}_j} (u_{j'}^k - u_j^k) + \frac{1}{h_k} \left(\frac{u_j^{k+1} - u_j^k}{h_{k+1/2}} - \frac{u_j^k - u_j^{k-1}}{h_{k-1/2}} \right) = 0, \quad k \geq 1, \quad (3.47)$$

$$\frac{2}{3h_{\perp}^2} \sum_{j' \in \mathcal{N}_j} (u_{j'}^0 - u_j^0) + \frac{1}{h_0} \left(\frac{u_j^1 - u_j^0}{h_{1/2}} + \cos q_1 x_j \cos q_2 y_j \right) = 0, \quad (3.48)$$

where the index j denotes a point on the hexagonal grid contained inside a rectangle on $[0, L_x] \times [0, L_y]$ and aligned with its sides (see Fig. 3.7 a), (x_j, y_j) denotes the Cartesian coordinates of the point with index j , and \mathcal{N}_j is the set of 6 nearest neighbors of the j -th point.

While the second term in each equation of scheme (3.47)-(3.48) is due to the optimal grid approximation, the first term represents the numerical scheme for the transversal Laplacian and can be obtained through, e.g. a finite volume approach. In

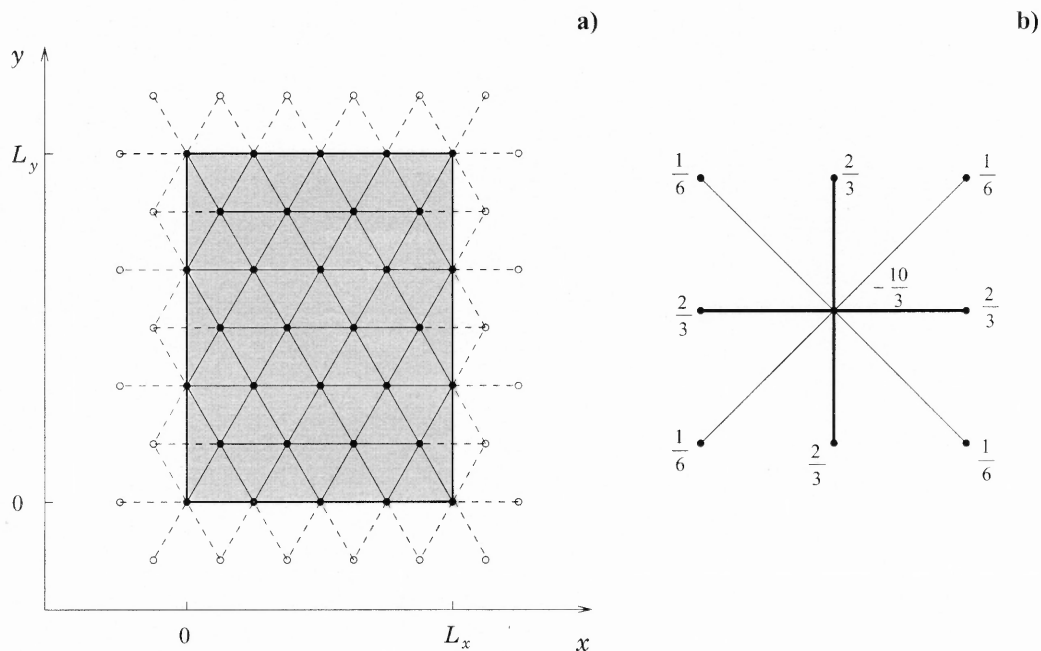


Figure 3.7 (a) The discretization of the rectangular domain using a hexagonal grid. (b) The 9-point anisotropy-adjusted stencil for Δ_{\perp} on a square grid. In (a), the solid circles show the discretization nodes, while the empty circles correspond to the ghost nodes of the reflecting boundary. Similarly, solid lines in (a) show the connections between the discretization nodes, while dashed lines show the connections to the ghost nodes. In (b), the fractions give, apart from the factor of h_{\perp}^{-2} , the weights of different nodes in the stencil.

fact, finite volumes represent a more general way to discretize the plane and can be efficiently extended to imperfect lattices [80] (see Chapter 6).

To complete the numerical setup of model problem (3.43), we add that we are using reflecting boundary conditions on the rectangle boundaries and a Dirichlet boundary condition at $k = n$.

To apply compensation to scheme (3.47), we need to determine the source of the error of the scheme itself. We put $u = e^{iq_1x+iq_2y}$, and then proceeding as in Section

3.2

$$\lambda_q u = -\frac{2}{3h_\perp^2} \sum_{j' \in \mathcal{N}_j} (u_{j'}^k - u_j^k), \quad (3.49)$$

$$\begin{aligned} \lambda_q e^{iq_1 x + iq_2 y} &= -\frac{2}{3h_\perp^2} \left(e^{iq_1(x+h_\perp)+iq_2 y} + e^{iq_1(x-h_\perp)+iq_2 y} + e^{iq_1(x-h_\perp/2)+iq_2(y+\sqrt{3}h_\perp/2)} + \right. \\ &\quad \left. + e^{iq_1(x-h_\perp/2)+iq_2(y-\sqrt{3}h_\perp/2)} + e^{iq_1(x+h_\perp/2)+iq_2(y+\sqrt{3}h_\perp/2)} + \right. \\ &\quad \left. e^{iq_1(x+h_\perp/2)+iq_2(y-\sqrt{3}h_\perp/2)} - 6e^{i(q_1 x + q_2 y)} \right), \end{aligned} \quad (3.50)$$

$$\begin{aligned} \lambda_q &= -\frac{2}{3h_\perp^2} \left(e^{iq_1 h_\perp} + e^{-iq_1 h_\perp} + e^{-iq_1 \frac{h_\perp}{2}} e^{iq_2 \frac{\sqrt{3}h_\perp}{2}} + \right. \\ &\quad \left. + e^{-iq_1 \frac{h_\perp}{2}} e^{-iq_2 \frac{\sqrt{3}h_\perp}{2}} + e^{iq_1 \frac{h_\perp}{2}} e^{iq_2 \frac{\sqrt{3}h_\perp}{2}} + e^{iq_1 \frac{h_\perp}{2}} e^{-iq_2 \frac{\sqrt{3}h_\perp}{2}} - 6 \right) \end{aligned} \quad (3.51)$$

$$= -\frac{2}{3h_\perp^2} \left\{ \cos(q_1 h_\perp) + 2 \cos\left(\frac{q_1 h_\perp}{2}\right) \cos\left(\frac{q_2 h_\perp \sqrt{3}}{2}\right) - 3 \right\}. \quad (3.52)$$

From this result, we have:

$$\lambda_q = |\mathbf{q}|^2 - \frac{1}{16} h_\perp^2 |\mathbf{q}|^4 + O(h_\perp^4). \quad (3.53)$$

The first two terms of Eq. (3.53) only depend on the modulus of the eigenvalues, and only the fourth order term depends explicitly on the components of \mathbf{q} . This fact is of extreme importance, since it will determine the accuracy that we should expect from the compensated approach.

From the results in Eq. (3.52), we can find an analogue of Eq. (3.24) for the hexagonal scheme

$$\begin{aligned} u(x_j, y_j, 0) &\approx \cos q_1 x_j \cos q_2 y_j \\ &\times F_n \left[\frac{4}{3h_\perp^2} \left\{ 3 - \cos(q_1 h_\perp) - 2 \cos\left(\frac{q_1 h_\perp}{2}\right) \cos\left(\frac{q_2 h_\perp \sqrt{3}}{2}\right) \right\} \right], \end{aligned} \quad (3.54)$$

where F_n is the impedance function of the grid in the z -direction.

The idea of compensation is now to modify the impedance function F that is being approximated by some F_c to cancel out the leading order error term in (3.53).

This is the best that we can do in three dimensions with this choice of stencil, since the dependence of the fourth order term on both components q_1 and q_2 does not allow (in this context) to compensate for the error in both directions at the same time. However, since the second order term depends only on the modulus $|\mathbf{q}|$, by choosing a particular direction of compensation we are able to eliminate the second order error, and also obtain essentially spectral accuracy along this preferred direction. This can be achieved, for example, by matching the resulting impedance function to the exact impedance function for $q_1 = 0$. Thus, we arrive at

$$F_c(\lambda) = \frac{h_\perp \sqrt{3}}{2 \arccos\left(1 - \frac{3}{8} h_\perp^2 \lambda\right)}. \quad (3.55)$$

With this choice of F_c , we have

$$F_c \left[\frac{4}{3h_\perp^2} \left\{ 3 - \cos(q_1 h_\perp) - 2 \cos\left(\frac{q_1 h_\perp}{2}\right) \cos\left(\frac{q_2 h_\perp \sqrt{3}}{2}\right) \right\} \right] = F(|\mathbf{q}|) + O(h_\perp^4), \quad (3.56)$$

for all choices of \mathbf{q} , with the error term vanishing identically for all $\mathbf{q} = (0, q)$.

Finally, constructing an optimal grid from the rational approximant F_n of the modified impedance function F_c on the spectral interval $\lambda \in [\lambda_{\min}, \lambda_{\max}]$, with $\lambda_{\min} = O(1)$ and $\lambda_{\max} = O(h_\perp^{-2})$, we resolve the solution at $z = 0$ with $O(h_\perp^4)$ accuracy, provided the value of n is chosen to be sufficiently large. While the obtained accuracy is no longer spectral-like, as in the case of one-dimensional problems, it nevertheless is of higher order than the expected second-order accuracy of such a 7-point centered difference stencil in three dimensions.

We performed numerical tests of the proposed method by solving the discretized version of the problem (3.43) and (3.44) with the help of the diagonally preconditioned conjugate gradient method, choosing $L_x = \pi$ and $L_y = \frac{115}{200} \pi \sqrt{3}$ with $h_\perp = \frac{\pi}{200}$.

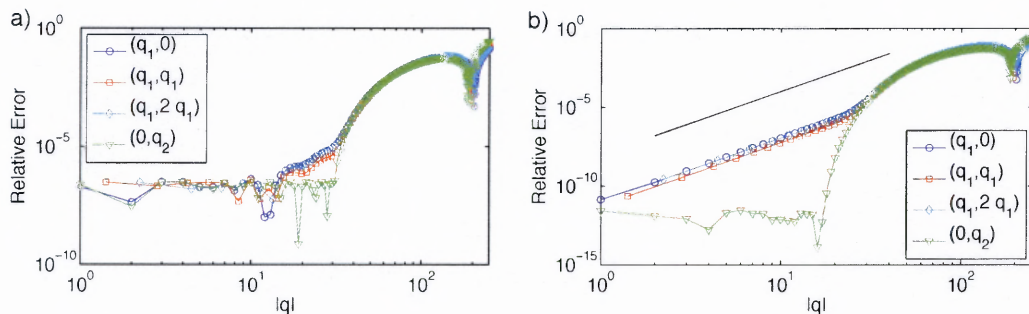


Figure 3.8 The L^∞ norm of the relative error of the numerical solution of (3.43) and (3.44) obtained, using hexagonal grids in the xy -plane and compensated optimal grids with $n = 8$ in (a) and $n = 14$ in (b) (see text for complete details). In (b), the straight line indicates the $O(|\mathbf{q}|^4)$ dependence.

We used two different optimal rational approximants for F_c in (3.55): one with $n = 8$ optimized on the spectral interval $\lambda \in [1, 10^3]$, and the other with $n = 14$ optimized on the spectral interval $\lambda \in [3 \times 10^{-1}, 3 \times 10^2]$.

The results for several choices of \mathbf{q} are shown in Fig. 3.8. One can see that, as $|\mathbf{q}|$ is decreased, the accuracy of the solution quickly reaches the resolution limit of 3.2×10^{-7} for the $n = 8$ optimal grid, and stays low for all smaller wave vectors in the problem. The performance of these grids is essentially as good as that of the one-dimensional compensated optimal grid constructed earlier (see Sec. 3.2). On the other hand, in the case of the $n = 14$ optimal grid the error reaches the resolution limit of 1.6×10^{-12} only for the wave vector $(0, q)$, as we should expect from our choice of compensation. Nevertheless, we are still able to obtain an error that behaves as $O(|\mathbf{q}|^4)$ for all the other wave vectors.

3.3.5 Compensation on anisotropy-adjusted square grids

We can also use a finite-difference approach for uniform square grids to obtain results similar to the ones in Section 3.3.4 for hexagonal grids.

In this case, to reduce the anisotropy we discretize the problem in the xy -plane to achieve a higher degree of isotropy for the discrete problem. Note that this

is different than using higher-order discretization for spatial derivatives, since the resulting stencil may still remain $O(h_{\perp}^2)$ accurate.

For instance, let us try to solve numerically the boundary-value problem given by (3.43) and (3.44) using a square grid based finite difference approach for the transverse Laplacian and compensated optimal grid in the vertical direction.

We have previously observed that the most obvious choice of a 5-point centered difference stencil is not sufficient to overcome the anisotropy that it produces (the second order term in Eq. (3.46)), thus leading to second order accuracy (see Fig. 3.6).

Instead, we consider the centered 9-point stencil involving nearest and next-to-nearest neighbors of each grid point (see Fig. 3.7(b)). In particular, because of the symmetry of the grid, we obtain the weights of part (b) in Fig. 3.7, e.g. the neighboring points have all the same weight which is different from the weight of the next to neighboring points. To see this, let us denote by i and j the Cartesian indices of the points on the square grid in the xy -plane and by k the index of the staggered grid in the z -direction, we write:

$$\begin{aligned} \Delta_{\perp} u^k(x_i, y_j) &= \frac{a}{h_{\perp}^2} (u_{i+1,j}^k + u_{i-1,j}^k + u_{i,j+1}^k + u_{i,j-1}^k) + \\ &+ \frac{b}{h_{\perp}^2} (u_{i+1,j+1}^k + u_{i+1,j-1}^k + u_{i-1,j+1}^k + u_{i-1,j-1}^k) + \frac{c}{h_{\perp}^2} u_{i,j}^k, \end{aligned} \quad (3.57)$$

where $x_i = ih_{\perp}$ and $y_j = jh_{\perp}$, and a , b and c are weights that need to be determined.

If we now assume that $u = e^{iq_1 x_i + iq_2 y_j}$, we obtain the following expression for λ_q :

$$\lambda_q = - \left\{ \frac{2a}{h_{\perp}^2} [\cos(q_1 h_{\perp}) + \cos(q_2 h_{\perp})] + \frac{4b}{h_{\perp}^2} \cos(q_1 h_{\perp}) \cos(q_2 h_{\perp}) + \frac{c}{h_{\perp}^2} \right\}, \quad (3.58)$$

if we now Taylor expand the above expression

$$\begin{aligned}
\lambda_q &= -\frac{1}{h_\perp^2} \left\{ 2a \left[1 - \frac{q_1^2 h_\perp^2}{2} + \frac{q_1^4 h_\perp^4}{4!} + 1 - \frac{q_2^2 h_\perp^2}{2} + \frac{q_2^4 h_\perp^4}{4!} \right] \right. \\
&+ 4b \left[1 - \frac{q_1^2 h_\perp^2}{2} - \frac{q_2^2 h_\perp^2}{2} + \frac{q_1^4 h_\perp^4}{4!} + \frac{q_2^4 h_\perp^4}{4!} + \frac{q_1^2 q_2^2 h_\perp^4}{4} \right] \\
&+ \left. c + O(h_\perp^6) \right\}, \tag{3.59}
\end{aligned}$$

and match corresponding powers of h_\perp , we obtain that for the choice of $a = 2/3$, $b = 1/6$, and $c = -10/3$

$$\lambda_q = |\mathbf{q}|^2 - \frac{1}{12} h_\perp^2 |\mathbf{q}|^4 + O(h_\perp^4), \tag{3.60}$$

which is analogous to (3.53). We should also mention that this stencil has been mentioned in [69] in a different context.

Hence, using the discretization of (3.57) in place of the 7-point stencil in a suitably modified version of (3.47) and (3.48), we find the solution to be

$$\begin{aligned}
u(x_i, y_j, 0) &\approx \cos q_1 x_i \cos q_2 y_j \\
&\times F_n \left[\frac{2}{3h_\perp^2} \{ 5 - 2 \cos(q_2 h_\perp) - \cos(q_1 h_\perp) (\cos(q_2 h_\perp) + 2) \} \right], \tag{3.61}
\end{aligned}$$

where, again, F_n is the impedance function of the staggered grid along the vertical Laplacian. When $q_2 = 0$, the solution in (3.61) reduces to

$$u(x_i, y_j, 0) \approx F_n[2h_\perp^{-2}(1 - \cos q_1 h_\perp)] \cos q_1 x_i, \tag{3.62}$$

which coincides with the result in Eq. (3.25) obtained for the one-dimensional problem. Therefore, approximating by F_n the impedance function F_c from (3.27), we have $u(x_i, y_j, 0) \approx F(q_1^2) \cos q_1 x_i$, and, moreover, for all \mathbf{q}

$$u(x_i, y_j, 0) \approx F(|\mathbf{q}|) \cos q_1 x_i \cos q_2 y_j + O(h_\perp^4). \tag{3.63}$$

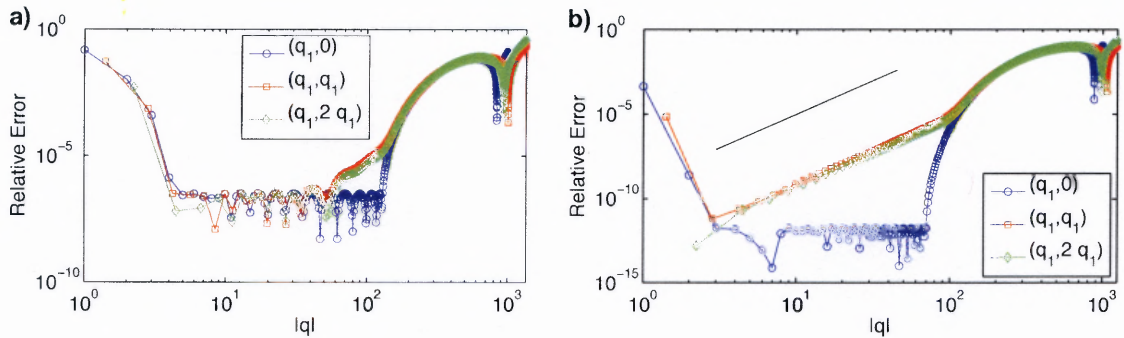


Figure 3.9 The L^∞ norm of the relative error of the numerical solution of (3.43) and (3.44) obtained, using anisotropy-adjusted square grids in the xy -plane and compensated optimal grids with $n = 8$ in (a) and $n = 14$ in (b) (see text for complete details). In (b), the straight line indicates the $O(|\mathbf{q}|^4)$ dependence.

In other words, we obtain a result similar to that for hexagonal lattices with the 7-point stencil, i.e., the solution of the discrete problem is approximating the exact solution of the boundary-value problem as well as the rational function F_n approximates the modified impedance function F_c given by (3.27), and the solution is $O(h_\perp^4)$ accurate for all wave vectors at sufficiently large values of n . We note that the compensated optimal grid in this case coincides with the one already constructed for the two-dimensional problem in Sec. 3.2.

Results of numerical studies analogous to those of Sec. 3.3.4 are presented in Fig. 3.9. In (3.43) and (3.44) we choose $L_x = L_y = \pi$ and discretize the problem with $h_\perp = \frac{\pi}{1000}$, using the compensated optimal grids constructed earlier in Sec. 3.3.1 with $n = 8$ and $n = 14$. The obtained results coincide with those obtained using the method of Sec. 3.3.4.

To summarize, we have shown that for the exterior Laplace problem in half-space, we can increase the accuracy of the optimal grid method from second order to fourth order by changing the impedance function being approximated so that it matches closely the scheme used to discretize the transverse Laplacian. Now, let us demonstrate the utility of this method when applied to a cell signaling problem.

3.4 Application to Cell Signaling

We now combine the discussion in the preceding sections with the mathematical modeling introduced in Chapter 2 to study a model problem arising in epithelial cell signaling.

In particular, we consider an idealized framework consisting of a flat epithelial layer and a semi-infinite layer of extracellular medium as in Fig. 2.1. Cells at the bottom of the layer emit various signaling molecules which can then diffuse in the extracellular space and bind to their specific cell-surface receptors [64, 28]. Binding of the signaling molecule to its respective receptor, in turn, activates the intracellular signaling cascades which then elicit multiple cellular responses. Importantly, such responses may further regulate secretion of the acting signaling molecule, resulting in the establishment of positive and negative feedbacks [29].

For simplicity we consider only one ligand molecule of concentration $s(t, x, y, z)$. From the mechanistic model described in Chapter 2 by Eqs. (2.4)-(2.8), we know that s satisfies the diffusion equation with an inhomogeneous Neumann boundary condition at $z = 0$ (the level of the epithelial layer) [62, 53]:

$$s_t = D_s \Delta s, \quad -D_s s_z|_{z=0} = g_s(t, x, y, z, s(t, x, y, 0)), \quad (3.64)$$

where Δ denotes the three dimensional Laplacian, and g_s is the secretion rate at which the ligand is secreted from the unit area of the epithelium surface. In general the argument of g_s will depend (explicitly or implicitly) on the ligand concentration s , so that a feedback loop can be established, but it can also depend on many other extracellular and intracellular elements. For example, in Chapter 2 we obtained this feedback by coupling ligand dynamics with the intracellular processes that are activated by ligand-receptor complexes on the epithelium (see the role of p in Eq. (2.6)).

We determine the form of g_s by assuming a Hill function behavior for the secretion rate of the ligand (σ in Eq. (2.6)), where the argument of this sigmoidal function is proportional to the concentration of ligand-receptor complexes (s^*). We also assume fast ligand-receptor kinetics, which is a biophysically reasonable approximation [62, 53] that becomes exact for stationary solutions, and an excess of ligand-sensing receptors.

Under the above conditions, and using the same notation as for the model described by Eqs. (2.4-2.8), we find the following expression for g_s as a function of the parameters of the system and the Dirichlet data $s(t, x, y, 0) = \bar{s}$:

$$g_s = -\frac{k_{s,ec}k_{s,on}r_s\bar{s}}{k_{s,off} + k_{s,ec}} + \frac{\bar{g}_s\bar{s}^\nu}{s_0^\nu + \bar{s}^\nu}, \quad (3.65)$$

where \bar{g}_s is the minimum secretion rate, and s_0 is an appropriately rescaled threshold of s_0^* .

To the dynamics described by Eqs. (3.64) and (3.65) we add another mechanism that is responsible for generating a feedback loop, which consists of an imposed morphogen gradient that contributes to the ligand-induced ligand-release dynamics. This is one of the roles that morphogens have in development [64].

To determine a form of g_s that models the involvement of both mechanisms in the feedback loop formation, we assume that a particular cell on the epithelial layer is emitting a morphogen molecule at the rate of Q_w molecules in a unit of time, that the morphogen recapture rate from the layer cells is negligible, and that the size of the cell is small with respect to the length scale of the problem. Under these assumptions, the concentration w of the morphogen molecule satisfies the following diffusive partial differential equation

$$w_t = D_w\Delta w \quad \text{for } z > 0, \quad -D_w w_z = Q_w\delta(x)\delta(y) \quad \text{at } z = 0, \quad (3.66)$$

where we placed the emitting cell at the origin. Here, $\delta(x)$ denotes the Dirac delta-function, and D_w is the diffusion constant of the morphogen.

We also suppose that the morphogen molecule can reversibly bind to its own receptor to form a morphogen-receptor complex (whose concentration we indicate with w^*), and that this complex is required to activate signaling through the positive feedback loop. Under the same regimes of fast equilibration kinetics together with excess of morphogen-sensing receptors, we may conclude that the density of morphogen-receptor complexes w^* is proportional to morphogen concentration at the cell surface with the constant of proportionality given by the ratio between the rates of complex formation and complex dissociation

$$w^* = \frac{k_{w,\text{on}}r_w}{k_{w,\text{off}}}w \quad \text{at } z = 0, \quad (3.67)$$

where $k_{w,\text{on}}r_w$ is the morphogen-receptor binding rate times the number of receptors per unit area and $k_{w,\text{off}}$ is the morphogen-receptor dissociation constant.

It is also biophysically reasonable to assume that ligand release depends on the product of concentrations of the inductive signal (the morphogen) and the induced ligand. This algebraic expression can be viewed as an approximation of the AND logic commonly encountered in developmental gene regulatory networks [15]. With this in mind, the input to the signaling cascade in the secretion rate (the argument of the Hill function in (3.65)) should now be taken to be proportional to the cell surface density of ligand-receptor and morphogen-receptor complexes:

$$g_s = -\frac{k_{s,\text{ec}}k_{s,\text{on}}r_s\bar{s}}{k_{s,\text{off}} + k_{s,\text{ec}}} + \frac{\bar{g}_s c^\nu}{c_0^\nu + c^\nu}, \quad c = \alpha_{sw} s^* w^*, \quad (3.68)$$

where, as before, we have assumed fast equilibration of the binding kinetics.

We are particularly interested in the steady state solution of this configuration. For the morphogen concentration w , we can find the stationary solution analytically

by using the Green's function for the Laplacian, obtaining:

$$w(x, y, 0) = \frac{Q_w}{2\pi D_w \sqrt{x^2 + y^2}}. \quad (3.69)$$

Before we apply this result to Eq. (3.64), it is also convenient to rescale the problem by introducing the nondimensional quantities

$$\begin{aligned} u &= \frac{k_{s,\text{on}} k_{s,\text{ec}} r_s}{\bar{g}_s (k_{s,\text{off}} + k_{s,\text{ec}})} s, \\ \kappa &= \frac{2\pi D_w D_s k_{w,\text{off}} (k_{s,\text{off}} + k_{s,\text{ec}}) c_0}{\alpha_{sw} \bar{g}_s Q_w k_{w,\text{on}} k_{s,\text{on}} r_s r_w}, \\ L &= \frac{D_s (k_{s,\text{off}} + k_{s,\text{ec}})}{k_{s,\text{ec}} k_{s,\text{on}} r_s}. \end{aligned} \quad (3.70)$$

Finally, we obtain the following equation describing ligand's stationary signaling profiles:

$$\Delta u = 0, \quad z > 0, \quad u_z = \bar{u} - \frac{\bar{u}^\nu}{\kappa^\nu (x^2 + y^2)^{\nu/2} + \bar{u}^\nu} = 0, \quad z = 0. \quad (3.71)$$

We have simulated the problem in Eq. (3.71) with $\nu = 2$ and $\kappa = 0.15$ on a square $(x, y) \in [-L, L] \times [-L, L]$ with Dirichlet boundary conditions.

In practice, the problem was solved using an explicit relaxation algorithm on a hexagonal grid covering the first quadrant with Neumann boundary conditions at $x = 0$ or $y = 0$, and Dirichlet boundary conditions at $x = L_x$ or $y = L_y$, with L_x, L_y chosen sufficiently close to $L = 15$ in a way compatible with the lattice. We used the suitably rescaled $n = 14$ compensated optimal grid obtained in Sec. 3.3.3 and varied h_\perp in the range $h_\perp = 0.1 \div 1$.

The profile of the solution for $h_\perp = 0.25$ is shown in Fig. 3.10(a). It has the expected bell-shaped profile, with high signaling restricted to a small neighborhood of the cell emitting the morphogen. Also, quite expectedly, we found that the region of high signaling grows upon decrease of κ (corresponding to increase in Q_w), and

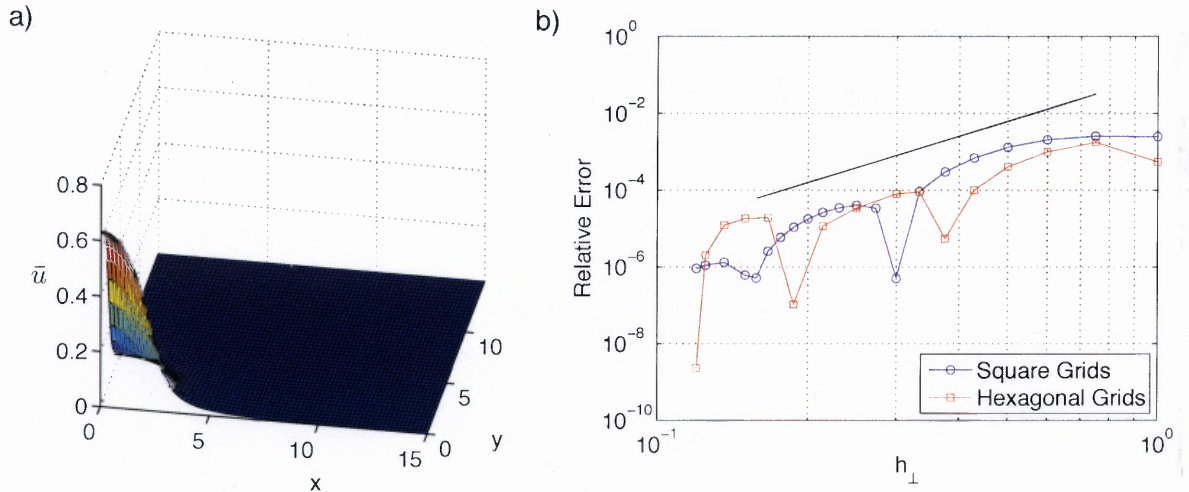


Figure 3.10 (a) The profile of the solution of (3.71) obtained using the $n = 14$ compensated optimal grid of Sec. 3.3.3 on a hexagonal lattice with $h_{\perp} = 0.25$, $L_x = 60h_{\perp}$, $L_y = 68h_{\perp}\sqrt{3}/2$. (b) The relative error of $\bar{u}(0,0)$ obtained using the $n = 14$ compensated optimal grids of Sec. 3.3.3 for hexagonal and anisotropy-adjusted square lattices. In (b), the straight line indicates the $O(h_{\perp}^4)$ dependence.

shrinks with increase of κ , until at some critical value of κ the solution disappears altogether. This signifies a region of bistability, since the problem always has $\bar{u} = 0$ as the trivial solution.

We have also performed convergence studies of the solution to assess the accuracy and efficiency of the method. As the indicator, we chose the maximum value of \bar{u} in the computational domain, which is attained at the origin. The results of these studies for both the hexagonal and anisotropy-adjusted square lattices combined with their corresponding $n = 14$ compensated optimal grids obtained in Sec. 3.3.3 are presented in Fig. 3.10(b). As expected, both lattices produce solutions that are fourth-order accurate in h_{\perp} .

3.5 Some Theoretical Considerations

So far, we have shown that it is possible to extend the method of optimal grids in such a way that the numerical error due to the discretization along the non opti-

mal direction(s) is either eliminated (for two dimensional problems) or significantly reduced (three dimensions). We also showed a successful application of the compensated optimal grids to cell signaling problems.

We would like to end the treatment of this subject by briefly comparing the compensated optimal grids method with Fast Fourier Transform (FFT) methods [82]. Thus far we only applied the compensated optimal grids method to problems that can already be solved using Fast Fourier Transform (FFT) methods.

Compensated optimal grids are very easy to use and implement (e.g. they can be easily embedded into existing codes) and straightforward to parallelize. Optimal grids can be used efficiently when implementing Newton-like methods for nonlinear problems, since they lead to sparse matrices to be inverted. This could be done for FFT too, but it would require the inversion of a non-sparse matrix. This task is computationally expensive for a two dimensional problem and could even be impossible in three dimensions where the matrix to be inverted would be of $O(N^4)$, where N is the number of grid points in one direction (e.g. $m = N^2$). Also, sometimes we have to use irregular grids to solve certain type of problems, e.g. when localized sources are present. This can be done using optimal grids, but not with FFT.

CHAPTER 4

AUTOCRINE SIGNAL TRANSMISSION IN THE PRESENCE OF VOLUME DEGRADATION

In this chapter, we are going to study the existence and qualitative properties of traveling fronts as mean of long range signal transmission in the presence of degradation in the bulk, i.e. in the context in which a ligand molecule diffusing away from the cell layer loses its signaling properties. This can happen through various mechanisms, such as sequestration by other molecules that are present in the extracellular matrix [63]. In a non developmental context, molecule degradation by extracellular ATP has been shown to enhance cell signaling in wound healing of corneal epithelial cells [92]. We begin by detailing the equations of the model for a general configuration of linear degradation.

4.1 Mathematical Model with Degradation

We are going to consider the general model consisting of Eqs. (2.4-2.8). This system is a mathematical representation of an idealized epithelium in which a cell layers sits at the boundary of a semi-infinite extracellular medium as shown in Fig. 2.1. We alter this model by adding a degradation term to the equation governing ligand diffusion (Eq. (2.4)). In particular, we assume that the rate of change of ligand concentration S is proportional to ligand concentration itself, and we indicate with k_{deg} the constant of proportionality.

We also consider the biophysically plausible assumption of fast binding kinetics that eliminate the first order time derivative in the complex evolution equation (Eq. (2.5)), and the assumption of receptors abundance, i.e. as ligands bind, unbind and ligand receptor complexes get internalized, the number of available receptors on the cell layer does not change significantly.

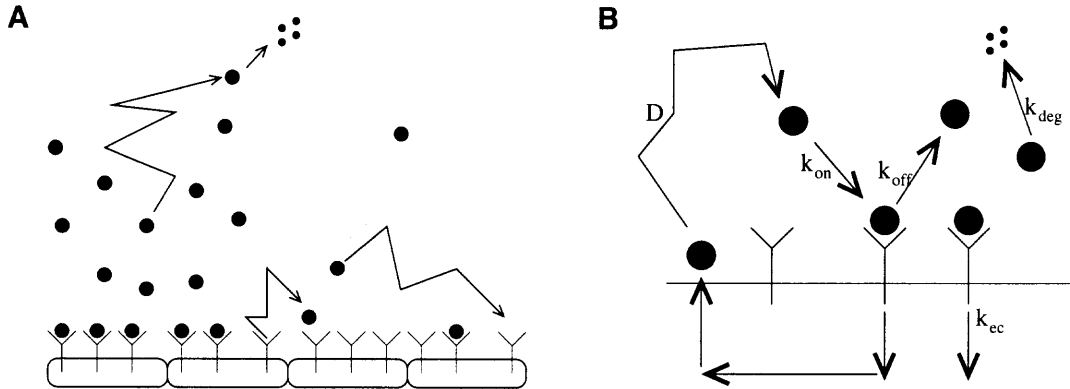


Figure 4.1 Ligand-mediated signal transmission. (A) The geometry of the system modeled by Eq. (4.1). (B) Illustration of elementary processes.

This system is represented graphically in Fig. 4.1, and these are its governing equations:

$$\frac{\partial S}{\partial T} = D \left(\frac{\partial^2 S}{\partial X^2} + \frac{\partial^2 S}{\partial Y^2} + \frac{\partial^2 S}{\partial Z^2} \right) - k_{deg} S, \quad Z > 0,$$

$$\left(D \frac{\partial S}{\partial Z} - k_{on} R S \right) \Big|_{Z=0} = -k_{off} C - g_S P, \quad (4.1)$$

$$0 = -(k_{off} + k_{ec}) C + k_{on} R \bar{S}, \quad \bar{S} = S|_{Z=0},$$

$$\frac{\partial P}{\partial T} = -k_P P + g_P \sigma(C/C_0).$$

In writing the last equation we assumed that the response to signaling is characterized by the sigmoidal function $g_P \sigma(C/C_0)$ taken to be a Hill function of order n

$$\sigma(x) = \frac{x^n}{1 + x^n}. \quad (4.2)$$

Our first step is to reduce the number of parameters by making the system dimensionless. We introduce these new variables:

$$t = k_p T; \quad x = \frac{X}{L}; \quad z = \frac{Z}{L}; \quad y = \frac{Y}{L}; \quad L = \frac{D(k_{off} + k_{ec})}{k_{ec} k_{on} R}; \quad (4.3)$$

$$s = \frac{k_P k_{ec} k_{on} R}{(k_{off} + k_{ec}) g_S g_P} S; \quad c = \frac{k_{ec} k_P}{g_S g_P} C; \quad p = \frac{k_P}{g_P} P. \quad (4.4)$$

The use of these new variables reduces the number of parameters from 10 to just 3, leading to the following system of equations:

$$\alpha \frac{\partial s}{\partial t} = \frac{\partial^2 s}{\partial x^2} + \frac{\partial^2 s}{\partial y^2} + \frac{\partial^2 s}{\partial z^2} - \gamma s, \quad z > 0, \quad (4.5)$$

$$\frac{\partial p}{\partial t} = -p + \sigma(c/c_0), \quad (4.6)$$

$$c = s|_{z=0}, \quad \left(\frac{\partial s}{\partial z} - s \right) \Big|_{z=0} = -p, \quad (4.7)$$

where:

$$\alpha = \frac{D k_P (k_{off} + k_{ec})^2}{k_{ec}^2 R^2 k_{on}^2}, \quad \gamma = \frac{k_{deg} D (k_{off} + k_{ec})^2}{k_{ec}^2 R^2 k_{on}^2}, \quad c_0 = \frac{k_{ec} k_P}{g_S g_P} C_0. \quad (4.8)$$

This is the model we are going to analyze in this Chapter. As first step, we will look at the model comparison with a well studied one [62, 61, 53] that presents many of the characteristics of the model under consideration.

4.2 Comparison with the Thin-Gap Limit

The most natural representation of the epithelium is a finite one, of course. And only under certain assumptions it is reasonable to consider a semi-infinite system like the one represented in Eq. (4.1).

In Chapter 2, we derived a simpler model (Eq. (2.17)) for an idealized epithelium in which ligand molecules are diffusing through a narrow layer of height H above the epithelium. The model we derived is two-dimensional, while the one that we consider here, like the one considered in [62, 61, 53] is three dimensional, and is obtained from the general one in the same way as we obtained Eq. (2.17)

$$\tau_s \frac{\partial s}{\partial t} = \frac{\partial^2 s}{\partial x^2} + \frac{\partial^2 s}{\partial y^2} - s + p, \quad \frac{\partial p}{\partial t} = -p + \sigma(s/c_0), \quad (4.9)$$

as long as $H \ll D/(Rk_{on})$ and $H \ll \sqrt{D/k_{deg}}$, with

$$\tau_s = \frac{k_P H (k_{off} + k_{ec})}{k_{ec} (k_{on} R + H k_{deg})}. \quad (4.10)$$

One of the main features that connects the above model with the one in Eqs. (4.5-4.7) is the feature of bistability. In fact, in both systems, there is a connection between the linear ligand diffusion with the nonlinear ligand production, this nonlinearity is the cause of potential steady state multiplicity. Furthermore, since σ , the nonlinear term responsible for protease activation and therefore ligand production, has sigmoidal shape, it can be shown that these systems can have two stable steady states [41, 55, 48].

In particular, for $\tau_s \gg 1$, Eq. (4.9) reduces to

$$\tau_s \frac{\partial s}{\partial t} = \frac{\partial^2 s}{\partial x^2} + \frac{\partial^2 s}{\partial y^2} - s + \sigma(s/c_0), \quad (4.11)$$

this equation has been extremely well-studied [24, 25, 26, 27, 41, 4, 67, 68, 51], and it is known that the system governed by Eq. (4.11) can be switched to the “on” state by a localized perturbation only if the threshold c_0 is sufficiently small so that the equation can be bistable [41]. The critical value of the threshold at which bistability can be observed in the spatially-distributed system is related to the existence of a stationary one-dimensional heteroclinic orbit connecting the two stable equilibria $s = \bar{s}_1 = 0$ and $s = \bar{s}_3$. This scenario is depicted in Fig. 4.2, where \bar{s}_3 is the largest of the two positive roots $\bar{s}_{2,3}$ of the nonlinearity in Eq. (4.11), i.e.

$$\bar{s}_{2,3} - \sigma(\bar{s}_{2,3}/c_0) = 0, \quad \bar{s}_3 > \bar{s}_2 > 0. \quad (4.12)$$

For planar fronts, this solution satisfies

$$\frac{d^2 s}{dx^2} - s + \sigma(s/c_0) = 0, \quad s(-\infty) = \bar{s}_3, \quad s(+\infty) = 0, \quad (4.13)$$

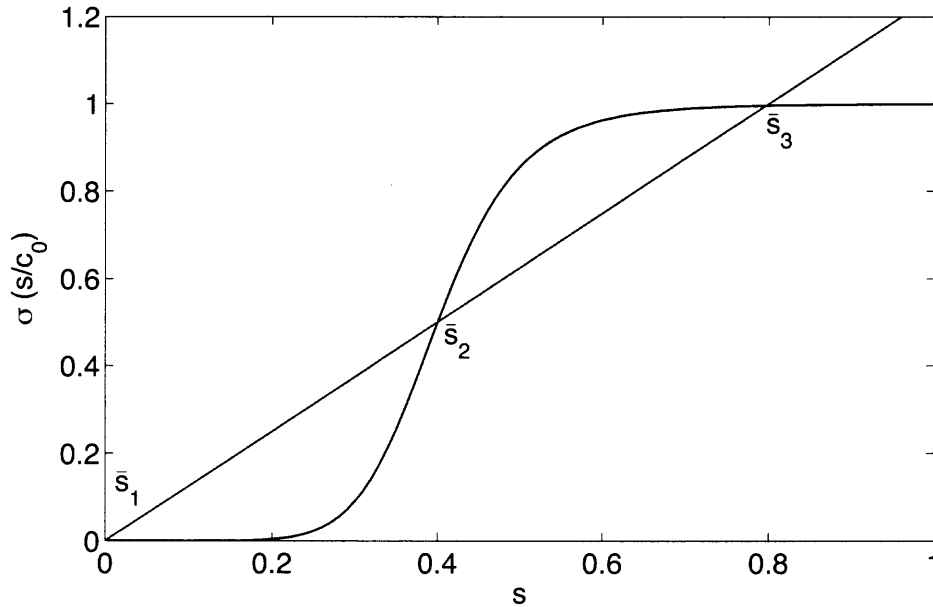


Figure 4.2 Graphical representation of a bi-stability scenario for Eq. (4.11)

and by multiplying this equation by s_x and then integrating, we can find a solvability condition ([41]) that is necessary and sufficient for the front existence:

$$E(\bar{s}_3) = 0, \quad E(\bar{s}) = \int_0^{\bar{s}} (s - \sigma(s/c_0)) ds. \quad (4.14)$$

This is the solvability condition for the boundary-value problem in Eq. (4.13) which determines the critical value of the threshold c_0 . Below this threshold, the positive feedback loop can be switched on in a spatially distributed system.

Thus, in the case of Eq. (4.11) and, in fact, the system of Eqs. (4.9) as well, one can characterize the spatial behavior of the autocrine loop by solving an algebraic problem in Eqs. (4.12) and (4.14). For instance, if we consider Eq. (2.30), which is the same as Eq. (4.11), with $\sigma(s/c_0) = \theta(s - c_0)$, where θ is the Heaviside step centered at c_0 . Then, Eq. (4.12) becomes

$$\bar{s} - \theta(\bar{s} - c_0) = 0 \quad \Leftrightarrow \quad \bar{s}_2 = c_0, \quad \bar{s}_3 = 1, \quad (4.15)$$

while Eq. (4.13), using the continuity of s , becomes

$$E(\bar{s}_3) = \int_0^1 s - \theta(s - c_0) ds = \int_{c_0}^1 s - 1 ds + \int_0^{c_0} s ds = c_0 - \frac{1}{2}, \quad (4.16)$$

and $E(\bar{s}_3)$ is equal to zero only if $c_0 = 1/2$, and the traveling front exists with $v > 0$ if and only if $c_0 < 1/2$. A well known result for a Heaviside nonlinearity that we used in Chapter 2 too.

In contrast, in the case of Eqs. (4.5) – (4.7) it is no longer obvious how to do this because of the non-local character of this problem. In the following, we will present a mathematical treatment which allows to obtain the criteria for activation of the positive feedback for the problem under consideration.

4.3 Steady State Multiplicity

We begin with the analysis of the steady states of signaling admitted by the model described by Eqs. (4.5-4.7). This is a necessary first step to check if traveling waves solutions connecting two stable steady states are possible.

For Eq. (4.11), the cooperativity due to ligand-mediated ligand release is enough to generate multiple steady states. In fact, the balance between a linear and a sigmoidal function that is required at equilibrium, coupled with a lower value of c_0 , implies the existence of three steady states (two stable and one unstable). This configuration is the one of the classical mathematical problem often referred in the literature as bistable equation [41, 22].

However, for model (4.5-4.7), the multiplicity of steady states is not a trivial result, although intuitively it is what we expect for certain values of the parameters of the problem. In fact, the bistable problem that we have obtained in the thin gap limit approximation is due to the possibility of averaging the concentration of the ligand along the z direction. This approximation localizes the dynamics of ligand-mediated ligand release to the epithelium layer, leading to steady states governed by

Eq. (4.12). In the half-space set up with degradation in the bulk, we cannot average along z anymore. Therefore, the equilibrium will depend not only on the dynamics at cell layer level, but also on the degradation in the bulk. And we need to study the balancing between these two phenomena to determine the steady states of the signaling system.

We are looking for the steady states of the non-dimensional model (4.5-4.7), i.e. solutions independent of time and the x, y coordinates. Therefore, at equilibrium the concentration of ligand in the bulk satisfies

$$\frac{\partial^2 s}{\partial z^2} = \gamma s, \quad s(0) = \bar{s}. \quad (4.17)$$

From this equation and the condition that ligand concentration has to vanish at infinity, we obtain that $s(z) = \bar{s} \exp(-z\sqrt{\gamma})$. Furthermore, by using this result, and the fact that p is at equilibrium too, we obtain from the boundary condition at cell layer that \bar{s} needs to satisfy

$$(1 + \sqrt{\gamma}) \bar{s} = \sigma(\bar{s}/c_0). \quad (4.18)$$

When σ is a Hill function, this is an algebraic equation which, depending on the value of γ , generically has one or three solutions. When the value of γ is sufficiently large, we have $\bar{s}_1 = 0$ as the only solution of Eq. (4.18). A pair of new solutions, \bar{s}_2 and \bar{s}_3 , is created through a saddle-node bifurcation when $\gamma < \gamma_c$, for some $\gamma_c = \gamma_c(c_0) > 0$. This is illustrated in Fig. 4.3 where the nonlinearity is assumed to be a Hill function with $n = 2$.

In this case we can explicitly find the steady states and their dependence on the parameters of the system. In fact the algebraic equation we need to solve is

$$(1 + \sqrt{\gamma}) \bar{s} = \frac{\bar{s}^2}{c_0^2 + \bar{s}^2}, \quad (4.19)$$

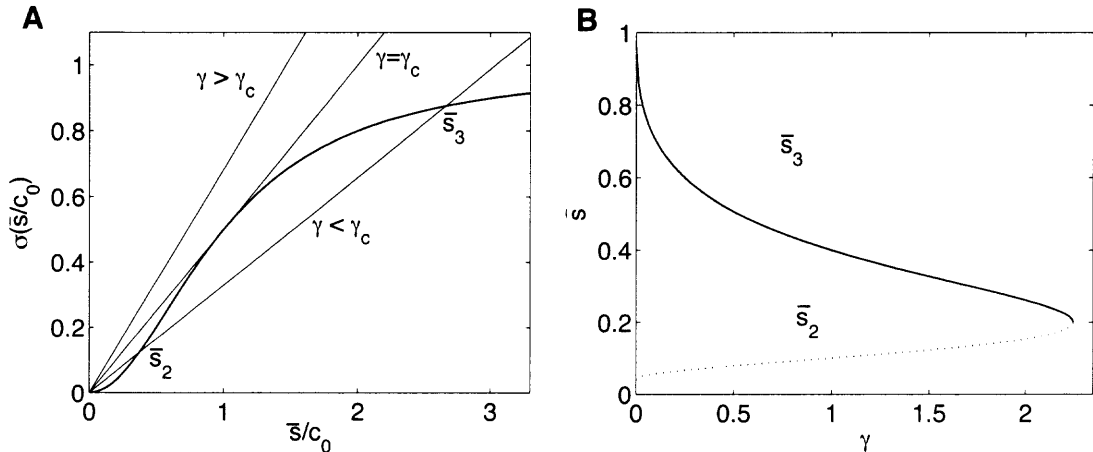


Figure 4.3 Multiplicity of the steady states for Hill nonlinearity with $n = 2$. (A) Three possible scenarios for the solution of Eq. (4.18). (B) The behavior of the two nontrivial solutions s_2 (unstable) and s_3 (stable) as γ increases. In both plots $c_0 = 0.2$.

which has solutions

$$\bar{s}_1 = 0, \quad \bar{s}_{2,3} = \frac{1 \mp \sqrt{1 - 4(1 + \sqrt{\gamma})^2 c_0^2}}{2(1 + \sqrt{\gamma})}. \quad (4.20)$$

From this result we find that the critical value of the degradation coefficient γ_c is

$$\gamma_c = \frac{(1 - 2c_0)^2}{4c_0^2}. \quad (4.21)$$

We need to note that the above steady states can be achieved only if $c_0 < 1/2$. If this is not the case, the only real solution of Eq. (4.19) is the trivial one, independently of the degradation factor γ . This is intuitively obvious, since even in absence of degradation, ligand-induced ligand release can overcome ligand-mediated endocytosis only if $c_0 < 1/2$.

Let us now analyze the stability of these steady state solutions. We linearize Eqs. (4.5), (4.6) and (4.7) with respect to perturbations of the form $\delta p = a e^{-\lambda t - i q x}$

and $\delta s = b(z)e^{-\lambda t - iqx}$ (so that $\text{Re } \lambda < 0$ would signify instability), obtaining

$$b''(z) = (q^2 + \gamma - \lambda)b, \quad \Rightarrow \quad b(z) = Ae^{-z\sqrt{q^2 + \gamma - \lambda}}, \quad (4.22)$$

$$-a\lambda = -a + \frac{\sigma'(\bar{s}/c_0)}{c_0}b(0), \quad (4.23)$$

$$a = -b'(0) + b(0), \quad (4.24)$$

where we dropped the higher order terms of the Taylor expansion of σ about \bar{s}/c_0 and used the fact that $b(z)$ vanishes at infinity.

The above system of equations leads us to the following condition for λ :

$$(1 - \lambda)(1 + \sqrt{\gamma + q^2 - \lambda}) = \frac{\sigma'(\bar{s}/c_0)}{c_0}, \quad (4.25)$$

where the analytic branch of the square root is chosen so that its real part is always positive.

From Eq. (4.25) one can see that λ is always real for $\gamma > 1$ (the opposite case is a little more subtle and will be treated elsewhere). Furthermore, we have $\lambda = 1$ for $\bar{s} = 0$, hence the state of no signaling is always linearly stable.

Under multiple steady states conditions, i.e. for $\gamma < \gamma_c$ we always have three different steady states as depicted in Fig. 4.3 A. Thus, the slope of $\sigma(s)$ at $s = \bar{s}_3$ is always going to be less than the one of the line $1 + \sqrt{\gamma}$. And the opposite happens for the steady state at \bar{s}_2 . Therefore, $0 < \sigma'(\bar{s}_3/c_0) < 1 + \sqrt{\gamma}$ and $\sigma'(\bar{s}_2/c_0) > 1 + \sqrt{\gamma}$. As a result, if we assume $\lambda \leq 0$ when $\bar{s} = \bar{s}_3$, we have that

$$\frac{\sigma'(\bar{s}_3/c_0)}{c_0} = (1 - \lambda)(1 + \sqrt{\gamma + q^2 - \lambda}) \geq (1 + \sqrt{\gamma + q^2 - \lambda}) > 1 + \sqrt{\gamma}, \quad (4.26)$$

which is impossible. Therefore, $\lambda > 0$ for all q , and the steady state \bar{s}_3 is linearly stable whenever it exists. This result is shown in Fig. 4.4 (B) where we can see that the value of λ is always greater than zero. From Fig. 4.4 (A) we notice that the steady state \bar{s}_2 is unstable for small values of q .

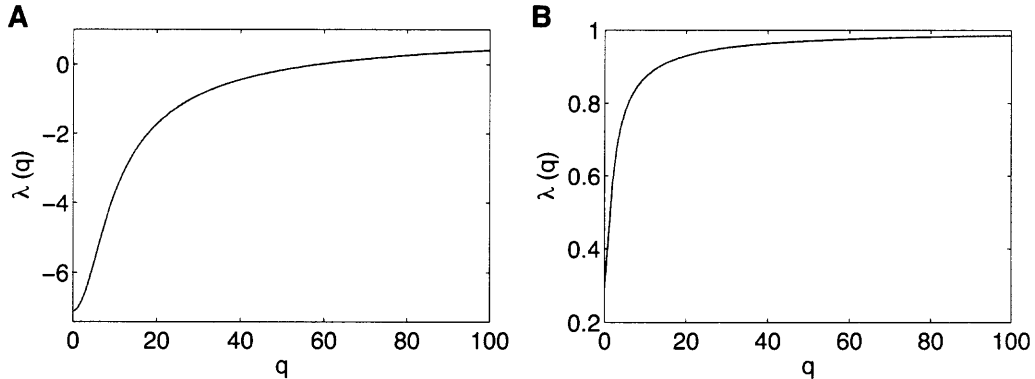


Figure 4.4 Dependence of λ upon q for the steady states s_2 (subplot A) and s_3 (subplot B). For this study we used $\gamma = 0.3$ and $c_0 = 0.1$.

Thus, although we started this discussion by highlighting the fact that model (4.5)-(4.7) may not have the same properties as the bistable equation (4.11), we found that the steady states of the degradation model are very similar to simple reaction-diffusion problems with bistable nonlinearities, as e.g., in Eq. (4.11) [41, 22].

To summarize the analysis above, our model exhibits signaling bistability when the threshold of signaling c_0 is below a certain value and whenever the volume degradation rate $\gamma < \gamma_c(c_0)$. Bistability is destroyed when the volume degradation is sufficiently strong, an intuitively expected result since under this condition the majority of ligand molecules will degrade before being able to reach an empty receptor.

In the steady state the effect of bulk degradation is essentially to enhance the removal of the ligands from the epithelium surface by a factor of $1 + \sqrt{\gamma}$. Let us point out the square root dependence of the enhancement factor on γ . This implies that the additional effect of bulk degradation can remain quite strong even for relatively small values of k_{deg} .

4.4 Stationary Fronts

Now that we have established the existence of bistability for the model, we want to study stationary front solutions connecting the two stable equilibria $s|_{z=0} = 0$ and $s|_{z=0} = \bar{s}_3$.

Without the loss of generality, we may assume that this front is parallel to the y -axis. After setting all the time and y -derivatives in Eqs. (4.5) – (4.7) to zero, we can eliminate p , thus arriving at the following boundary-value problem for s alone:

$$\frac{\partial^2 s}{\partial x^2} + \frac{\partial^2 s}{\partial z^2} - \gamma s = 0, \quad \left(\frac{\partial s}{\partial z} - s + \sigma(s/c_0) \right) \Big|_{z=0} = 0. \quad (4.27)$$

Since we are looking for stationary fronts connecting \bar{s}_3 to 0, we determine that the following conditions need to be satisfied as $x \rightarrow \pm\infty$ in order to have these type of heteroclinic x -independent stationary solutions of Eq. (4.27):

$$\lim_{x \rightarrow -\infty} s(x, z) = \bar{s}_3 \exp(-\sqrt{\gamma}z), \quad \lim_{x \rightarrow +\infty} s(x, z) = 0. \quad (4.28)$$

To be able to characterize these heteroclinic orbits using Eqs. (4.27) and (4.28), we need to determine a solvability condition. This is not a trivial task due the non-local character of the problem.

We looked at the literature for these type of problems. We found that in a recent paper the authors studied solutions for a general nonlinear problem similar to Eq. (4.27), except that they have $\gamma = 0$ [12]. In particular, one of their driving ideas was to extend the knowledge of the Peierls-Nabarro problem from [81, 58] to more general systems. Of course, the Peierls-Nabarro problem they refer to, is the same one that we studied numerically in Chapter 3.

While looking at the problem in n dimensions, the authors were able to establish existence of front solutions to Eqs. (4.27) and (4.28) in a special case of $\gamma = 0$ [12]. They obtained a solvability condition from an observation that Eq. (4.27), viewed as an infinite-dimensional dynamical system with x playing the role of time, possesses

a kind of Hamiltonian structure leading to the existence of a conserved quantity as a function of x .

Since the linear degradation term is the only difference between our problem and theirs, we can follow the arguments in [12] in our problem. For each x define the functional

$$E[s(x, \cdot)] = \frac{1}{2}s^2(x, 0) - \int_0^{s(x, 0)} \sigma(s'/c_0) ds' + \frac{1}{2} \int_0^\infty \left\{ \left(\frac{\partial s}{\partial z} \right)^2 + \gamma s^2 \right\} dz. \quad (4.29)$$

Then, multiplying the first equation in (4.27) by $\partial s/\partial x$ and integrating z

$$\int_0^\infty \frac{\partial s}{\partial x} \frac{\partial^2 s}{\partial x^2} dz + \int_0^\infty \frac{\partial s}{\partial x} \frac{\partial^2 s}{\partial z^2} dz - \gamma \int_0^\infty \frac{\partial s}{\partial x} dz = 0, \quad (4.30)$$

we can use the chain rule to rewrite the first and last terms to get

$$\frac{\partial}{\partial x} \left[\int_0^\infty \frac{1}{2} \left(\frac{\partial s}{\partial x} \right)^2 dz \right] + \int_0^\infty \frac{\partial s}{\partial x} \frac{\partial^2 s}{\partial z^2} dz - \frac{\partial}{\partial x} \left[\int_0^\infty \frac{1}{2} \gamma s^2 dz \right] = 0, \quad (4.31)$$

while for the middle term, we use integration by parts and the boundary condition from the second equation in (4.27) together with the fact that the function vanishes as $z \rightarrow \infty$, to obtain:

$$\int_0^\infty \frac{\partial s}{\partial x} \frac{\partial^2 s}{\partial z^2} dz = \frac{\partial s(x, 0)}{\partial x} \left(s(x, 0) - \sigma \left(\frac{s(x, 0)}{c_0} \right) \right) - \frac{\partial s}{\partial x} \left[\int_0^\infty \frac{1}{2} \left(\frac{\partial s}{\partial z} \right)^2 dz \right], \quad (4.32)$$

after two more applications of the chain rule in the above equation and rearranging the terms, we can use the definition of the energy functional E in Eq. (4.29) to write the following equation

$$\frac{d}{dx} \left\{ E[s(x, \cdot)] - \frac{1}{2} \int_0^\infty \left(\frac{\partial s}{\partial x} \right)^2 dz \right\} = 0. \quad (4.33)$$

Since in the limit $x \rightarrow \pm\infty$ we must have $\partial s/\partial x \rightarrow 0$, integrating Eq. (4.33) over x and using Eqs. (4.28), we obtain the solvability condition:

$$E[\bar{s}_3 \exp(-\sqrt{\gamma}z)] = 0. \quad (4.34)$$

This formula can be further expressed in terms of \bar{s}_3 only. Performing the z -integration, we obtain an equivalent condition

$$\frac{1}{2}(1 + \sqrt{\gamma})\bar{s}_3^2 - \int_0^{\bar{s}_3} \sigma(s/c_0)ds = 0. \quad (4.35)$$

This is an analogue of Eq. (4.14) defining the threshold value of $\gamma = \gamma_0$ beyond which the autocrine loop cannot be switched on by a localized stimulus.

The value of γ_0 can be explicitly calculated in the case when σ is a Hill function with $n = 2$. Here, the solvability condition of Eq. (4.35) becomes

$$\frac{1}{2}(1 + \sqrt{\gamma_0})\bar{s}_3^2 - \int_0^{\bar{s}_3} \frac{s^2}{c_0^2 + s^2} ds = 0, \quad (4.36)$$

and γ_0 needs to satisfy:

$$\frac{\bar{s}_3^2}{2}(1 + \sqrt{\gamma_0}) - \bar{s}_3 + c_0 \arctan\left(\frac{\bar{s}_3}{c_0}\right) = 0, \quad (4.37)$$

where \bar{s}_3 is given by Eq. (4.20) with $\gamma = \gamma_0$. We can plot the obtained threshold value of γ_0 vs. \bar{s}_3 parametrically as a function of c_0 . The result, together with several bifurcation curves, is shown in Fig. 4.5. This figure shows how the parameter region in which autocrine signaling can be switched on, located above the dashed line, is smaller compared to the region of multiple steady state solutions.

We can also compute the autocrine loop activation threshold in another extreme when the Hill nonlinearity is replaced with a Heaviside function: $\sigma(x) = H(x - 1)$ (corresponding to the limit of a very sharp nonlinearity, $n = \infty$ in the Hill function). In this case it is easy to see from Eq. (4.18) that multiple steady states exist whenever $\gamma < \gamma_c = (1 - c_0)^2/c_0^2$, as long as $c_0 < 1$. Once again, substituting the Heaviside function into Eq. (4.35), we find that the autocrine loop activation threshold is given by

$$\gamma_0 = \frac{(1 - 2c_0)^2}{4c_0^2}, \quad c_0 < \frac{1}{2}. \quad (4.38)$$

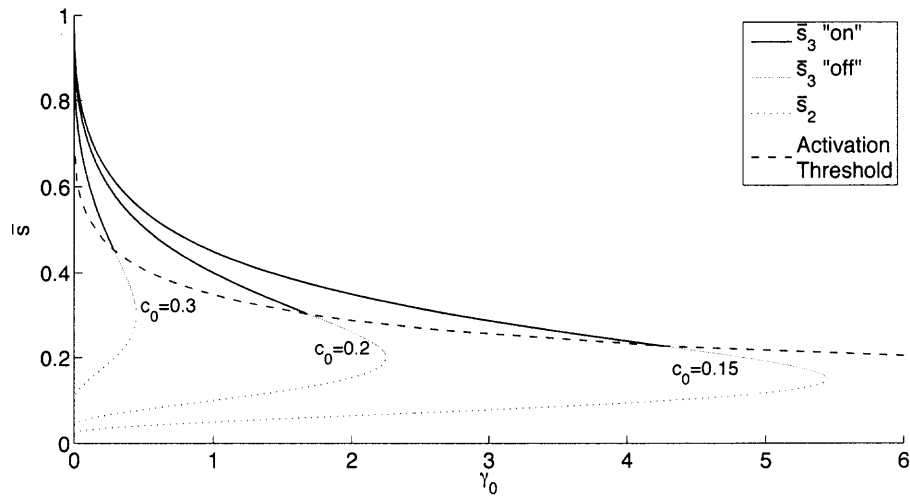


Figure 4.5 Steady state bifurcation diagram superimposed on the plot of the autocrine loop activation threshold curve for Hill nonlinearity with $n = 2$.

A parametric plot of this dependence is shown in Fig. 4.6. Note a significant drop in the value of c_0 needed for autocrine signaling to take place even for relatively small values of γ , due to the $\sqrt{\gamma}$ dependence at small γ .

In the case of the Hill function with a general value of n , it is still possible to analyze the autocrine loop activation threshold γ_0 numerically. Let us also point out that these results are not very different from those obtained in the case when the Hill function is replaced with the Heaviside function. In Fig. 4.7 we compare the parametric relation between c_0 and γ_0 for several values of n . One can see that the Heaviside function gives a very good approximation to the activation threshold for the entire range of values of n . Also, note that for fixed c_0 the threshold γ_0 increases monotonically with n , with the $n = 2$ result in Eq. (4.37) providing the lower bound and the Heaviside result in Eq. (4.38) providing the upper bound, respectively.

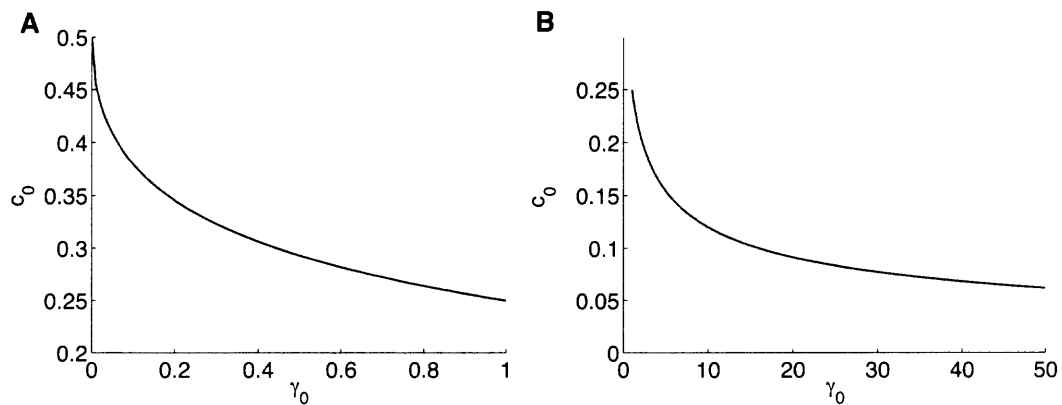


Figure 4.6 Autocrine loop activation threshold in the case of the Heaviside nonlinearity.

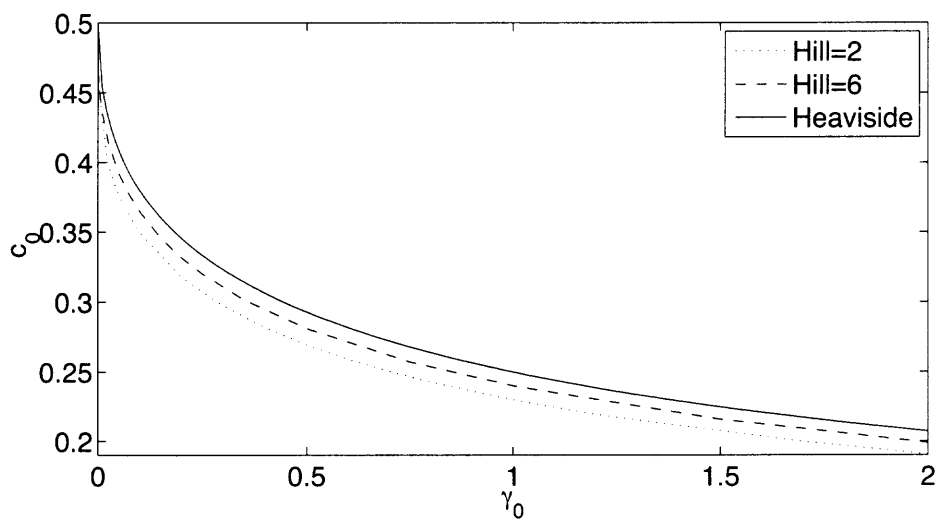


Figure 4.7 Autocrine loop activation threshold: comparison between the Hill and the Heaviside nonlinearities.

4.5 Traveling Waves

When the values of c_0 and γ are below the activation threshold, one would expect that a sufficiently localized stimulus applied to the epithelium would result in switching the signaling activity on.

In the case of Eq. (4.11) this “ignition” phenomenon is rather well understood [25, 26, 27, 4, 41, 55]. Here, a localized perturbation of sufficient strength and size evolves into a radially diverging wave of signaling [4, 39]. The role of the feedback in this process is to relay the signaling activity to remote regions of the epithelium from the point of origination. This signal propagates through the epithelium by means of a special type of solution: a traveling front, i.e. a solution of Eqs. (4.5) – (4.7) of the form

$$s = s(x - vt, z), \quad p = p(x - vt), \quad (4.39)$$

where v is the constant propagation velocity which is characterized by a monotonically increasing level of signaling. Traveling front solutions are also translation invariant, and connect two different steady states of a given bistable system such as the one we are dealing with (at least for certain values of parameters c_0 and γ as discussed in the previous section).

Substituting the ansatz from Eq. (4.39) into Eqs. (4.5) – (4.7), we find that the traveling wave solutions satisfy the following nonlinear boundary-value problem, together with Eq. (4.28):

$$\frac{\partial^2 s}{\partial x^2} + \frac{\partial^2 s}{\partial z^2} + \alpha v \frac{\partial s}{\partial x} - \gamma s = 0, \quad z > 0, \quad (4.40)$$

$$v \frac{\partial p}{\partial x} - p + \sigma(c/c_0) = 0, \quad c(0) = c_0, \quad (4.41)$$

$$\left(\frac{\partial s}{\partial z} - s \right) \Big|_{z=0} = -p, \quad c(x) = s(x, 0), \quad (4.42)$$

where the value of c at the origin is chosen to fix translations.

As we noted earlier in this work, despite the similarities of the model described by Eqs. (4.5) – (4.7) and that of Eq. (4.11), because of the non-local character of the spatial coupling, it is not immediately obvious whether the system under consideration can sustain traveling waves in the presence of bulk degradation. This scenario is also different from that in Chapter 2 where we demonstrated existence of traveling wave solutions and signal propagation for a similar class of non-local problems in which the ligand dynamics in the extracellular space is governed by pure diffusion (see also similar results in presence of purely diffusing ligand dynamics in [62]).

Here instead, we investigate the existence and properties of the traveling wave solutions in the presence of bulk degradation.

One can use Fourier transform techniques to study existence of traveling wave solutions in the special case of a sharp threshold nonlinearity, in which the Hill function in Eq. (4.7) can be replaced with a Heaviside step. This analysis is outlined in the last section of this Chapter. There, we find that traveling front solutions with speed $v > 0$ exist and are unique (up to translations) for all values of α , as long as $c_0 < 1/2$ and $\gamma < \gamma_0$, with γ_0 given precisely by Eq. (4.38). In other words, the front of signaling activation persists in the presence of ligand volume degradation when the strength of this degradation is not too high. The profile of one such solution for a particular choice of the parameters is shown in Fig. 4.8. In particular, one can see from this figure that, as expected, the high level of signaling remains tightly localized in the vicinity of the epithelium. The figure was generated by applying numerical integration to the integral expressions in Eq. (4.61).

Also, the velocity v of the front as a function of model parameters for the Heaviside nonlinearity is given parametrically by the following expression (see Sec. 4.6):

$$c_0 = \frac{1}{\pi} \int_{(\alpha v + \sqrt{\alpha^2 v^2 + 4\gamma})/2}^{\infty} \left\{ \frac{\sqrt{s^2 - \alpha v s - \gamma}}{s(1 + vs)(s^2 - \alpha v s - \gamma + 1)} \right\} ds. \quad (4.43)$$

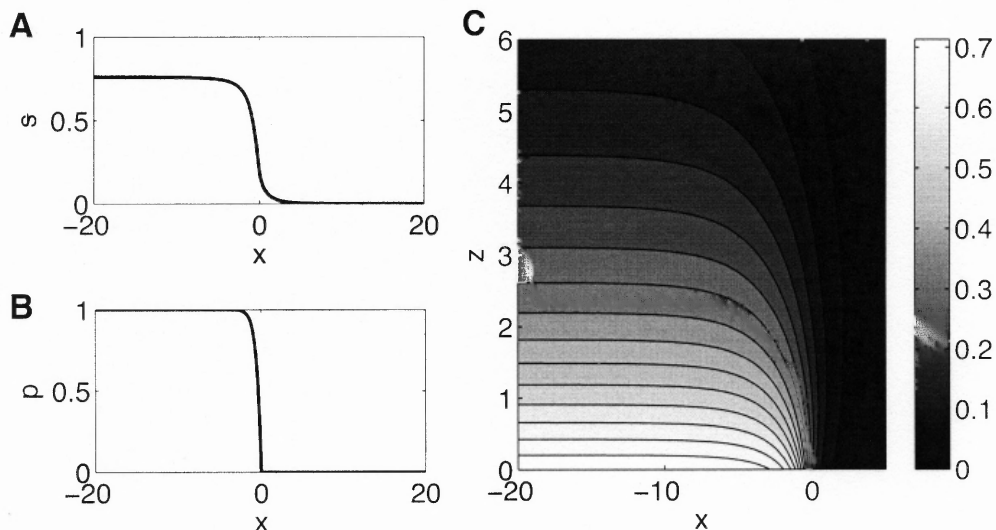


Figure 4.8 The profiles of a traveling wave solution at $\alpha = 0.2$, $\gamma = 0.1$, $c_0 = 0.188$. In (A) and (B), the distributions of $s(x, 0)$ and $p(x)$ are shown, in (C) a contour plot of $s(x, z)$ is shown.

The dependence of c_0 on v for several values of α at fixed γ is presented in Fig. 4.9. This figure also shows two limiting behaviors as $\alpha \rightarrow 0$, corresponding to quasi-stationary diffusion of ligands in the extracellular space, and $\alpha \rightarrow \infty$, corresponding to instantaneous protease response to changes in the ligand concentrations at the epithelium surface. One can see that when $\alpha \ll 1$, the solution is well approximated by neglecting the time derivative in Eq. (4.5), whereas when $\alpha \gg 1$ the solution can be well approximated by neglecting the time derivative in Eq. (4.6).

We also studied the dependence of the propagation velocity v on the bulk degradation rate γ for several values of the threshold c_0 at fixed α , Fig. 4.10A, and for several values of α at fixed c_0 , Fig. 4.10B. For all the parameters in Fig. 4.10, there exists a traveling wave solution with $v > 0$ at $\gamma = 0$. As the value of γ is increased, the propagation velocity v decreases, and when γ reaches γ_0 , the propagation velocity vanishes. Note that for $\gamma \ll 1$ the dependence of v on γ is approximately linear. This

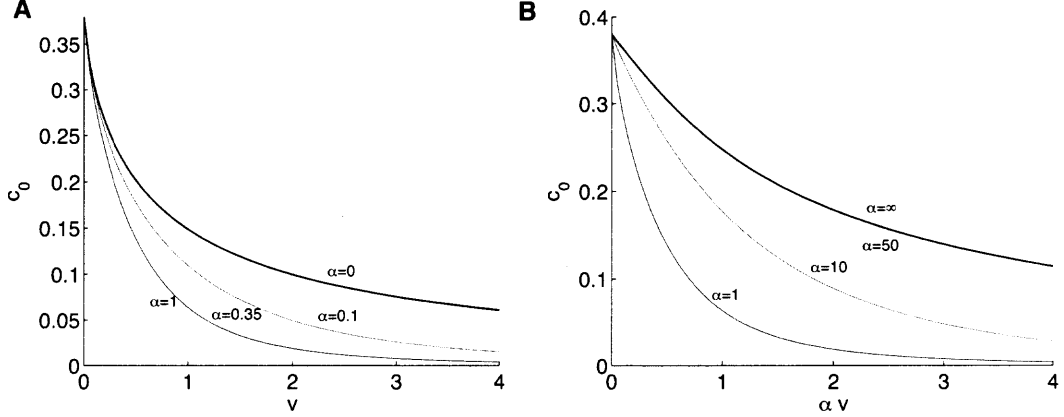


Figure 4.9 Relation between the traveling wave velocity v and the activation threshold c_0 for different values of α at $\gamma = 0.1$, obtained from Eq. (4.43).

is in contrast with the $\sqrt{\gamma}$ dependence of the propagation threshold c_0 on γ in Eq. (4.38) for small γ .

Finally, we studied how much the propagation velocity in the problem with a general Hill nonlinearity deviates from the exact solution obtained for the Heaviside nonlinearity in Eq. (4.43). The results for numerical studies of the propagation velocity for several values of the Hill coefficient and other fixed parameters are presented in Fig. 4.11.

To obtain these results we used a numerical method consisting of forward difference in time, centered difference for the transversal Laplacian and optimal grids for the discretization along the vertical direction, obtaining the scheme

$$\alpha \frac{s_{j,k}^{t+\Delta t} - s_{j,k}^t}{\Delta t} = \frac{s_{j+1,k}^t - 2s_{j,k}^t + s_{j-1,k}^t}{h_{\perp}^2} + \frac{1}{h_k} \left(\frac{s_{j,k+1}^t - s_{j,k}^t}{h_{k+1/2}} - \frac{s_{j,k}^t - s_{j,k-1}^t}{h_{k-1/2}} \right) - \gamma s_{j+1,k}^t, \quad (4.44)$$

$$\frac{p_j^{t+\Delta t} - p_j^t}{\Delta t} = -p_j^t + \frac{(s_{j,k}^t)^n}{(c_0)^n + (s_{j,k}^t)^n}, \quad (4.45)$$

where t is the time index, j represents the discretization along the x direction, and k is the optimal grid index along the vertical direction. We used the standard optimal grid

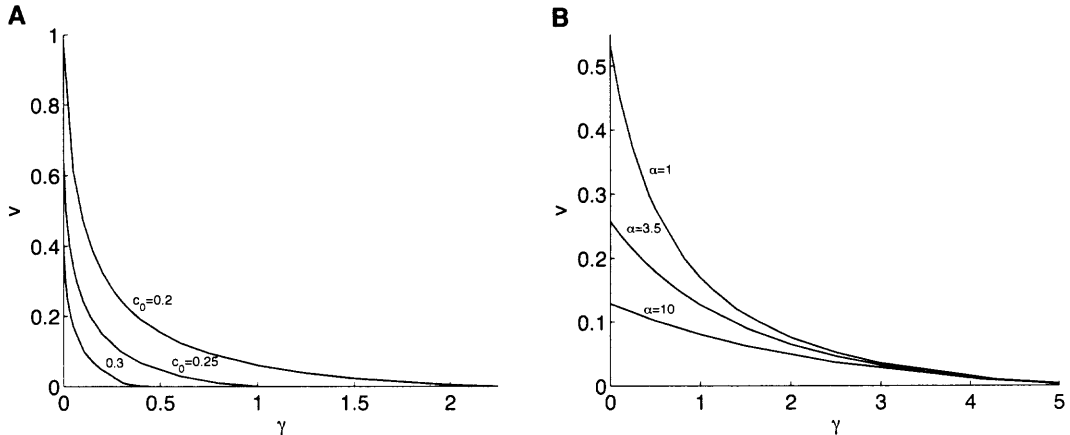


Figure 4.10 Dependence of the propagation velocity v on γ for different values of c_0 (A) and α (B), obtained from Eq. (4.43). In A, $\alpha = 0.1$, in B, $c_0 = 0.15$.

treatment of the boundary condition at $z = 0$ (e.g. $k = 0$), a homogeneous Dirichlet boundary condition at $k = n_{og}$ (in the case n_{og} means the size of the optimal grid, to avoid confusion with the Hill coefficient), and no flux boundary conditions at $j = 0, m$.

It is not obvious from our discussion in Chapter 3 that we can use the optimal grids method in connection with such a parabolic problem. However, in [6], the authors successfully applied the problem for the solution of hyperbolic problems. Furthermore, we can think of the use of the optimal grid approach in time-dependent problems as solving an elliptic one in the Laplace transform space. For instance, given the problem

$$s_t = s_{zz} + \Delta_{\perp} s - \gamma s, \quad (4.46)$$

if we take the Fourier transform of s with respect to x and y , and the Laplace transform with respect of time

$$\hat{S} = \int_0^{\infty} \int_{-\infty}^{\infty} \int_{-\infty}^{\infty} s(t, x, y, z) e^{-rt + iq_1 x + iq_2 y} dx dy dt, \quad (4.47)$$

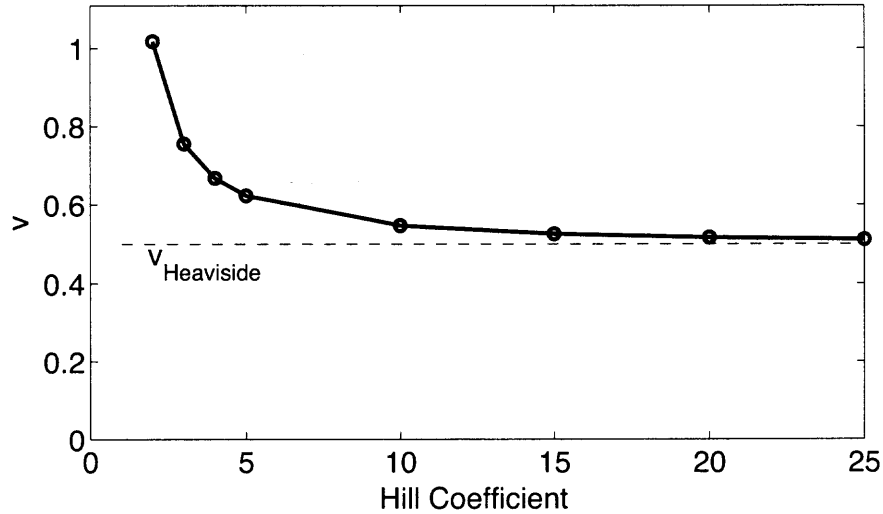


Figure 4.11 Dependence of the propagation velocity on the Hill coefficient at $\gamma = 0.25$, $\alpha = 0.1$, $c_0 = 0.1594756$, obtained from the numerical solution of Eqs. (4.5) – (4.7).

the above equation reduces to

$$\hat{S}_{zz} - \lambda \hat{S} = 0, \quad \lambda = \gamma + q_1^2 + q_2^2 + r, \quad (4.48)$$

where q_1, q_2 are due to the Fourier transform and r is the Laplace variable.

Using this notation we can suppose that for a range of values of λ the optimal grid approximation will be valid even for the parabolic problem, and this is actually the result that we obtain through our simulations.

Going back to Fig. 4.11, one can see that in the considered case the deviation is more significant than in the case considered in [62] at small Hill coefficients. Nevertheless, for sufficiently sharp Hill nonlinearities (i.e. when $n \gtrsim 4$) the Heaviside function gives a good approximation ($\lesssim 20\%$ accurate) of the propagation velocity for the considered parameter values.

4.6 Exact Traveling Wave Solutions

If we use as nonlinearity $\sigma(c/c_0) \approx H(c/c_0)$, where H is the Heaviside step function and c_0 is the activation threshold, we can find an integral form for the traveling wave solutions of Eq. (4.5).

We assume that the solution is a traveling front propagating along the x -axis with constant velocity v , i.e. $s = s(x - vt, z)$, $c = c(x - vt)$, and $p = p(x - vt)$. Then, if $c(x)$ is a monotonically decreasing function of x , (4.5) can be rewritten as

$$\frac{\partial^2 s}{\partial x^2} + \frac{\partial^2 s}{\partial z^2} + \alpha v \frac{\partial s}{\partial x} - \gamma s = 0, \quad z > 0, \quad (4.49)$$

$$v \frac{\partial p}{\partial x} - p + H(-x) = 0, \quad c(0) = c_0, \quad (4.50)$$

$$\left(\frac{\partial s}{\partial z} - s \right) \Big|_{z=0} = -p, \quad c(x) = s(x, 0), \quad (4.51)$$

where, without loss of generality, we assumed that the threshold $c = c_0$ is reached at the origin.

We can solve Eq. (4.50) using the continuity condition $p(0) = 0$. Thus obtaining

$$p(x) = \begin{cases} 0, & x \geq 0, \\ 1 - e^{x/v}, & x < 0. \end{cases} \quad (4.52)$$

We now Fourier-transform with respect to x to find the z dependency of s in Fourier space. We use the following conventions:

$$\hat{s}_q(z) = \int_{-\infty}^{+\infty} e^{-iqx} s(x, z) dx, \quad \hat{p}_q = \int_{-\infty}^{+\infty} e^{-iqx} p(x) dx. \quad (4.53)$$

Using the above definitions, and solving the resulting o.d.e. in Fourier space, we find that $s(x, z)$ is given by the integral expression:

$$s(x, z) = \frac{1}{2\pi} \lim_{\epsilon \rightarrow 0} \int_{-\infty}^{\infty} \frac{(1 - \epsilon v) e^{-\sqrt{q^2 + \gamma - i\alpha v q} z + i q x}}{(\epsilon - i q) (1 - i v q) (\sqrt{q^2 + \gamma - i\alpha v q} + 1)} dq, \quad (4.54)$$

where the presence of ϵ is due to the Fourier transform of p (\hat{p}_q):

$$\hat{p}_q = \lim_{\epsilon \rightarrow 0} \frac{1 - \epsilon v}{(\epsilon - iq)(1 - ivq)}. \quad (4.55)$$

It is possible to write the complex integral of Eq. (4.54) as a real one by using contour integration techniques. For the purpose of choosing the appropriate contour, we found that the integrand has two simple poles at $q_1 = -i\epsilon$, and $q_2 = -i/v$; and also two branch points at $q_{3,4} = i(\alpha v \mp \sqrt{\alpha^2 v^2 + 4\gamma})/2$. Since we want to find the integral along the real line, we choose the branch cuts to extend from $q_{3,4}$ toward minus and plus infinity, respectively. Using this setup, we can find a real expression for $s(x, z)$ when $x \leq 0$ by using the contour portrayed in Fig. 4.12. For this contour choice we assume that $|q_2| > |q_3|$. This is not always true, but the other case leads to a more straightforward calculation, and both cases give the same result.

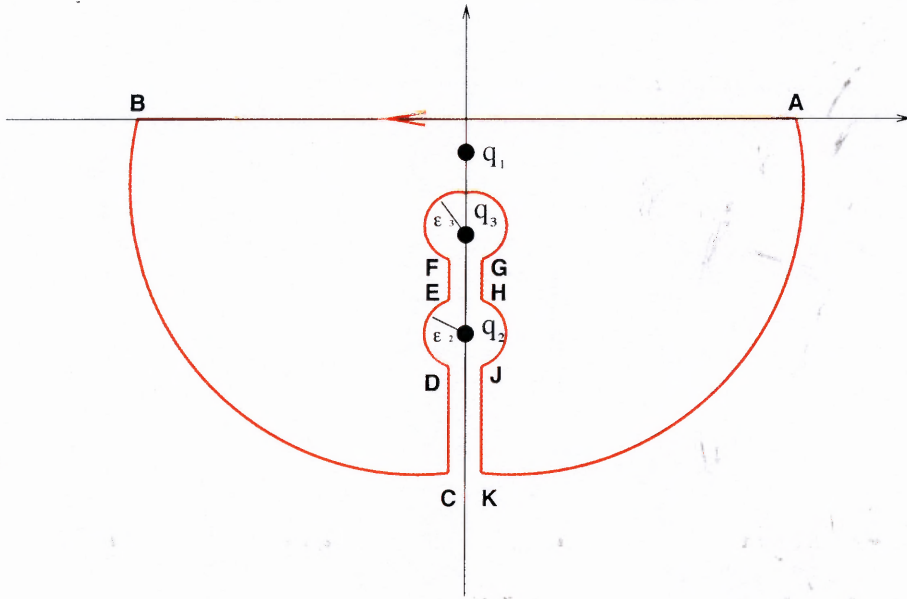


Figure 4.12 Contour for the integral of Eq.(4.56).

Applying Cauchy's Residue Theorem to the integrand in Eq. (4.54) around the contour $\Gamma = ABCDEFGHJKA$ we have:

$$\int_{\Gamma} \frac{(1 - \epsilon v) e^{-\sqrt{q^2 + \gamma - i\alpha v q} z + iqx}}{(\epsilon - iq)(1 - ivq) \left(\sqrt{q^2 + \gamma - i\alpha v q} + 1 \right)} dq = 2\pi i \text{Res}(-i\epsilon). \quad (4.56)$$

The integral to the left is given by the sum of the line integrals that characterize the contour. Of these line integrals, \int_B^C and \int_K^A vanish in the limit as the radius tending both arcs goes to infinity. The integral around the branch point q_3 also disappears in the limit as ϵ_3 goes to zero. The remaining ones all contribute to the final result.

In the limit as ϵ_2 goes to zero we find that:

$$\int_C^D \dots + \int_E^F \dots = \int_{-\infty}^{Im(q_3)} \frac{i(1 - \epsilon v) e^{-i\sqrt{q^2 - \gamma - \alpha v q} z - xq}}{(\epsilon + q)(1 + vq) \left(i\sqrt{q^2 - \gamma - \alpha v q} + 1 \right)} dq. \quad (4.57)$$

$$\int_G^H \dots + \int_J^K \dots = - \int_{-\infty}^{Im(q_6)} \frac{i(1 - \epsilon v) e^{i\sqrt{q^2 - \gamma - \alpha v q} z - xq}}{(\epsilon + q)(1 + vq) \left(-i\sqrt{q^2 - \gamma - \alpha v q} + 1 \right)} dq. \quad (4.58)$$

For the two remaining integrals we have:

$$\int_D^E \dots + \int_H^J \dots = 2\pi i \text{Res}(-i/v) = 2\pi \frac{e^{\frac{x}{v} - \sqrt{\gamma - \alpha - \frac{1}{v^2}} z}}{1 + \sqrt{\gamma - \alpha - \frac{1}{v^2}}}. \quad (4.59)$$

Combining the results from Eq.'s (4.56), (4.57), (4.58), and (4.59) and taking the limit as ϵ goes to zero, we obtain the following integral expression for $s(x, z)$:

$$\begin{aligned} s(x, z) &= \frac{1}{\pi} \int_{-\infty}^{(\alpha v - \sqrt{\alpha^2 v^2 + 4\gamma})/2} \frac{e^{-xq} \sin \left(z \sqrt{q^2 - \gamma - \alpha v q} \right)}{q(1 + vq)(1 + q^2 - \gamma - \alpha v q)} + \\ &+ \frac{\sqrt{q^2 - \gamma - \alpha v q} e^{-xq} \cos \left(z \sqrt{q^2 - \gamma - \alpha v q} \right)}{q(1 + vq)(1 + q^2 - \gamma - \alpha v q)} dq \\ &+ \frac{e^{-\sqrt{\gamma} z}}{1 + \sqrt{\gamma}} - \frac{e^{\frac{x}{v} - \sqrt{\gamma - \alpha - \frac{1}{v^2}} z}}{1 + \sqrt{\gamma - \alpha - \frac{1}{v^2}}}. \end{aligned} \quad (4.60)$$

This integral is only valid for nonpositive values of x . An integration around a similar contour, but on the positive half-plane will give the value of $s(x, z)$ for positive values of x . We carried out the calculations and found that:

$$\begin{aligned}
 s(x, z) = & \int_{(\alpha v + \sqrt{\alpha^2 v^2 + 4\gamma})/2}^{\infty} \frac{e^{-xq} \sin\left(z\sqrt{q^2 - \gamma - \alpha vq}\right)}{\pi q (1 + vq) (q^2 - \alpha vq - \gamma + 1)} + \\
 & + \frac{\sqrt{q^2 - \alpha vq - \gamma} e^{-xq} \cos\left(\sqrt{q^2 - \alpha vq - \gamma} z\right)}{\pi q (1 + vq) (q^2 - \alpha vq - \gamma + 1)} dq. \tag{4.61}
 \end{aligned}$$

Note that, by using the condition $s(0, 0) = c_0$ on the above equation, we obtain Eq. (4.43).

To summarize, we showed that even in presence of degradation in the bulk, there is a wide range of parameters that lead to multiple steady states for the model of Eqs. (4.5)–(4.7). Furthermore, we showed the existence of traveling fronts connecting two stable states. Although the range of parameters for which the model admits traveling wave solutions is smaller than the multiple steady states range of parameters.

CHAPTER 5

CONCLUSIONS AND FUTURE RESEARCH

This work has been devoted toward two main goals: the development of an extension to the optimal grids method, and the analysis of the existence of traveling front solutions in a model epithelium that accounts for degradation in the bulk.

In Chapter 3, we presented the method of optimal geometric grids for elliptic problems in unbounded domains. This method was introduced by Druskin in [18] and has been successfully applied to various problems such as the computation of stray magnetic fields [50]. We showed that it is possible to improve the method so that the essentially spectral properties of the optimal grids approximation are not lost when this method is coupled with a less accurate discretization technique to solve problems in higher dimensions.

As a result, we are able to render superconvergent a second order scheme such as centered finite difference for a one dimensional second order derivative, with only the addition of few discretization points on the direction normal to the one of the lower order scheme. This is extremely impressive, and comparable to an FFT approach in terms of computational complexity.

However, as we mentioned at the end of Chapter 3, the compensated optimal grid method has a few advantages over FFT. We did not really exploit these advantages in details and one of our future goals is to do so.

In particular, we stated that the compensation approach can be extended to nonregular grids in a more effective way than FFT. This is one of the reason why we developed the method in the first place, since we envision it as one of the cornerstones for the implementation of more realistic geometrical shapes of the epithelium. In fact, we have developed an algorithm able to handle an arbitrary bounded domain. We are

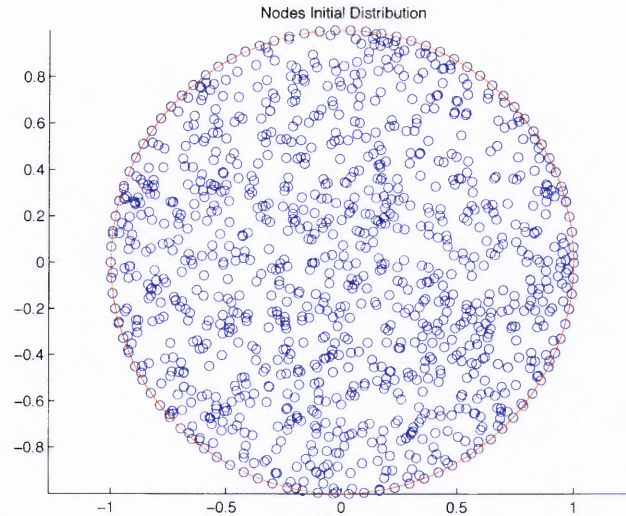


Figure 5.1 The user input a number of nodes is randomly placed on a prescribed geometrical shape.

testing it for simple model problems and hope to soon be able to apply it practical signaling problems.

For instance, let us suppose that we want to solve a problem in a disk, and that we want to obtain a hexagonal tessellation on the transversal plane and optimal gris along the vertical direction, with the goal of using the finite volume scheme from Chapter 3. We propose a general approach for this task that is depicted in Figs. 5.1, 5.1 and 5.3. The first step is to select the number of nodes that we want to use to represent the given domain, then these points are placed randomly on the domain, with the only constraint being that points cannot be too close to each other (this constraint is not necessary but makes the following step faster). The result for this first step for a circular domain is shown in Fig. 5.1. The next step is to use a simulated annealing algorithm [43, 47] to rearrange the nodes so that they occupy the domain in which we want to solve the problem in a “regular” configuration. Briefly, the simulated annealing algorithm is a Monte-Carlo method in which at each iteration the state of the system is measured using a problem-specific energy function, then

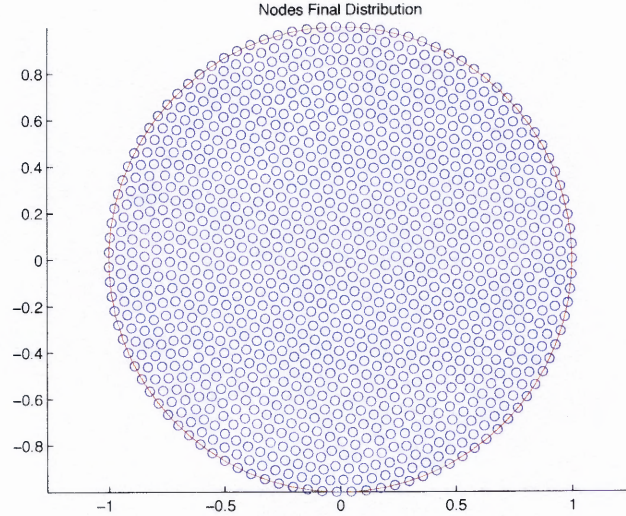


Figure 5.2 A simulated annealing algorithm rearranges the nodes to minimize a given penalty function that is selected with the goal of achieving a regular configuration of nodes.

a random perturbation to the system is introduced. The perturbed configuration is accepted if it is a configuration of lower energy than the previous one or by a random acceptance process (to sample as many configurations as possible) that is made more stringent as the system approaches a state of low energy.

In our case, we choose a penalty function that should give a lower energy configuration that corresponds to a regular discretization in which each point is positioned at the vertex of an hexagon. To achieve this regular configuration we could choose:

$$E[(x_j, y_j)] = \sum_{j' \in \mathcal{N}_j} k_1 [(x_j - x_{j'})^2 + (y_j - y_{j'})^2] + k_2 \left[\frac{1}{(x_j - x_{j'})^2 + (y_j - y_{j'})^2} \right], \quad (5.1)$$

where by \mathcal{N}_j we indicate the set of the sixth closest neighbors to the j -th node, and k_1, k_2 are two constants. This is the energy function we used to obtain the results in Fig. (5.2) with $k_1 = 1$, and $k_2 = 1$.

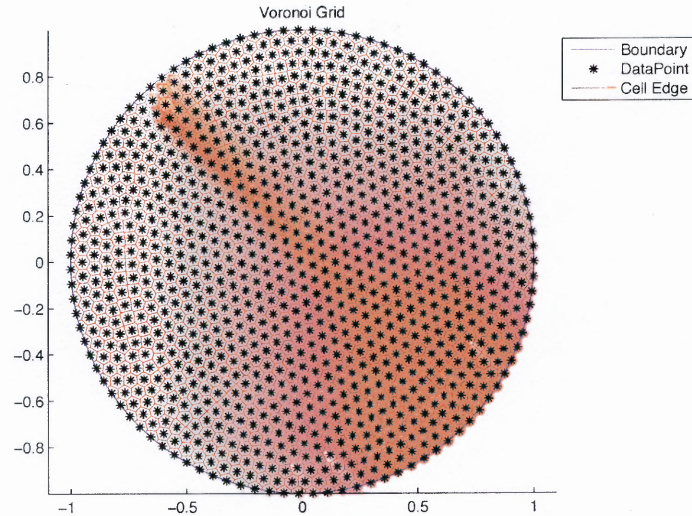


Figure 5.3 Voronoi partitioning of the given domain.

While the results that we obtain with this approach are not as good as the ones in Fig. 3.7, we believe that we can still achieve at least second order convergence if we use a Voronoi tessellation of the domain in the transversal direction, and discretize it using a finite volume scheme that takes advantage of the properties of Voronoi tessellation. Such a tessellation is shown in Fig. 5.3 for the annealed grid of Fig. 5.2.

At present time, we are still experimenting using toy problems, such as solving for the Bessel function in a disk with base given by the circle of Fig. 5.3. The results are encouraging, however, there is still much more work that needs to be done especially for the annealing step before we can reach any valid conclusion.

Related to these studies, but with a different biophysical approach, there is the goal to apply this general idea of partitioning of the epithelium to problems in which cell signaling is analyzed with each cell treated individually, i.e. a discrete version of the continuum model we have analyzed so far.

This discrete approach has been used in [61] and we could use it to answer some questions about cell signaling in presence of cells with different signaling capabilities, for example some of the cell could act as sink with respect to the diffusing ligands.

The other main analysis of this thesis was done in Chapter 4, where we analyzed a mathematical model of ligand mediated signaling in an idealized epithelium in the presence of degradation in the bulk. In this setting it is not obvious that the system exhibits steady states multiplicity and whether it has traveling front solutions connecting different stable steady states. We showed that this is indeed the case, by first using an appropriate energy functional to find the conditions on parameters of the system for which bi-stability is achieved, using an approach similar to the one introduced by [12] for a reaction-diffusion equation in an n -dimensional space.

After establishing the existence of two different steady state, we looked for traveling front solutions of the system, i.e. solutions of the form $s(x - vt)$, $p(x - vt)$. In particular we were able to analytically determine the properties of these traveling fronts for the case of a Heaviside nonlinearity in the ligand activation term. And to numerically show how the traveling wave front solutions for the case of a Hill nonlinearity converge toward the Heaviside setup as the Hill coefficient tends to infinity.

In the near future we are going to do a more thorough mathematical analysis of the Hill nonlinearity case, by trying to determine if some of the properties and theorems of the reaction-diffusion equation literature can be extended to our model. Also, we will numerically construct the traveling wave solution explicitly for the degradation model, and extend these results to more general models.

APPENDIX

STABILITY OF TIME DEPENDENT PROBLEMS

We are going to show that the relaxation algorithm used in Chapter 3 for the cell signaling problem of Section 3.4 and the nonlinear problem of Section 3.3 is conditionally stable, and that the condition depends on h_{\perp} , and the choice of h_0 , i.e. the mesh stepsize in the transversal Laplacian, and the initial step in the compensated grid respectively.

Let us consider scheme (3.47) together with the forward difference scheme for the discretization of the first order time derivative (we use this time discretization for the relaxation approach to solve the model nonlinear problem in Section 3.3.2):

$$\frac{u_{j,k}^{l+1} - u_{j,k}^l}{\Delta t} = \frac{2}{3h_{\perp}^2} \sum_{j' \in \mathcal{N}_j} (u_{j'}^k - u_j^k) + \frac{1}{h_k} \left(\frac{u_j^{k+1} - u_j^k}{h_{k+1/2}} - \frac{u_j^k - u_j^{k-1}}{h_{k-1/2}} \right), \quad (5.2)$$

where l is the time index, Δt is the uniform time step, and everything else is the same as in Eq.(3.47).

We can re-write this scheme in matrix form:

$$\mathbf{u}^{l+1} = Q\mathbf{u}^l, \quad (5.3)$$

where Q is obtained from Eq.(5.2), after multiplying both sides by h_k to make the compensated optimal grid matrix operator, and Q itself, symmetric. Thus

$$Q\mathbf{u} = \mathbf{u} + \Delta t(H + V)\mathbf{u}, \quad (5.4)$$

where H and V are the matrix operator for the horizontal and vertical Laplacian respectively.

Under this notation, a necessary and sufficient condition for scheme (5.2) to be stable is that the spectral radius of Q be less than 1 [80].

Let us indicate with λ the eigenvalues of Q , with λ_{\perp} the eigenvalues of H , and with $\tilde{\lambda}$ the eigenvalues of V . Then, we can write the following expression relating these eigenvalues:

$$\tilde{\lambda} = \lambda_{\perp} - \frac{1 - \lambda}{\Delta t}. \quad (5.5)$$

Using the negativeness of the eigenvalues of V (it is a real tridiagonal matrix with negative values on the main diagonal) in Eq.(5.5), we find that $\lambda < 1$ for any choice of Δt .

We now need to find a condition such that $\lambda > -1$. Let us choose $\lambda = 1$, then:

$$\tilde{\lambda} = \lambda_{\perp} - \frac{2}{\Delta t} \Rightarrow \Delta t = \frac{2}{\lambda_{\perp} + |\tilde{\lambda}|}, \quad (5.6)$$

and the condition for stability is:

$$\Delta t < \frac{2}{\lambda_{\perp} + |\tilde{\lambda}|}, \quad (5.7)$$

which is definitely satisfied if

$$\Delta t < \frac{2}{\max(\lambda_{\perp}) + \max(|\tilde{\lambda}|)}, \quad (5.8)$$

and all is left to do is to estimate these maximal spectral values.

This is a simple task for the compensated optimal grids matrix operator since this values is explicitly given by the optimal rational interpolant. For instance, from Eq. (3.30) we infer that the maximum eigenvalue is $\max(\lambda_{\perp}) = 2.69169/h_{\perp}^2$.

For the transversal Laplacian, we can use the CFL condition and obtain

$$\max(\lambda_{\perp}) = \frac{4}{h_{\perp}^2}, \quad \max(\lambda_{\perp}) = \frac{16}{3h_{\perp}^2}, \quad (5.9)$$

for the centered difference and the 7-point stencil respectively.

In conclusion, a necessary and sufficient condition for stability of scheme (5.2) is:

$$\Delta t < Ch_{\perp}^2, \quad (5.10)$$

where C depends on the choice of optimal grid and discretization on the transversal domain, and can be easily calculated as we discussed above.

REFERENCES

- [1] M. D. Adams and al., “The genome sequence of drosophila melanogaster,” *Science*, vol. 287, pp. 2185–2195, 2000.
- [2] A. Anderson, A. Weaver, P. Cummings, and V. Quaranta, “Tumor morphology and phenotypic evolution driven by selective pressure from the microenvironment,” *Cell*, pp. 905–915, 2006.
- [3] T. Apostol, *Mathematical Analysis*, 2nd ed. Reading, Massachusetts: Addison Wesley Longman, 1974.
- [4] D. Aronson and H. Weinberger, “Multidimensional nonlinear diffusion arising in population genetics,” *Adv. in Math.*, vol. 30, pp. 33–76, 1978.
- [5] A. R. Asthagiri and D. A. Lauffenburger, “Bioengineering models of cell signaling,” *Annu. Rev. Biomed. Eng. 2000*, vol. 2, pp. 31–52, 2000.
- [6] S. Asvadurov and L. Knizhnerman, “Application of the difference (gaussian) rules to solution of hyperbolic problems,” *J. Comp. Phys.*, vol. 158, pp. 116–135, 2000.
- [7] K. Atkinson, *An introduction to Numerical Analysis*, 2nd ed. New York: Wiley, 1989.
- [8] F. Aurenhammer, “Voronoi diagrams- a survey of a fundamental geometric data structure,” *ACM Comp. Surv.*, vol. 23, pp. 345–404, 1991.
- [9] Z. Bai, “Krylov subspace techniques for reduced-order modeling of large-scale dynamical systems,” *Appl. Num. Math.*, vol. 43, pp. 9–44, 2002.
- [10] L. Batsilas, A. Berezhkovskii, and S. Shvartsman, “Stochastic model of autocrine and paracrine signals in cell culture assays,” *Biophys. J.*, vol. 85, pp. 3659–3665, 2003.
- [11] C. V. Buskirk and T. Schupbach, “Versatility in signaling: multiple responses to EGF receptor activation during drosophila oogenesis,” *Trends Cell Biol.*, vol. 9, pp. 1–4, 1999.
- [12] X. Cabre and J. Sola-Morales, “Layer solutions on a half-space for boundary reactions,” *Comm. Pure and Appl. Math.*, vol. I.VIII, pp. 1678–1732, 2005.
- [13] E. W. Cheney, *Introduction to Approximation Theory*, 2nd ed. Providence, RI: AMS, 1999.
- [14] M. Coppey, A. Berezhkovskii, Y. Kim, A. Boettiger, and S. Shvartsman, “Modeling the bicoid gradient: diffusion and nuclear trapping of a stable protein,” *Dev. Biol.*, vol. 312, pp. 623–630, 2007.

- [15] S. T. De-Leon and E. Davidson, "Gene regulation: Gene control network in development," *Annu. Rev. Biophys. Biomol. Struct.*, vol. 36, pp. 191–212, 2007.
- [16] E. M. DeRobertis and H. Kuroda, "Dorsal-ventral patterning and neural induction in xenopus embryos," *Annu. Rev. Cell Dev. Biol.*, vol. 20, pp. 285–308, 2004.
- [17] A. DeWitt and al., "Quantitative analysis of the egfr receptor autocrine system reveals cryptic regulation of cell response by ligand capture," *J. Cell Sci.*, pp. 2301–2313, 2001.
- [18] V. Druskin, "Spectrally optimal finite difference grids in unbounded domains," *Schlumberger-Doll Research Notes EMG*, vol. 002, 1997.
- [19] V. Druskin and L. Knizhnerman, "Gaussian spectral rules for the three-point second differences: I. A two-point positive definite problem in a semiinfinite domain," *SIAM J. Numer. Anal.*, vol. 37, pp. 403–422, 1999.
- [20] A. Eldar, D. Rosin, B. Shilo, and N. Barkai, "Self-enhanced ligand degradation underlies robustness of morphogen gradients," *Dev. Cell.*, vol. 5, pp. 635–646, 2003.
- [21] G. B. Ermentrout and J. B. McLeod, "Existence and uniqueness of traveling waves for a neural network," *Proc. of Roy. Soc. Edinburgh*, vol. 123A, pp. 461–478, 1993.
- [22] C. P. Fall, E. S. Marland, J. M. Wagner, and J. J. Tyson, *Computational Cell Biology*. Berlin: Springer, 2002.
- [23] J. Ferrell, "How responses get more switch-like as you move down a protein kinase cascade," *Trends Biochem. Sci.*, vol. 22, pp. 288–289, 1997.
- [24] P. C. Fife, *Dynamics of Internal Layers and Diffusive Interfaces*. Philadelphia: SIAM, 1988.
- [25] P. C. Fife and J. B. McLeod, "The approach of solutions of nonlinear diffusion equations to travelling wave solutions," *Bull. Am. Math. Soc.*, vol. 81, pp. 1076–1078, 1975.
- [26] P. C. Fife and J. B. McLeod, "The approach of solutions of nonlinear diffusion equations to travelling front solutions," *Arch. Rational Mech. Anal.*, vol. 65, pp. 335–361, 1977.
- [27] P. C. Fife and J. B. McLeod, "A phase plane discussion of convergence to travelling fronts for nonlinear diffusion," *Arch. Rational Mech. Anal.*, vol. 75, pp. 281–314, 1981.
- [28] M. Freeman and J. B. Gurdon, "Regulatory principles of developmental signaling," *Annu. Rev. Cell Dev. Biol.*, vol. 18, pp. 515–539, 2002.
- [29] M. Freeman, "Feedback control of intercellular signalling in development," *Nature*, vol. 408, pp. 313–319, 2000.

- [30] A. Gierer and H. Meinhardt, "A theory of biological pattern formation," *Kibernetik*, vol. 12, pp. 30–39, 1972.
- [31] A. Gierer and H. Meinhardt, "Pattern formation by local self-activation and lateral inhibition," *BioEssays*, vol. 22, pp. 753–760, 2000.
- [32] L. A. Goentoro, C. P. Kowal, G. T. Reeves, C. B. Muratov, L. Marinelli, T. Schupbach, and S. Y. Shvartsman, "Quantifying the gurken morphogen gradient in drosophila oogenesis," *Dev. Cell*, vol. 11, pp. 263–272, 2006.
- [33] G. H. Golub and C. F. V. Loan, *Matrix Computations*, 3rd ed. Baltimore: Johns Hopkins University Press, 1996.
- [34] T. Gregor, W. Bialek, R. de Ruyter van Steveninck, D. Tank, and E. Wieschaus, "Diffusion and scaling during early embryonic pattern formation," *Proc. Natl. Acad. Sci. USA*, pp. 18 403–18 407, 2005.
- [35] B. Hogan, "Morphogenesis," *Cell*, vol. 96, pp. 225–233, 1999.
- [36] B. Houchmandzede, E. Wieschaus, and S. Leibler, "Establishment of developmental precision and proportions in the early drosophila embryo," *Nature*, vol. 415, pp. 798–802, 2002.
- [37] C. F. Huang and J. E. Ferrell, "Ultrasensitivity in the mitogen-activated protein kinase cascade," *Proc. Natl. Acad. Sci. USA*, vol. 93, pp. 10 078–10 083, 1996.
- [38] D. Ingerman, V. Druskin, and L. Knizhnerman, "Optimal finite difference grids and rational approximations of the square root: I. elliptic problems," *Commun. Pure. Appl. Math*, vol. 53, pp. 1039–1066, 2000.
- [39] C. Jones, "Asymptotic behavior of a reaction-diffusion equation in higher space dimensions," *Rocky Mountain J. Math.*, vol. 13, pp. 355–364, 1983.
- [40] D. S. Jones and B. D. Sleeman, *Differential Equations and Mathematical Biology*. London: Chapman and Hall/CRC, 2003.
- [41] J. Keener and J. Sneyd, *Mathematical Physiology*. Berlin: Springer, 1998.
- [42] J. Keener, "Propagation and its failure in coupled systems of discrete excitable cells," *SIAM J. Appl. Math.*, vol. 47, p. 556, 1987.
- [43] S. Kirkpatrick, C. Gelatt, and M. Vecchi, "Optimization by simulated annealing," *Science*, vol. 220, pp. 671–680, 1983.
- [44] D. Klein, V. Nappi, G. Reeves, S. Shvartsman, and M. Lemmon, "Argos inhibits epidermal growth factor receptor signalling by ligand sequestration," *Nature*, vol. 430, pp. 1040–1044, 2004.
- [45] Lodish, Berk, Matsudaira, Kaiser, Krieger, Scott, Zipursky, and Darnell, *Molecular Cell Biology*, 5th ed. New York: W.H. Freeman and Company, 2004.

- [46] P. Maini, R. Baker, and C. Chuong, “The turing model comes of molecular age,” *Science*, vol. 314, pp. 1397–1398, 2006.
- [47] N. Metropolis, A. Rosenbluth, A. Teller, and E. Teller, “Equations of state calculations by fast computing machines,” *J. Chem. Phys.*, vol. 21, pp. 1087–1092, 1953.
- [48] A. S. Mikhailov, *Foundations of Synergetics*. Berlin: Springer, 1994.
- [49] C. B. Muratov and V. Osipov, “Scenarios of domain pattern formation in a reaction-diffusion system,” *Phys. Rev. E*, vol. 54, pp. 4860–4879, 1996.
- [50] C. Muratov and V. V. Osipov, “Optimal grid-based methods for thin film micromagnetics simulations,” *J. Comput. Phys.*, vol. 216, pp. 637–653, 2006.
- [51] C. B. Muratov and M. Novaga, “Front propagation in infinite cylinders. i. a variational approach (submitted),” *Commun. Math. Sci.*, 2008.
- [52] C. B. Muratov and S. Y. Shvartsman, “An asymptotic study of the inductive pattern formation mechanism in drosophila egg development,” *Physica D*, vol. 186, pp. 93–108, 2003.
- [53] C. B. Muratov and S. Y. Shvartsman, “Signal propagation and failure in discrete autocrine relays,” *Phys. Rev. Lett.*, vol. 93, pp. 118 101–4, 2004.
- [54] J. D. Murray, *Mathematical Biology I: An Introduction*. Berlin: Springer, 2002.
- [55] J. D. Murray, *Mathematical Biology II: Spatial Models and Biomedical Applications*. Berlin: Springer, 2003.
- [56] J. Murray, “How the leopard gets its spots,” *Sci. Amer.*, vol. 258, pp. 80–87, 1988.
- [57] D. L. Nikolic, A. N. Boettiger, J. D. Carbeck, and S. Y. Shvartsman, “The role of boundary conditions in an experimental model of epithelial wound healing,” *AJP-Cell Physiology*, vol. 291(1), pp. C68–C75, 2006.
- [58] R. Peierls, “The size of a dislocation,” *Proc. Phys. Soc.*, vol. 52, pp. 34–37, 1940.
- [59] P. Petrushev and V. Popov, *Rational approximation of real functions. Encyclopedia of Mathematics and its Applications*. Cambridge-New York: Cambridge University, 1987.
- [60] F. Posta, S. Y. Shavartsman, and C. B. Muratov, “Compensated optimal grids for elliptic boundary value problems (submitted),” *J. Comp. Phys.*, 2008.
- [61] M. Pribyl, C. B. Muratov, and S. Y. Shvartsman, “Discrete models of autocrine cell communication in epithelial layers,” *Biophys. J.*, vol. 84, pp. 3624–3635, 2003.
- [62] M. Pribyl, C. B. Muratov, and S. Y. Shvartsman, “Long-range signal transmission in autocrine relays,” *Biophys. J.*, vol. 84, pp. 883–896, 2003.

- [63] G. T. Reeves, R. Kalifa, D. Klein, , M. Lemmon, and S. Y. Shvartsman, “Computational analysis of egfr inhibition by argos,” *Dev. Biol.*, vol. 284, pp. 523–535, 2005.
- [64] G. T. Reeves, C. B. Muratov, T. Schupbach, and S. Y. Shvartsman, “Quantitative models of developmental pattern formation,” *Developmental Cell*, vol. 11, pp. 289–300, 2006.
- [65] V. Riechmann and A. Ephrussi, “Axes formation during drosophila oogenesis,” *Curr. Opin. Genet. Dev.*, vol. 11, pp. 374–383, 2001.
- [66] J. Rinzel and J. B. Keller, “Traveling wave solution of a nerve conduction equation,” *Biophys. J.*, vol. 13, pp. 1313–1337, 1973.
- [67] J. Roquejoffre, “Convergence to travelling waves for solutions of a class of semilinear parabolic equations,” *J. Diff. Eq.*, vol. 108, pp. 262–295, 1994.
- [68] J. Roquejoffre, “Eventual monotonicity and convergence to travelling fronts for the solutions of parabolic of parabolic equations in cylinders,” *Ann. Inst. H. Poincare Anal. Non Lin.*, vol. 14, pp. 499–552, 1997.
- [69] J. B. Rosser, “Nine point difference solutions for poisson’s equation,” *Comp. Math. Appl.*, vol. 1, pp. 351–360, 1975.
- [70] S. K. Scott and K. Showalter, “Simple and complex propagating reaction-diffusion fronts,” *J. of Phys. Chem.*, vol. 90, 1992.
- [71] L. A. Segel, *Modeling dynamic phenomena in molecular and cellular biology*. Cambridge: Cambridge University Press, 1984.
- [72] S. Y. Shvartsman, C. B. Muratov, and D. A. Lauffenburger, “Modeling and computational analysis of egf receptor-mediated cell communication in drosophila oogenesis,” *Development*, vol. 129, pp. 2577–2589, 2002.
- [73] S. Y. Shvartsman, “Quantitative analysis of developing tissues,” *AIChE Journal*, vol. 51, pp. 1312–1318, 2005.
- [74] A. C. Spradling, *Developmental Genetics of oogenesis, in The Development of Drosophila Melanogaster*. Cold Spring Harbor, New York: Cold Spring Harbor Laboratory Press, 1993.
- [75] J. C. Strikwerda, *Finite Difference Schemes and Partial Differential Equations*, 2nd ed. Pacific Grove, CA: SIAM, 2004.
- [76] K. Swanson, C. Bridge, J. Murray, and E. Alvord, “Virtual and real brain tumors: using mathematical modeling to quantify glioma growth and invasion,” *J. Neurolog. Sci.*, vol. 216, pp. 1–10, 2003.

- [77] K. Swanson, L. True, D. Lin, K. Buhler, R. Vessella, and J. Murray, "A quantitative model for the dynamics of serum prostate-specific antigen as a marker for cancerous growth," *Amer. J. Pathol.*, vol. 158, pp. 2195–2199, 2001.
- [78] K. Swanson, L. True, and J. Murray, "On the use of quantitative modeling to help understand psa dynamics an other medical problems," *Amer. J. Clin. Pathol.*, vol. 119, pp. 14–17, 2003.
- [79] M. E. Taylor, *Partial Differential Equations II: Qualitative Studies of Linear Equations*. Berlin: Springer-Verlag, 1996.
- [80] J. W. Thomas, *Numerical Partial Differential Equations: Finite Difference Methods*. New York: Springer, 1995.
- [81] J. F. Toland, "The Peierls-Nabarro and Benjamin-Ono equations," *J. Funct. Anal.*, vol. 145, pp. 136–150, 1997.
- [82] L. N. Trefethen, *Spectral Methods in MATLAB*. Philadelphia: SIAM, 2000.
- [83] A. Turing, "The chemical basis of morphogenesis," *Phil. Trans. B.*, vol. 237, pp. 37–72, 1952.
- [84] D. Umulis, M. Serpe, M. O'Connor, and H. Othmer, "Robust, bistable patterning of the dorsal surface of the drosophila embryo," *Proc. Natl. Acad. Sci. USA*, vol. 103, pp. 11 613–11 618, 2006.
- [85] Q. Wang, V. G., and W. Z., "Control of epidermal growth factor receptor endocytosis by receptor dimerization, rather than receptor kinase activation," *EMBO Rep.*, pp. 942–948, 2005.
- [86] P. B. Weisz, "Diffusion and chemical transformation," *Science*, vol. 179, pp. 433–440, 1973.
- [87] O. Wilby and G. Webster, "Experimental studies on axial polarity. in hydra," *J. Embryol. Exp. Morphol.*, vol. 24, pp. 595–613, 1970.
- [88] S. H. Wiley, S. Y. Shvartsman, and D. A. Lauffenburger, "Computational modeling of the EGF-receptor system: a paradigm for systems biology," *Trends Cell Bio.*, vol. 13, pp. 43–50, 2003.
- [89] L. Wolpert, "Positional information and pattern formation," *Curr. Top. Dev. Biol.*, vol. 6, pp. 183–224, 1971.
- [90] L. Wolpert and al., *Principles of Development*. Oxford: Oxford University Press, 1998.
- [91] L. Wolpert, J. Hicklin, and A. Hornbruch, "Positional information and pattern regulation in regeneration of hydra," *Symp. Soc. Exp. Biol.*, vol. 25, pp. 391–415, 1971.

- [92] J. Yin, K. Xu, A. Kumar, and F. Yu, "Wound-induced atp release egf receptor activation in epithelial cells," *J. Cell Sci.*, vol. 120, pp. 815–825, 2007.
- [93] Y. Zhang, A. Lander, and Q. Nie, "Computational analysis of bmp gradients in dorsal-ventral patterning of the zebrafish embryo," *J. Theo. Biol.*, vol. 248, pp. 579–589, 2007.